



Linking the active zone ultrastructure to function in *Drosophila*

Struktur-Funktions-Beziehungen an der aktiven Zone in *Drosophila*

Doctoral thesis for a doctoral degree
at the Graduate School of Life Sciences,
Julius-Maximilians-Universität Würzburg,
Section Neuroscience

submitted by

Nadine Ehmann

from

Eberstadt

Würzburg 2015

Members of the Thesis Committee:

Dr. Robert Kittel

Prof. Erich Buchner

Prof. Wolfgang Rössler

Chairman: Prof. Thomas Hünig

Submitted on:

Date of Public Defense:

Date of Receipt of Certificates:

Substantial parts of this thesis are published in the following articles:

Ehmann, N.,* van de Linde, S.*, Alon, A., Ljaschenko, D., Keung, X.Z., Holm, T., Rings A., DiAntonio, A., Hallermann, S., Ashery, U., Heckmann, M., Sauer, M. & Kittel R.J. (2014). Quantitative super-resolution imaging of Bruchpilot distinguishes active zone states. *Nature Communications*, 5, 1–12. (*equal contribution)

Ehmann N., Sauer M. Kittel R.J. Super-resolution microscopy of the synaptic active zone. *Front. Cell. Neurosci.* 9:7.

Affidavit

I hereby confirm that my thesis entitled *Linking the active zone ultrastructure to function in Drosophila* is the result of my own work. I did not receive any help or support from commercial consultants. All sources and / or materials applied are listed and specified in the thesis.

Furthermore, I confirm that this thesis has not been submitted as part of another examination process neither in identical or similar form.

Würzburg,

Signature

Eidesstattliche Erklärung

Hiermit erkläre ich an Eides statt, die Dissertation *Linking the active zone ultrastructure to function in Drosophila* eigenständig, d.h. insbesondere selbstständig und ohne Hilfe eines kommerziellen Promotionsberaters, angefertigt und keine anderen als die von mir angegebenen Quellen und Hilfsmittel verwendet zu haben.

Ich erkläre außerdem, dass die Dissertation weder in gleicher noch in ähnlicher Form bereits in einem anderen Prüfungsverfahren vorgelegen hat.

Würzburg,

Signature

1. SUMMARY	1
1. ZUSAMMENFASSUNG	2
2. INTRODUCTION	4
2.1 Chemical synapses	4
2.1.1 The presynaptic active zone	5
2.1.1.1 Structural organization of active zones	5
2.1.1.2 Molecular composition of active zones	8
2.1.1.3 Functional determinants of neurotransmitter release	12
2.2 <i>Drosophila melanogaster</i>	13
2.2.1 Background	13
2.2.2 Anatomy and physiology of the neuromuscular junction	15
2.2.3 Active zones at neuromuscular junctions in <i>Drosophila</i>	18
2.2.3.1 Molecular composition and ultrastructure of the <i>Drosophila</i> AZ	18
2.2.3.2 Brp and Rab3 - Implications in synaptic plasticity	23
2.3 Microscopy	26
2.3.1 Optical light microscopy	26
2.3.2. Electron microscopy	27
2.3.3. Super-resolution microscopy	28
2.3.3.1 Application in the neurosciences	30
2.4 Motivation of the study	31
3. MATERIALS & METHODS	32
3.1 Fly stocks	32
3.2 Electrophysiology	32
3.2.1 Two-electrode voltage clamp	32
3.2.2 Modelling	34
3.3 Confocal imaging	36
3.3.1 Immunohistochemistry and image acquisition	36
3.3.2 Data analysis	37
3.3 Super-resolution imaging	37
3.3.1 Antibody labelling and image acquisition	37
3.3.2 Data analysis	39
3.3.2.1 Cluster analysis	41
3.3.3 Quantification of Brp protein numbers	42
3.4 Statistical analysis	44

4. RESULTS	45
4.1 Localization microscopy of the CAZ nanostructure	45
4.1.1 Application of <i>d</i> STORM to <i>Drosophila</i> AZs	45
4.1.2 Density-based analysis of CAZ-units	47
4.2 Quantifying the substructural organization of Brp in the CAZ	49
4.3 Ultrastructural analysis of different AZ states	52
4.4 Functional properties of AZ states	56
4.4.1 Electrophysiological characterization of different AZ states	56
4.4.2 Mechanistic interpretation of AZ function	59
4.5 Dissecting structure-function relationships	61
5. DISCUSSION	64
5.1 Localization microscopy of the CAZ nanostructure	64
5.2 Quantifying the substructural organization of Brp in the CAZ	67
5.3 Analysis of different AZ states	70
5.4 Dissecting structure-function relationships	72
6. CONCLUSION & OUTLOOK	74
7. REFERENCES	80
8. ABBREVIATIONS	95
9. TABLE OF FIGURES	99
10. APPENDIX	100
10.1 List of publications	100
10.2 Curriculum vitae	101

Danke

Mein größter Dank gilt meinem Betreuer und Doktorvater Robert Kittel, von dem ich sehr viel über wissenschaftliches Arbeiten, Denken und Schreiben lernen durfte, der konstruktiv Kritik geübt hat, wenn es angebracht war, und mich in “schwierigen“ wissenschaftlichen Zeiten immer unterstützt hat. Ich bin extrem dankbar, dass ich in seinem Labor arbeiten durfte und weiterhin darf. Außerdem möchte ich mich bei Manfred Heckmann für seine Unterstützung in der Publikationsphase, seine Expertise in wissenschaftspolitischen Fragen, das Lesen der Doktorarbeit und den Unterschlupf in seinem Institut bedanken. Des Weiteren bedanke ich mich bei den Mitgliedern meines Promotionskomitees Wolfgang Rössler und Erich Buchner, der sich außerdem bereit erklärt hat das Zweitgutachten zu übernehmen, sowie bei Thomas Hünig für den Prüfungsvorsitz.

Eine wissenschaftliche Arbeit ist nie der Verdienst eines Einzelnen, deshalb möchte ich mich bei allen bedanken, die zum Gelingen beigetragen haben. Zuallererst bei Markus Sauer, Sebastian van de Linde und Thorge Holm, die sowohl ihr Setup, als auch ihr Wissen über *d*STORM zu jeder Zeit bereitwillig geteilt haben, sowie immer wieder neue Ideen einbrachten um die Proteinquantifizierung zu ermöglichen. Bei Annika Rings und Stefan Hallermann für die Analyse der radialen Brp Verteilungen und das Modelling sowie bei Amit Alon und Uri Ashery für die Clusteranalyse. Außerdem bei Aaron diAntonio, Xi Zhen Keung für elektrophysiologische Messungen und bei Dmitrij Ljaschenko, der vor allem in der Anfangsphase maßgeblich an diesem Projekt beteiligt war und von dem ich Vieles über Elektrophysiologie und *Drosophila* gelernt habe. Des Weiteren bedanke ich mich sowohl bei Stefan Sigrist als auch bei Erich Buchner für die Bereitstellung von Antikörpern.

Mein Dank geht an alle Mitarbeiter der Neurophysiologie, insbesondere an Tobias Langenhan, für wissenschaftliche Gespräche, gute Ratschläge und seine Hilfsbereitschaft, an Claudia Wirth, die mir alles über Fliegen- und Laborarbeit beigebracht hat und Maria Oppmann, für ihre exzellente Unterstützung während meiner molekularbiologischen Ausflüge. An Dmitrij Ljaschenko, Martin Pauli, Marjan Fateh,

Isabella Maiellaro und Nicole Scholz - ihr seid nicht nur zu den besten Kollegen, sondern auch zu Freunden geworden.

Bedanken möchte ich mich außerdem bei der Graduate School of Life Sciences, die es jungen Wissenschaftlern durch ihre Förderung ermöglicht auf eigenen Beinen zu stehen.

Zu guter Letzt, bedanke ich mich bei meinen Eltern. Mama, Papa, ihr habt es mir ermöglicht zu studieren und mich unterstützt wo immer ihr konntet. Danke! Außerdem bei meiner Schwester Sandra, Anne-Catherine und Juliane – es ist schön gute Freunde zu haben.

1. Summary

Accurate information transfer between neurons governs proper brain function. At chemical synapses, communication is mediated via neurotransmitter release from specialized presynaptic intercellular contact sites, so called active zones. Their molecular composition constitutes a precisely arranged framework that sets the stage for synaptic communication.

Active zones contain a variety of proteins that deliver the speed, accuracy and plasticity inherent to neurotransmission. Though, how the molecular arrangement of these proteins influences active zone output is still ambiguous. Elucidating the nanoscopic organization of AZs has been hindered by the diffraction-limited resolution of conventional light microscopy, which is insufficient to resolve the active zone architecture on the nanometer scale. Recently, super-resolution techniques entered the field of neuroscience, which yield the capacity to bridge the gap in resolution between light and electron microscopy without losing molecular specificity. Here, localization microscopy methods are of special interest, as they can potentially deliver quantitative information about molecular distributions, even giving absolute numbers of proteins present within cellular nanodomains.

This thesis puts forward an approach based on conventional immunohistochemistry to quantify endogenous protein organizations *in situ* by employing *direct* stochastic optical reconstruction microscopy (*d*STORM). Focussing on Bruchpilot (Brp) as a major component of *Drosophila* active zones, the results show that the cytomatrix at the active zone is composed of units, which comprise on average ~137 Brp molecules, most of which are arranged in approximately 15 heptameric clusters. To test for a quantitative relationship between active zone ultrastructure and synaptic output, *Drosophila* mutants and electrophysiology were employed. The findings indicate that the precise spatial arrangement of Brp reflects properties of short-term plasticity and distinguishes distinct mechanistic causes of synaptic depression. Moreover, functional diversification could be connected to a heretofore unrecognized ultrastructural gradient along a *Drosophila* motor neuron.

1. Zusammenfassung

Kommunikation zwischen Nervenzellen ist von grundlegender Bedeutung für die Hirnfunktion. An chemischen Synapsen findet diese an hoch spezialisierten interzellulären Kontaktstellen statt, den aktiven Zonen, welche die Voraussetzung für präzise Neurotransmission schaffen und somit die synaptische Kommunikation gewährleisten.

In aktiven Zonen befindet sich eine Vielzahl von Proteinen dicht gepackt, die Geschwindigkeit, Genauigkeit und Plastizität der Signaltransduktion vermitteln. Bisher ist es jedoch unklar, in welcher Weise die molekularen Organisationsprinzipien dieser Proteine die Funktion der aktiven Zone beeinflussen. Teilweise ist dies dem Auflösungsvermögen konventioneller Lichtmikroskopie geschuldet, das nicht ausreicht um die Architektur der aktiven Zone im Nanometer Bereich aufzuklären. Unlängst jedoch haben neue Methoden der hochaufgelösten Fluoreszenzmikroskopie ihren Weg in die Neurowissenschaften gefunden. Diese sind in der Lage die Lücke zwischen optischer Lichtmikroskopie und Elektronenmikroskopie zu schließen, ohne die Identität der Proteinspezies aus den Augen zu verlieren. Besonderes Interesse kommt hierbei sogenannten Lokalisationsmikroskopie Techniken zu. Diese können neben der Darstellung molekularer Organisationen im Idealfall sogar quantitative Informationen über die absolute Anzahl bestimmter Moleküle in subzellulären Bereichen liefern.

In der vorliegenden Arbeit wurde eine Methode entwickelt, die auf klassischer Immunohistochemie beruht und *d*STORM (*direct* stochastic optical reconstruction microscopy) nutzt, um die endogene Proteinorganisation *in situ* zu quantifizieren. Fokussierend auf Brp (Bruchpilot), einem Protein an der aktiven Zone von *Drosophila melanogaster*, zeigen die Ergebnisse, dass die Zytomatrix an der aktiven Zone modular aufgebaut ist, wobei jedes Modul ~137 Brp Moleküle umfasst. Diese sind zum Großteil in etwa 15 Gruppen mit je 7 Untereinheiten angeordnet. Um auf einen quantitativen Zusammenhang zwischen der Ultrastruktur der aktiven Zone und ihrer Funktion zu schließen, wurden *Drosophila* Mutanten eingesetzt und mittels Elektrophysiologie funktionell untersucht. Die Ergebnisse veranschaulichen, dass sich spezifische Eigenschaften von Kurzzeitplastizität in der präzisen Anordnung von Brp

widerspiegeln, was Rückschlüsse auf verschiedene Ursprünge synaptischer Depression zulässt. Darüber hinaus beschrieben *d*STORM Experimente erstmals, dass ein funktioneller Gradient entlang des Motoneurons mit der graduellen Veränderung der Anzahl von Bruchpilotmolekülen pro aktive Zone korreliert.

2. Introduction

2.1 Chemical synapses

Synapses are specialized intercellular contact sites that mediate fast and precise communication between neurons to ensure proper brain function. When ‘synapses’ were first mentioned by Charles Sherrington in 1897 and characterized histologically by Ramón y Cajal (Ramón y Cajal, 1894) the nature of neuronal communication was discussed controversially. Initially, it was assumed that all synapses communicate via electrical signalling. This ‘fast’ mode of neurotransmission is mediated by the flow of electrical current directly from the pre- to the postsynaptic cell.

In the 1920s, however, Otto Loewi discovered the ‘Vagusstoff’, thus providing the first description of a chemical compound that acts as a neurotransmitter and the first verification of chemical neurotransmission (Loewi, 1921). Chemical synapses rely on presynaptic release and postsynaptic detection of neurotransmitter molecules. Besides signal amplification, this allows synapses to act as small computational units (Südhof, 2012) that are able to modify signals in an activity-dependent manner, thereby influencing synaptic strength. The basic idea that learning results from changes in synaptic strength was already proposed by Ramón y Cajal and incorporated further into more refined models by Donald Hebb (Hebb, 1949). The modulation of synaptic elements based on activity is known as ‘synaptic plasticity’ and was recognized early as an essential component of learning and memory, which motivated detailed studies in both the invertebrate system (Kandel, 1976, 2001) and the mammalian hippocampus (Bliss and Lømo, 1973; Bliss and Collingridge, 1993). Subsequently, synaptic plasticity has been assigned to presynaptic changes in the effectiveness of neurotransmitter release or to postsynaptic changes in biophysical receptor properties (Choquet and Triller, 2013).

Communication at chemical synapses is driven by the depolarization-induced opening of calcium (Ca^{2+}) channels, which triggers transmitter-laden synaptic vesicles (SVs) to fuse with the presynaptic membrane and to release their cargo into the synaptic cleft.

Following this, specific postsynaptic receptor ion channels activate and enable current flow to convey the neuronal signal.

This work focuses on presynaptic elements of neurotransmission, in particular on the active zone (AZ), the site of neurotransmitter release, which is an integral part of the complex molecular framework that modulates synaptic transmission.

2.1.1 The presynaptic active zone

2.1.1.1 Structural organization of active zones

The fusion of SVs with the presynaptic plasma membrane to subsequently release their neurotransmitter is controlled in a spatially and temporally highly precise manner.

Spatially, SVs dock and fuse at a specialized area, called the ‘active zone’ (Couteaux and Pécot-Dechavassine, 1970). AZs with their associated cytomatrix (CAZ), a complex meshwork of distinct proteins, build the stage for synaptic neurotransmission and exhibit characteristic structural features that are conserved in a variety of organisms [Figure 1; (Zhai and Bellen, 2004)]. First, when viewed by electron microscopy (EM), the CAZ appears electron dense, indicating its proteinaceous composition. Second, SVs tether, dock and fuse at AZs (Heuser and Reese, 1973) and third, AZs are precisely aligned with the postsynaptic density that houses receptors to receive neurotransmitter signals. EM studies in mammalian central nervous systems showed that the CAZ is a web-like pattern, consisting of ‘pyramidally-shaped particles’, that reach approximately 50 nm into the cytoplasm (Bloom and Aghajanian, 1968; Pfenninger et al., 1972; Landis et al., 1988; Phillips et al., 2001; Zhai and Bellen, 2004). Likewise, the first 3D-structural description of the CAZ at frog neuromuscular junctions (NMJs) was provided by employing electron tomography (Harlow et al., 2001). Here, the CAZ is composed of an array-like structure with ‘beams’ and ‘ribs’ that connect SVs, whereas ‘pegs’ are supposed to represent putative Ca^{2+} channels that are perfectly aligned to mediate the release of a SV.

Additionally, some AZs possess dense projections that reach from the CAZ into the cytoplasm and are surrounded by SVs. Such dense projections can be rather small as in the mammalian CNS (Phillips et al., 2001), medium sized, such as the *Drosophila* T-bar

(Atwood et al., 1993), or prominent structures like ribbon synapses, which can be found in the vertebrate sensory system (Lenzi and von Gersdorff, 2001). Despite intensive research it is not clear why they come in a variety of shapes and sizes, which differ tremendously among organisms (Figure 1). However, it is supposed that large dense projections can tether more SVs to ensure sufficient and rapid vesicle delivery to the AZ (Zhai and Bellen, 2004).

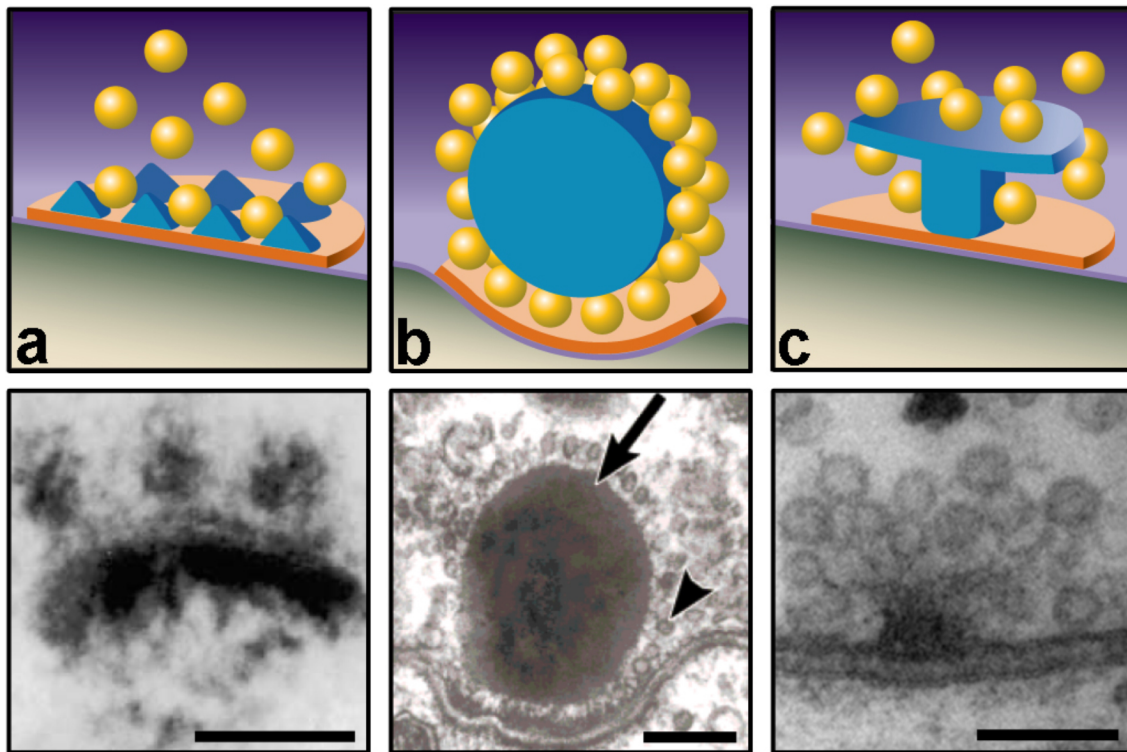


Figure 1 AZ ultrastructures. (a-c) Schematics of AZ structures in various organisms (upper panel) with corresponding electron micrographs (lower panel). Modified from Zhai and Bellen, 2004. (a) Synaptic terminal of the mammalian CNS shows the dense projection as part of the presynaptic particle web. Modified from Phillips et al., 2001. (b) Ribbon synapse of the frog inner ear hair cell. Arrow depicts the presynaptic dense projection, surrounded by SVs (arrowhead). From Lenzi and von Gersdorff, 2001. (c) T-bar at AZs of *Drosophila melanogaster* with tethered SVs. From Hallermann et al., 2010c. Scale bars: (a) 100 nm, (b) 200 nm, (c) 100 nm.

Temporally, the release of SVs is extremely fast, in that the delay between presynaptic Ca^{2+} influx and postsynaptic depolarization can be less than a millisecond (Borst and Sakmann, 1996; Sabatini and Regehr, 1996; Geiger and Jonas, 2000). The detailed mechanisms underlying such a brief delay are not completely understood, but a crucial component that might assure high-speed transmission is the tight packing of participating molecules (Eggermann et al., 2012). In fact, ultrastructural studies

employing electron tomography at the frog NMJ suggested a distance of ~ 20 nm between Ca^{2+} -channels and SVs (Harlow et al., 2001). Similarly, functional analysis of squid giant synapses and ciliary ganglion calyx synapses of the chick indicated nanometer-coupling [‘nanodomain’; < 100 nm (Eggermann et al., 2012); Figure 2a] between Ca^{2+} source and Ca^{2+} sensor (Adler et al., 1991; Stanley, 1997). In the last years, a number of mammalian central synapses were made experimentally accessible and provide evidence for a looser coupling between SVs and Ca^{2+} channels, known as ‘microdomain’ coupling [> 100 nm; Figure 2b; (Borst and Sakmann, 1996; Ohana and Sakmann, 1998; Rozov et al., 2001; Meinrenken et al., 2002; Fedchyshyn and Wang, 2005; Vyleta and Jonas, 2014)].

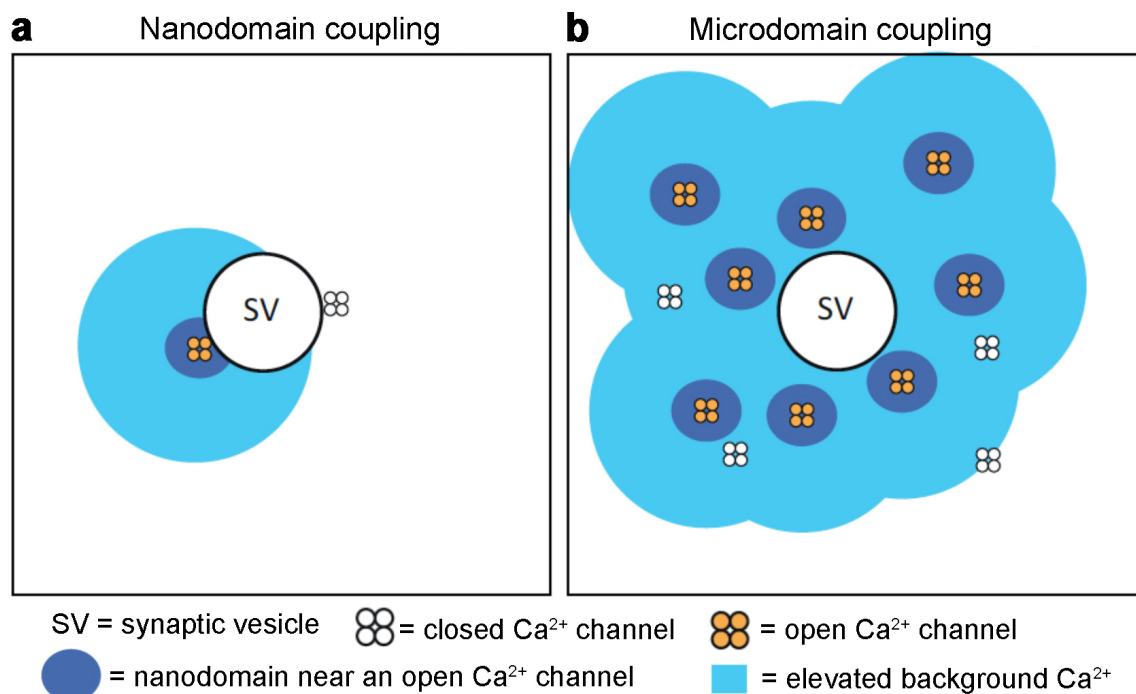


Figure 2 Schematics of nanodomain and microdomain coupling at a single vesicle release site. (a) Nanodomain coupling occurs when the fusion of a SV is triggered by the local flux of Ca^{2+} through one or a very small number of open Ca^{2+} channel(s). **(b)** Microdomain coupling occurs when SV fusion is triggered by Ca^{2+} flux through a number of open Ca^{2+} channels that could lead to an elevation of background Ca^{2+} concentration within the AZ. Not to scale, modified from Tarr et al., 2013.

Valuable quantitative information on both coupling regimes has been obtained by employing electrophysiology, modelling, Ca^{2+} -imaging and Ca^{2+} -uncaging (Bollmann et al., 2000; Schneggenburger and Neher, 2005; Sun et al., 2007; Eggermann et al., 2012). However, there appears to be no general map of SV and Ca^{2+} channel arrangements at the AZ [e.g. (Meinrenken et al., 2002)].

The underlying mechanisms that lead to nanodomain or microdomain coupling are still unclear and interpretations are complicated by results reporting developmental modulations, pathway-specific use and dynamic regulations of coupling modes that contribute to distinct forms of presynaptic plasticity (Eggermann et al., 2012).

Originally based on evidence from analyses at the frog NMJ, an interesting hypothesis for synapse reliability in various model systems was proposed recently. Here, the basic building block is an unreliable single vesicle release site that utilizes nanodomain coupling to trigger vesicle fusion (Figure 2a). Consequently, low release probability synapses can be designed by employing a small number of such building blocks within a few AZs whereas large and reliable synapses are constructed using plenty of unreliable single vesicle release sites within hundreds of AZs (Tarr et al., 2013). Thus, varying AZ size as well as the number and spatial distribution of unreliable single vesicle release sites could influence synaptic properties. Single vesicle release sites themselves have been proposed to be built from pre-assembled AZ proteins that arrive via AZ precursor vesicles (Zhai et al., 2001; Sorra et al., 2006). After insertion into the plasma membrane, association with Ca^{2+} channels is regulated in a biochemical manner, leading to nano- or microdomain coupling. When synapses mature, coupling modes could be modified [e.g. immature and mature Calyx of Held; (Fedchyshyn and Wang, 2005)] via protein-protein interactions between release site proteins and Ca^{2+} channels [e.g. (Han et al., 2011; Kaeser et al., 2011)] or variation in phosphorylation states that influence Ca^{2+} channel properties [see (Tarr et al., 2013)].

2.1.1.2 Molecular composition of active zones

The underlying protein composition of AZs sets the basis for efficient and accurate neurotransmission (Rosenmund, 2003). This includes the organization of SV pools, tethering, docking and priming of SVs, the coupling of endo- and exocytotic machineries and the positioning of Ca^{2+} channels relative to SV docking sites (Gundelfinger and Fejtova, 2012). Hence, a variety of proteins act together, whose molecular identities have recently been reviewed thoroughly [e.g. (Südhof, 2004; Jahn and Fasshauer, 2012; Südhof, 2012)].

The core of the AZ is made up of five conserved proteins, namely RIM (Rab3-interacting molecule), RIM binding protein (RBP/RIM-BP), Munc13 [mammalian homologue of the nematode *C. elegans* Unc13 (uncoordinated) protein], Liprin- α and the CAZ-associated structural protein [(CAST/ERC/ELKS); Figure 3]. Intriguingly, expression of these core proteins is not restricted to AZs but can also be found in non-neuronal (ELKS and Liprin- α), neuroendocrine or other secretory cells [RIM, Munc13 and RIM-BP; (Südhof, 2012)]. Additionally, Bassoon and its structurally related homolog Piccolo/Aczonin are associated with vertebrate AZs (tom Dieck et al., 1998; Fenster et al., 2000; Limbach et al., 2011) and are supposed to serve as scaffolds for the assembly of dense projections or the whole presynaptic particle web (Limbach et al., 2011). Furthermore, proteins related to Syd-1 (synapse defective-1) could be identified to play an important role in assembling invertebrate AZs (Owald et al., 2010). As part of the vesicle fusion machinery, SNARE (soluble N-ethylmaleimide-sensitive factor attachment receptor)-proteins like Syntaxin and SNAP-25 and the SM (Sec1/Munc18-like)-protein Munc18 are distributed in the plasma membrane (Figure 3).

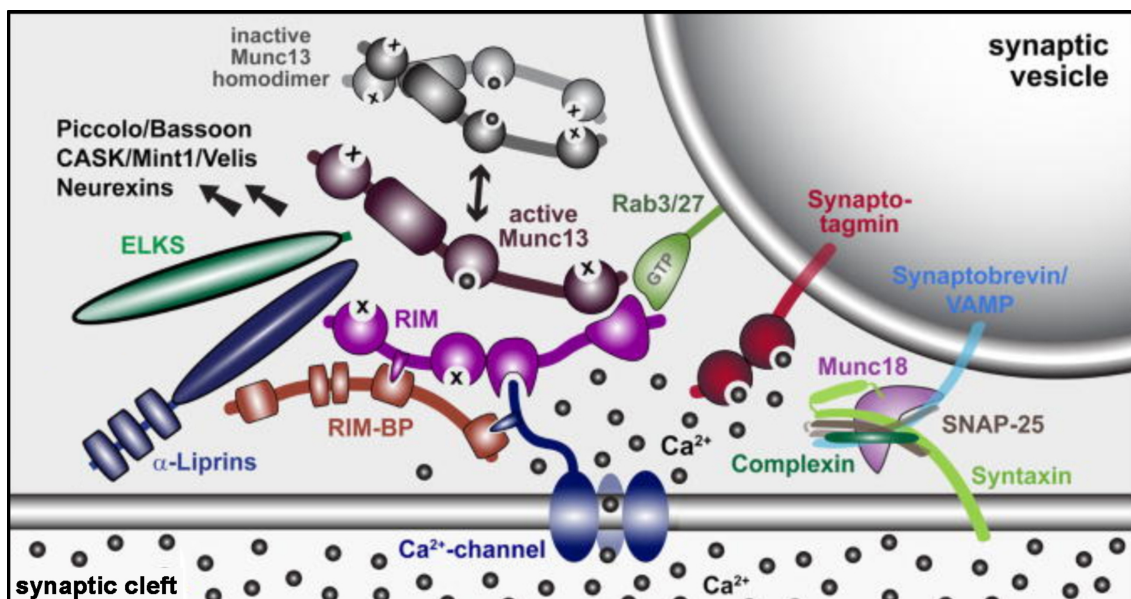


Figure 3 Key players at the presynaptic AZ. Schematic shows part of a SV (top right) and the presynaptic plasma membrane (grey) with essential proteins for SV release. Left and middle part depicts the AZ core protein complex, which consists of RIM, RBP, Munc13, Liprin- α and the CAZ-associated protein CAST/ERC/ELKS in addition to an AZ Ca²⁺ channel. The indicated interaction between RIM and vesicular Rab3/27 is thought to dock SVs, while RIM mediated Munc13 activation leads to SV priming. The core fusion machinery, comprising the SNARE proteins and Munc18 as well as Complexin is shown on the right. Adapted from Südhof, 2012.

Syntaxin and SNAP-25 associate with the vesicular SNARE protein Synaptobrevin to form a helical coiled coil complex that brings the SV membrane and the presynaptic plasma membrane in close proximity. Munc18, which is connected to Syntaxin throughout SNARE complex assembly and disassembly, alters its conformation as a consequence of SNARE association to interact with the SNARE complex (Dulubova et al., 2007). Subsequent vesicle fusion and neurotransmitter release leave the SNARE/SM complex in the plasma membrane. For repeated fusion cycles, this complex has to be disassembled by NSF (N-ethylmaleimide-sensitive factor,) and SNAPs [soluble NSF attachment proteins; (Wojcik and Brose, 2007; Jahn and Fasshauer, 2012; Südhof, 2013)]. Key regulators of such SNARE-mediated vesicle fusions are Munc18, Munc13, Synaptotagmin and Complexin. All of these proteins participate in excitation-secretion coupling: the transduction of an electrical signal into neurotransmitter release following neuronal depolarization (Schneggenburger and Neher, 2005; Wojcik and Brose, 2007). Vesicle docking, priming, Ca^{2+} triggering and vesicle fusion make up the four steps that are necessary for fast and precise excitation-secretion coupling (Wojcik and Brose, 2007). A popular model describes vesicle docking as the attachment of SVs to the presynaptic plasma membrane where they mature to become fusion competent (priming), which establishes an RRP (readily releasable pool) of SVs that can be released rapidly following Ca^{2+} flux into the cell (Südhof, 2013).

Docking and priming of SVs as well as the recruitment of Ca^{2+} channels at mammalian AZs is attained by a large protein complex consisting of RIM, RBP and Munc13 (Kaeser et al., 2011; Südhof, 2013). The interaction of RIM with the small vesicular GTP (guanosine triphosphate)-binding proteins Rab3 and Rab27 docks SVs (Gracheva et al., 2008; Han et al., 2011; Kaeser et al., 2011; Fernández-Busnadiego et al., 2013), while RIM mediated Munc13 activation leads to SV priming via SNARE complex assembly (Brose et al., 1995; Augustin et al., 1999; Betz et al., 2001; Richmond et al., 2001; Deng et al., 2011; Ma et al., 2013). To immediately react on alterations in AZ Ca^{2+} concentrations, SVs and Ca^{2+} channels are tightly associated. This close proximity is established by the interaction of RIM and RBP that co-operate to recruit Ca^{2+} channels to sites of vesicle fusion (Hibino et al., 2002; Han et al., 2011; Kaeser et al., 2011; Liu et al., 2011). To finally induce SV fusion Synaptotagmin and Complexin are necessary, which convey the presynaptic Ca^{2+} signal. Their precise functions however,

remain enigmatic, since both proteins hold clamping as well as activation properties (Geppert et al., 1994; McMahon et al., 1995; Neher, 2010a; Südhof, 2013). Moreover, technical challenges in assessing the distinct steps preceding vesicle fusion have hindered clarification of their underlying molecular processes. Recently, a study employed cryofixation and three-dimensional electron tomography to investigate molecular and morphological characteristics of vesicle docking and priming with high precision under almost native conditions. Interestingly, the authors found conserved tethering and docking mechanisms and that SV docking, priming and SNARE-assembly are morphological, functional and molecular appearances of the same process, which follows SV tethering (Imig et al., 2014).

As mentioned above, ultrafast neurotransmission in response to neuronal depolarization can only be achieved when docked and primed SVs reside near AZ Ca^{2+} channels. In addition to the ‘molecular priming’ hypothesis, a different theory, known as ‘positional priming’, also provides an explanation for tight coupling between SVs and Ca^{2+} channels (Wadel et al., 2007; Neher and Sakaba, 2008). According to this, SVs located further away from AZ Ca^{2+} channels would be released reluctantly since they would not sense nanodomain Ca^{2+} concentrations (Neher and Sakaba, 2008). The hypothesis was tested by employing caged Ca^{2+} stimulation to measure the intrinsic Ca^{2+} sensitivity of SVs that remained after depletion of the RRP. Interestingly, these reluctantly released vesicles are nearly as sensitive towards Ca^{2+} as the rapidly released ones, suggesting a longer distance to the next Ca^{2+} channel (Wadel et al., 2007). However, it should be noted that also heterogeneity in intrinsic Ca^{2+} sensitivity may well play a role in the kinetics of SV release (Wölfel et al., 2007). Recently, it was demonstrated that reluctant SVs can be transformed into fast-releasing ones by changing their position to AZ Ca^{2+} channels, which strengthens the hypothesis of ‘positional priming’ (Lee et al., 2012). Originally thought to predominantly take part in asynchronous release (Sakaba, 2006), this finding assigns a role to reluctant SVs in synchronous release via an actin-dependent mechanism that recruits reluctant SVs into a fast-releasing vesicle pool to prevent short-term synaptic depression (Lee et al., 2012). Furthermore, a follow up study could show that newly recruited vesicles can only respond at full speed to a Ca^{2+} stimulus after so-called ‘superpriming’, which increases the Ca^{2+} sensitivity of primed SVs to ensure full release competence. In contrast to ‘positional priming’, this process

is supposed to be actin-independent and rather regulated by modulation of Munc13 function. Therefore, ‘superpriming’ presents an additional step in refilling the fast-releasing vesicle pool (Lee et al., 2013). Although controversially discussed, it is assumed that ‘molecular’ as well as ‘positional’ priming determine the kinetics of neurotransmission (Wadel et al., 2007; Wölfel et al., 2007; Neher and Sakaba, 2008).

2.1.1.3 Functional determinants of neurotransmitter release

Derived from the hypothesis that neurotransmitters are released in “quantal units” (Del Castillo and Katz, 1954), it is understood that synaptic strength can be described by N , the number of fusion competent SVs (readily-releasable vesicles, RRVs), p_{vr} , their probability of exocytosis and q , usually taken to reflect postsynaptic sensitivity. This conceptual framework plays an important role in explaining synaptic function and plasticity (Zucker and Regehr, 2002) and identifies N and p_{vr} as major functional determinants of the presynapse.

Functional readouts of N can be achieved through electrophysiological measurements, employing high-frequency electrical stimulation or fluctuation analysis of synaptic responses (Clements and Silver, 2000). Results obtained by either approach must, however, be interpreted carefully as additional factors complicate the analysis (Sakaba et al., 2002; Scheuss et al., 2002; Hosoi et al., 2007; Hallermann et al., 2010b). Hypertonic sucrose stimulation can be used as another technique to approximate N (Fatt and Katz, 1952; Rosenmund and Stevens, 1996). However, being independent of Ca^{2+} -triggered fusion, it remains uncertain whether hypertonically released vesicles are generally also readily released under physiological conditions (Moulder and Mennerick, 2005).

Alternatively, N can be defined as the number of release sites, in which case p_{vr} denotes the probability that a vesicle will fuse at a given site (Schneggenburger et al., 2002). Nerve terminals vary greatly in size and correspondingly contain between one [e.g. at certain cortical synapses; (Xu-Friedman et al., 2001)] and many hundred AZs [e.g. at the Calyx of Held; (Sätzler et al., 2002)]. It is therefore helpful to view the AZ as a fundamental unit of presynaptic function (Alabi and Tsien, 2012). That said, morphology and function of AZs are highly heterogeneous (Zhai and Bellen, 2004),

also varying within one and the same neuron (Atwood and Karunanithi, 2002; Peled and Isacoff, 2011). Accordingly, functional approximations of p_{vr} at central mammalian synapses have reported both AZs operating with uniquantal release and AZs capable of multivesicular release (Tong and Jahr, 1994; Auger et al., 1998; Silver et al., 2003). To date, this next level of AZ organization has been difficult to study as specific molecular markers or structural correlates of release sites remain uncertain.

Functional estimates of p_{vr} can be obtained employing several methods that provide relative or absolute values. These include electrophysiology-based approaches such as paired-pulse stimulation or fluctuation analysis (Clements and Silver, 2000; Sakaba et al., 2002; Zucker and Regehr, 2002) and dynamic optical readouts of exocytosis or postsynaptic activation (Branco and Staras, 2009; Zhang et al., 2009; Peled and Isacoff, 2011; Marvin et al., 2013). Since p_{vr} is highly Ca^{2+} -dependent, its value for a given SV will be strongly influenced by the distance to voltage-gated Ca^{2+} channels at the AZ (Neher, 1998; Eggermann et al., 2012). Given their major significance for synaptic transmission, detailed understanding of Ca^{2+} channels and their spatial arrangement in relation to SVs would be desirable to improve our mechanistic understanding of AZ structure-function relationships.

2.2 *Drosophila melanogaster*

2.2.1 Background

Research on *Drosophila melanogaster*, commonly known as the fruit fly, has substantially contributed to our understanding of neuroscience (Bellen et al., 2010). Today, *Drosophila* is one of the most valuable organisms to study synapse physiology, plasticity and development (Budnik and Ruiz-Canada, 2006; Frank et al., 2013).

One beneficial aspect of working with *Drosophila* is certainly the great variety of sophisticated genetic tools, most of which trace back to detailed studies from 1910-1960 and have since been permanently developed further (Bellen et al., 2010). The introduction of the bipartite UAS (upstream activating sequence)/Gal4 system, which originally derives from yeast, and the related LexA/LexAop and Q systems (Lai and

Lee, 2006; Potter et al., 2010) into *Drosophila* allows ectopic gene expression in almost any cell or tissue of interest (Brand and Perrimon, 1993). Using these binary expression systems, e.g. RNA interference as one strategy to reduce gene expression in distinct cells can be accomplished with ease (Dietzl et al., 2007; Ni et al., 2009). Due to its genetic accessibility gene addition or removal in *Drosophila* is comfortably possible, using a random approach of insertion or chemical mutagenesis (Lewis and Bacher, 1968) respectively, or directed methods, which affect the locus of interest (Rong et al., 2002; Bellen et al., 2004; Venken and Bellen, 2005). Additionally, the rapid generation of transgenic flies is possible and thousands of fly lines exist that can easily be shared within the scientific community (The FlyBase Consortium, 2003).

Viewed from a practical perspective, *Drosophilae* are small, easy to handle, have a short life cycle and can be cost efficiently kept in large numbers. Usually, flies are maintained in either small or large vials (Figure 4b) with homemade egg-laying medium to serve adults and larvae with food.

Figure 4a depicts the life cycle of flies at 25°C. Following the deposition of fertilized eggs (~ 0.5 mm long), larvae will hatch after one day to develop to first, second (lasting 1 day each) and third instar larvae (lasting 2 days). After the third larval stage, drastic changes in morphology and physiology occur during pupation, which lead to tissue replacement, derived from larval imaginal discs. Eclosion takes place on day 9. After flies reach sexual maturity, the cycle begins anew.

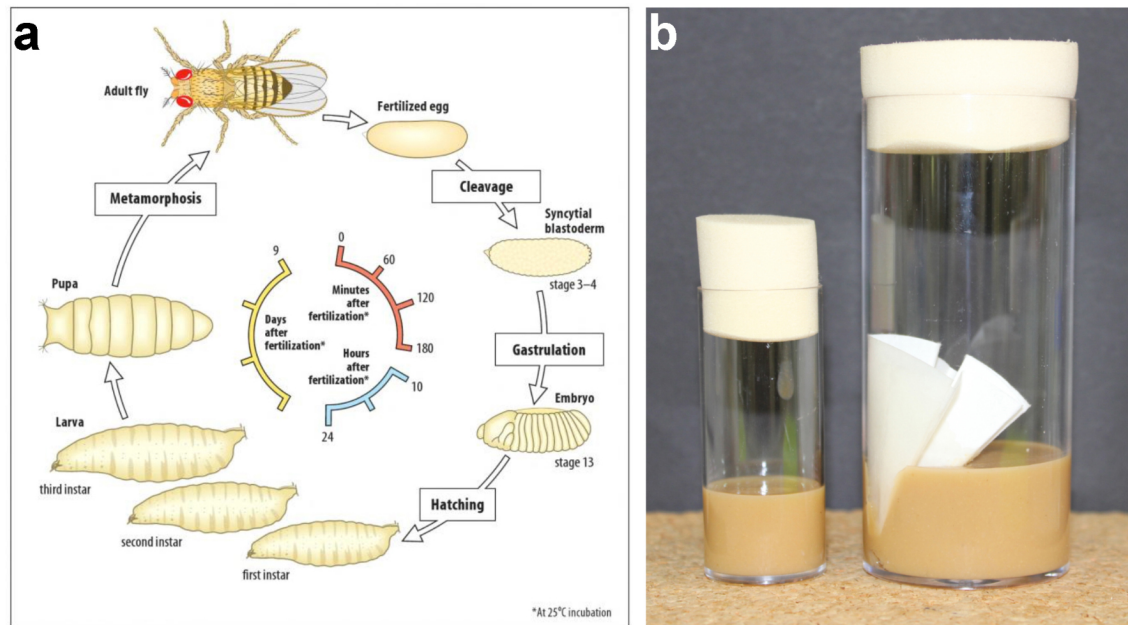


Figure 4 *Drosophila melanogaster*. (a) Life cycle of *Drosophila melanogaster* at 25°C. Modified from Wolpert and Tickle, 2011. (b) Culture vials for *Drosophila* breeding with egg-laying medium: small (34 ml) and large vial (174 ml).

2.2.2 Anatomy and physiology of the neuromuscular junction

The development of the embryonic *Drosophila* NMJ typically starts 13 hours after egg laying as soon as the innervating nerve contacts the muscle surface and ends when neuronal processes reach their final positions and synaptic swellings, so called boutons that harbour synapses are established (Saitoe et al., 1997; Budnik and Ruiz-Canada, 2006). During larval life, the muscle surface area increases 100-fold, which is accompanied by considerable increase in motor neuron arborizations and terminals (Keshishian et al., 1993) as well as an elevated synapse number per bouton (Schuster et al., 1996) and a larger number of vesicles within individual boutons (Prokop, 1999).

The *Drosophila* neuromuscular system consists of approximately 400 striated muscle fibers (Figure 5) each containing 10-20 nuclei that are arranged in a row on the surface of the muscle (Jan and Jan, 1976a). In the present work, most investigations were conducted on ventral longitudinal muscles (VLM) 6/7 in abdominal segments A2 and A3 of third instar larvae. At this stage VLM 6/7 is 400µm long, 80µm wide and 25µm thick (Jan and Jan, 1976a). Segmental nerves that originate from the ventral nerve cord run down the periphery and approach the muscle on the ipsilateral side.

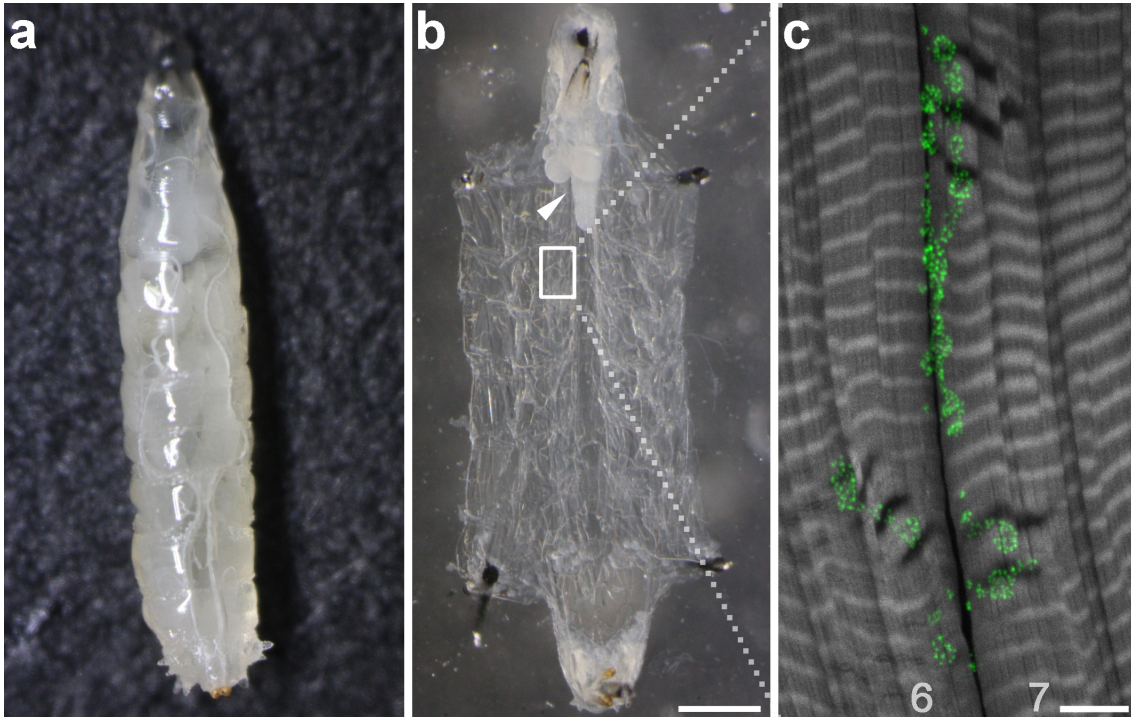


Figure 5 *Drosophila* neuromuscular system. (a-c) *Drosophila* third instar larva. (b) Body-wall preparation of a *Drosophila* larva with intact ventral nerve cord (arrowhead). The digestive and other internal organs were removed. Box denotes VLM 6/7 in abdominal segment A2. (c) Enlarged region shows muscles stained against phalloidin (grey) and presynaptic AZs visualized via Bruchpilot staining (mAb Brp^{Nc82}; green). Scale bars: (a,b) 500 μ m, (c) 10 μ m.

Drosophila muscles can be innervated by a maximum of three types of motor neurons that form type I, II, or III endings on their target muscles. Type I motor neurons form large boutons that are typically 1-5 μ m in diameter and contain the excitatory neurotransmitter glutamate [Figure 6; (Jan and Jan, 1976b)], though two additional peptidergic compounds have also been communicated (Anderson et al., 1988; Keshishian et al., 1993; Zhong and Peña, 1995). Type II endings usually possess more branches and can extend over a larger muscle area. Their boutons are smaller (\sim 1 μ m) and use glutamate as well as octopamine for neurotransmission (Monastirioti et al., 1995). Additionally, nerve endings exist that are almost deprived of glutamate containing vesicles and include instead round dense core vesicles, which represent peptidergic type-III endings and can be found on muscle 12 (Jia et al., 1993).

The *Drosophila* nerve muscle preparation (Figures 5, 6), which is commonly used for electrophysiology, is thin, almost transparent and accessible to experimental manipulations. Furthermore, *in vivo* imaging (Rasse et al., 2005), dye injection and uptake experiments, immunohistochemistry, EM studies, even Ca²⁺ imaging with

synthetic (Macleod et al., 2002) or genetically expressed indicators (Peled and Isacoff, 2011) can be accomplished (Sullivan et al., 2000). Due to the highly stereotyped structure of the *Drosophila* nerve muscle system, each muscle can be uniquely distinguished based on its position. Hence, NMJs can be reliably identified and quantitatively compared between individuals (Budnik and Ruiz-Canada, 2006).

The first to describe the physiology of larval *Drosophila* NMJs in detail were Jan and Jan (Jan and Jan, 1976a). In combination with a study by Stewart et al., the basis for electrophysiological measurements employing the *Drosophila* nerve muscle preparation was established (Stewart et al., 1994).

VLM6 has a cell capacitance of 2000-5000 pF and a typical membrane resistance of 5-10 M Ω (Stewart et al., 1994). The resting membrane potential (V_m) is approximately -54 mV and neither sensitive to changes in pH (between 6.8 and 7.3) nor osmolarity (between a relative tonicity of 0.88 and 1.12). V_m is dependent on external sodium and potassium concentrations and follows the Goldman-Hodgkin-Katz equation with a permeability coefficient of $P_{Na}/P_K = 0.23$. Furthermore, transmitter release is quantal and dependent on the fourth power of external Ca^{2+} (Jan and Jan, 1976a). Importantly, the excitatory neurotransmitter at this NMJ is glutamate (Jan and Jan, 1976b).

VLM 6 and 7 are innervated by two type-I motor neurons [RP3 and MN6/7b; (Keshishian et al., 1993)]. Whereas RP3 contributes big boutons (Ib), MN6/7b gives rise to small boutons (Is) on both muscles (Figure 6). In addition to these morphological differences (Atwood et al., 1993), type Is boutons give rise to larger excitatory junctional potentials that show less facilitation (Atwood et al., 1993; Kurdyak et al., 1994). Hence, type Is boutons are believed to exhibit a higher p_{vr} than type Ib. To elucidate the structural components that underlie and influence this physiological feature is highly interesting as can be seen later on.

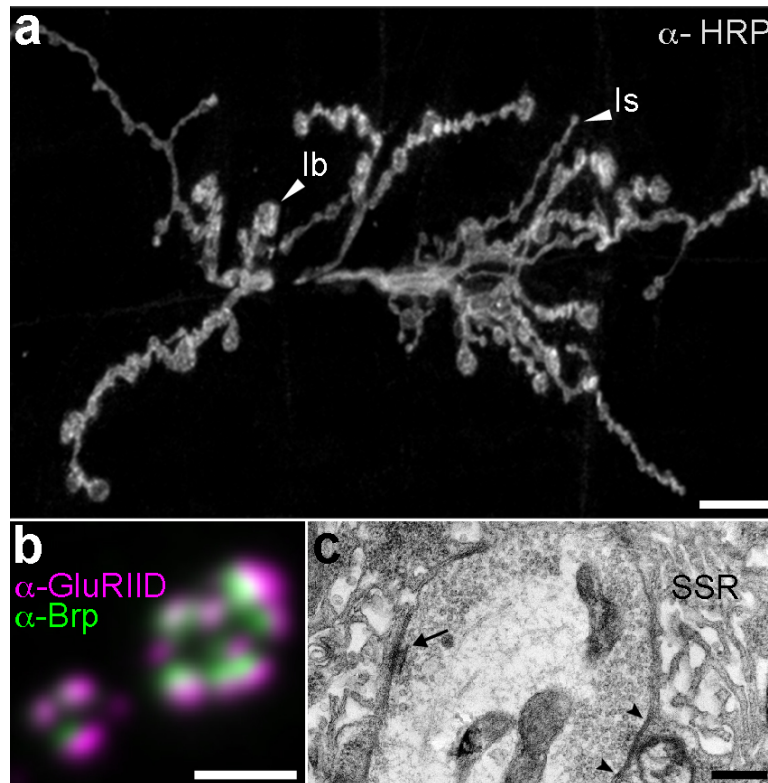


Figure 6 Synaptic structure of the *Drosophila* NMJ. (a) Confocal image of the glutamatergic NMJ stained against horseradish peroxidase (α -HRP) to label neuronal membranes. Arrowheads denote Ib and Is boutons. (b) Boutons labelled with antibodies against Brp (α -Brp; mAb Brp^{Nc82}; green) and the postsynaptic glutamate receptor subunit IID (α -GluRIID; magenta). (c) Electron micrograph shows the ultrastructure of a bouton surrounded by the subsynaptic reticulum (SSR). Arrowheads depict a synapse, which can be recognized by electron dense membranes on the pre- and postsynaptic side. Arrow shows an AZ T-bar that reaches into the cytoplasm. Electron micrograph provided by N.Scholz in collaboration with Brigitte Trost and Christian Stigloher. Scale bars: (a) 10 μ m, (b) 2 μ m, (c) 400 nm.

2.2.3 Active zones at neuromuscular junctions in *Drosophila*

2.2.3.1 Molecular composition and ultrastructure of the *Drosophila* AZ

This section focuses on key players of *Drosophila* AZs, part of which are main subjects of this thesis.

A major role of Liprin- α in *Drosophila* (DLiprin- α) is to control synapse morphogenesis at the NMJ (Kaufmann et al., 2002). Super-resolution imaging via STED (stimulated emission depletion) microscopy revealed the localization of DLiprin- α at the rim of presynaptic AZs, where it forms clusters [Figure 7d; (Fouquet et al., 2009)]. Interestingly, DLiprin- α seems to influence appropriate Brp localization, since DLiprin- α mutants exhibit complex multi-T-bar AZs (Kaufmann et al., 2002) and atypically

shaped Brp clusters (Fouquet et al., 2009). For correct localization of DLiprin- α , *Drosophila* Syd-1 (Dsyd-1; synapse defective-1) is necessary (Owald et al., 2010). DSyd-1, as well, was shown to reside at the rim of the AZ and to organize Brp localization [Figure 7d; (Owald et al., 2010)]. Functionally, DSyd-1 mutant *Drosophila* larvae possess fewer release sites, which is accompanied by decreased evoked synaptic currents. In contrast to DLiprin- α that might solely function presynaptically DSyd-1 also regulates the accumulation of postsynaptic glutamate receptors trans-synaptically (Owald et al., 2010).

RIM (Rab3 interacting molecule) is truly a multitalent at AZs as it can bind to a variety of proteins including Liprin- α , Munc13, RBP and Ca²⁺ channels. However, its role at *Drosophila* AZs was only recently identified (Graf et al., 2012). Here, RIM increases Ca²⁺ channel density to ensure synaptic efficacy and regulates the size of the RRP (Graf et al., 2012). In contrast to its role in mammals and *C. elegans*, where it interacts with CAST/ERC/ELKS (Ohtsuka et al., 2002; Wang et al., 2002; Deken et al., 2005), RIM does not seem to influence Brp, the *Drosophila* homolog of CAST/ERC/ELKS (Graf et al., 2012).

Derived from experiments in cell culture, RBP conducts an important linker function at AZs in connecting Ca²⁺ channels to RIM, which itself contacts Rab3 on the SV. Therefore, it was hypothesized that RBP might control the strength of neurotransmission by linking the fusion machinery to AZ tethering mechanisms (Hibino et al., 2002). Consistent with its function in the mammalian system, analysis in *Drosophila* confirmed the enrichment of RBP at presynaptic terminals, where it is localized in close proximity to Brp, surrounding a field of AZ Ca²⁺ channels [Figure 7d; (Liu et al., 2011)]. Here, studies of RBP mutants showed atypically shaped electron-dense material but no regular T-bar structures. Functionally, RBP mutants exhibit strongly decreased excitatory postsynaptic currents with altered short-term synaptic plasticity (STP) and a reduced quantal content (Liu et al., 2011). Moreover, synaptic currents seem to be desynchronized from incoming stimuli, which fits well with the previously identified role of RBP in localizing Ca²⁺ channels.

The heart of the AZ is formed by Brp, a protein of roughly 200 kDa, which was initially identified via mass spectrometry using an antibody derived from the Würzburg

hybridoma bank that is a large collection of antibodies obtained from *Drosophila* head-extracts (Hofbauer et al., 2009). Brp contains numerous coiled coil rich domains especially in its C-terminal region (Wagh et al., 2006) and is an integral part of the *Drosophila* T-bar (Kittel et al., 2006; Wagh et al., 2006; Fouquet et al., 2009). Derived from EM analyses, T-bars exhibit an irregular shaped pedestal (80-240 nm width) with a total height of ~ 50 nm from which extension arise approximately 150-170 nm into the cell (Jiao et al., 2010; Matkovic et al., 2013).

Brp itself adopts an elongated polarized conformation within the CAZ reaching with its C-terminus into the cytoplasm, while the N-terminal region is located in close proximity to the presynaptic plasma membrane in the region of the T-bar core overlaying AZ Ca²⁺ channels [Figure 7b, d; (Fouquet et al., 2009; Maglione and Sigrist, 2013)]. Correspondingly, EM-tomography analysis reported so-called ‘legs’, which present putative Ca²⁺ channels that are attached to the pedestal, with a spacing of 20-25 nm from each other [Figure 7b; (Jiao et al., 2010)]. In Brp null mutants (*brp*⁶⁹), synapses are completely deprived of electron dense projections (Figure 7c), confirming that Brp is a direct component of the T-bar and display mislocalized Ca²⁺ channels, clearly indicating a role of Brp in AZ Ca²⁺ channel clustering (Kittel et al., 2006). Application of HPF (high-pressure freezing) to *Drosophila* AZs allowed visualizing the filamentous ultrastructure of Brp’s C-terminal part (Fouquet et al., 2009), which, when seen *en face* (optical axis perpendicular to the AZ membrane) in STED microscopy, builds up ring-like structures forming discrete clusters [Figure 7a; (Kittel et al., 2006; Fouquet et al., Liu et al., 2011)]. Furthermore, the combination of HPF with EM-tomography (Figure 7b) demonstrated that the C-terminal filaments assemble to striated 10 nm thick structures, suggesting that they are made of bundles of filaments. Moreover, this study could show that two pools of SVs are associated with T-bars. One pool is linked to the presynaptic membrane, while the other connects to SVs around the T-bar, indicating that SVs loose their connection to other vesicles while they move closer to release sites (Jiao et al., 2010). Relatedly, investigations on a C-terminally truncated version of Brp (*brp*^{nude}) revealed a severe defect in the vesicle tethering capacity of T-bars (Figure 7c), thereby showing that the last 17 C-terminal amino acids of Brp are necessary to attach SVs (Hallermann et al., 2010c). By employing STED microscopy to map the localization of Brp in relation to RBP it was shown that, while Brp contributes T-bar

filaments, RBP surrounds the central core, most likely shaping the electron dense T-bar pedestal [Figure 7d; (Liu et al., 2011; Maglione and Sigrist, 2013)]. Recently, the application of super-resolution microscopy and EM to two major Brp isoforms, namely Brp-190 and Brp-170, demonstrated that both are necessary for proper assembly of the T-bar (Matkovic et al., 2013).

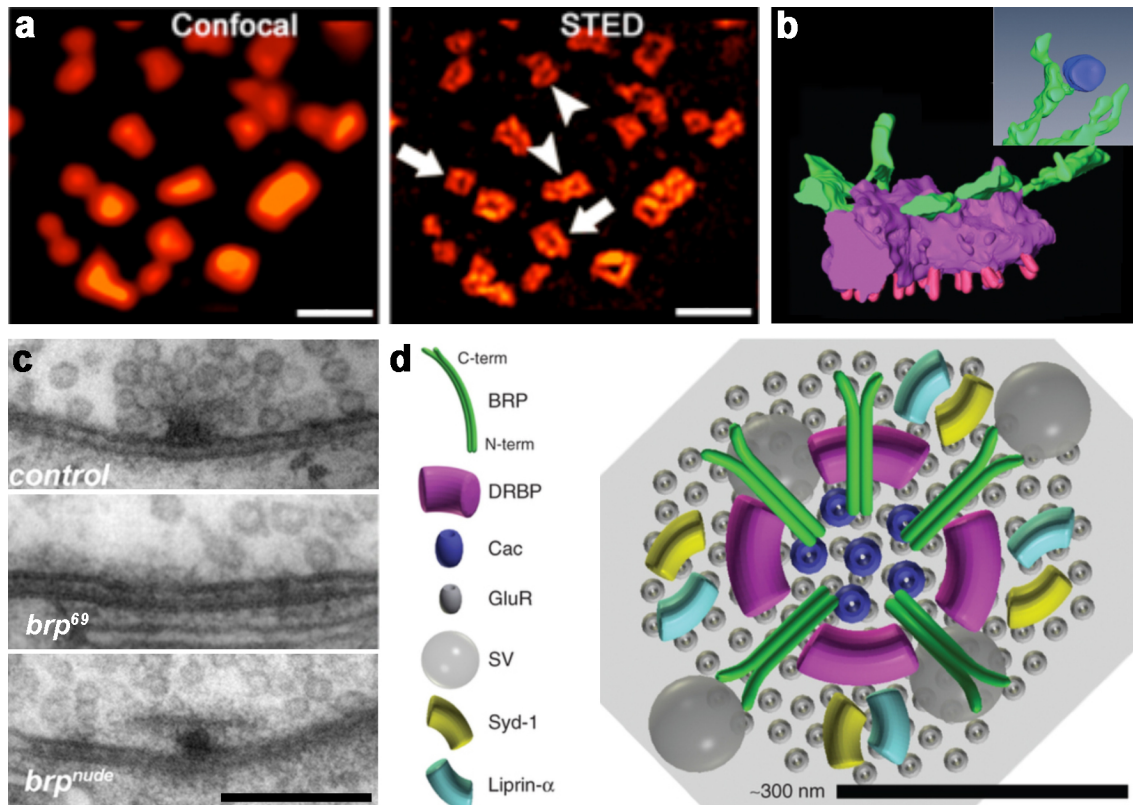


Figure 7 Ultrastructural composition of the *Drosophila* AZ. (a) Immunostaining against the C-terminal part of Brp in confocal (left) and corresponding STED microscopy (right; arrows: single ring, arrowhead: double-ring). Taken from Kittel et al., 2006. (b) Electron tomography of a T-bar shows the three main components: the central core (purple), extensions (green) and legs (pink). Inset depicts a Brp filament that attaches a SV (blue) via small connections. Modified from Jiao et al., 2010. (c) EM of AZs (side view) reveals structural phenotypes of *brp⁶⁹* (complete loss of T-bar) and *brp^{nude}* (naked T-bar). Taken from Fouquet et al., 2009 and Hallermann et al., 2010c. (d) AZ model (seen *en face*). Adapted from Maglione and Sigrist, 2013. Scale bars: (a) 1 μ m, (c) 200 nm.

Beneath the prominent *Drosophila* T-bar, the Ca^{2+} channel α 1-subunit cacophony can be found (Figure 7d). Analysis of a temperature-sensitive mutation of cacophony revealed a severe reduction in neurotransmitter release, indicating that cacophony functions in neurotransmission (Kawasaki et al., 2000; Kuromi et al., 2004). Surprisingly, the *Drosophila* locus for cacophony was first identified in a screen for changes in courtship songs (von Schilcher, 1976, 1977) before it was found to encode a

voltage gated Ca^{2+} channel $\alpha 1$ subunit (Smith et al., 1996) and a primary presynaptic Ca^{2+} channel in *Drosophila* (Dellinger et al., 2000; Kawasaki et al., 2000, 2002). The *cacophony* gene locus encodes a Ca^{2+} channels that is most similar to vertebrate N- and P/Q-type channels (Smith et al., 1996; Kawasaki et al., 2002; Rieckhof et al., 2003). Besides its role in neurotransmission, cacophony was also suggested to play a major role in the developmental regulation of neuronal excitability (Peng and Wu, 2007).

Rab3 is part of the SV cycle and belongs to a large family of GTP-binding proteins, which control intracellular transport processes (Südhof, 2004). Rab3 association and dissociation to SVs is tightly linked to synaptic exo- and endocytosis. Connected to SVs in its GTP-bound state, Rab3 undergoes hydrolyzation [GTP to GDP (guanosine diphosphate)] directly with or after vesicle fusion. Furthermore, Rab3 interacts with Rabphilin and RIM1 α /2 α to regulate neurotransmitter release (Südhof, 2004). In *Drosophila* the single Rab3 homolog was shown to be highly conserved and widely expressed throughout the nervous system (Johnston et al., 1991; DiAntonio et al., 1993). In 2009 Graf *et al.* published a study that dealt with a mutation in Rab3, named *rab3^{rup}* [*rup* stands for *running-unapposed*; (Graf et al., 2009)]. The mutation in the *rab3* locus derives from a genetic screen for AZ defects at the NMJ. Biochemical and immunohistochemical investigations demonstrated that *rab3^{rup}* behaves like a genetic null or strong hypomorph (Graf et al., 2009). Structural analysis showed that approximately 60% of GluR (glutamate receptor) clusters are not opposed to Brp positive AZs. Additionally, the number of AZs is severely decreased, while the remaining AZs are twofold larger. Further investigations revealed a high concentration of cacophony Ca^{2+} channels at remaining Brp positive AZs, while Brp negative AZs exhibit less Ca^{2+} channel immunofluorescence, suggesting a shift of AZ components to a small fraction of Brp-positive AZs. The number and distribution of SVs, however, seemed to be unaffected. In contrast to wildtype (wt) NMJs, where no or one T-bar is mostly found at AZs, *rab3^{rup}* NMJs showed a decrease in AZs containing one T-bar, while AZs with multiple T-bars were observed more frequently. The results indicate a function of Rab3 beyond its role in the SV cycle, namely in regulating and localizing presynaptic components at AZs (Graf et al., 2009).

2.2.3.2 Brp and Rab3 - Implications in synaptic plasticity

Synaptic plasticity can be described as a transient or persistent change in synaptic strength or efficacy following use-dependent activity. Synaptic plasticity exhibits a huge diversity, ranging from short to long periods of time, in which synaptic transmission can be depressed or enhanced (Citri and Malenka, 2008). Here, I will briefly summarize some of the major phenomena in synaptic plasticity and focus on the functional impact of Brp and Rab3 on STP.

Most models of learning and memory storage are based on Hebbian plasticity in terms of LTP (long-term potentiation) and LTD [long-term depression; (Abbott and Nelson, 2000)]. This is not surprising since there are several similarities between memory and synaptic plasticity: rapid generation, strengthening and prolongation by repetition, cooperativity, associativity and input specificity (Nicoll et al., 1988).

LTP was first discovered by Bliss and Lømo during their investigations on the rodent hippocampus (Bliss and Lømo, 1973), where they observed a long-lasting strengthening of all three major hippocampal pathways following high frequency stimulation. A very popular model of LTP is NMDAR (N-methyl-D-aspartate receptor)-dependent LTP. In contrast to AMPARs (α -amino-3-hydroxy-5-methyl-4-isoxazole propionic acid receptors) that contribute to most of the excitatory synaptic response when the cell is near its resting potential, NMDARs exhibit a high voltage dependency, which is attributed to a Mg^{2+} block within the channel at negative values. Therefore, NMDARs play a minor role during basal synaptic activity but can be activated when the cell is depolarized by removal of Mg^{2+} from its binding site. Once activated, NMDARs conduct sodium as well as Ca^{2+} ions. Especially the latter is associated with biochemical processes that might lead to induction of LTP, if a critical postsynaptic Ca^{2+} concentration is reached [(Mayer et al., 1984; Nowak et al., 1984); for a more detailed overview see (Citri and Malenka, 2008)]. In contrast, induction of LTD leads to activity-dependent long-lasting weakening of synaptic contacts by repetitive low frequency stimulation (Barrionuevo et al., 1980; Bear, 1999). Thus, these two processes provide an option for a bidirectional modulation of synaptic strength. However, despite intensive research, the detailed molecular mechanisms underlying long-term synaptic plasticity have yet to be elucidated.

STP is a change in synaptic strength lasting for milliseconds to minutes (Zucker and Regehr, 2002). STP is thought to play a crucial role in the adaption to sensory inputs, temporary behavioural changes and rapid modes of information storage (Citri and Malenka, 2008). An enhancement of synaptic transmission is usually connected to the accumulation of Ca^{2+} in the presynaptic cell, known as the ‘residual Ca^{2+} hypothesis’ [e.g. (Zucker and Regehr, 2002)]. In contrast, short-term synaptic depression is commonly associated with a transient depletion of RRVs, which leads to a decrease in the postsynaptic response (Zucker and Regehr, 2002). However, other mechanisms, e.g. the inactivation of voltage-dependent sodium or Ca^{2+} channels have also been proposed (Citri and Malenka, 2008). A frequently used paradigm to measure STP is the application of two stimuli with a very short interval, known as paired-pulse stimulation. In such an experimental setup, the response to the second stimulus can either be enhanced or depressed compared to the first one, reflecting synaptic facilitation or depression (Katz and Miledi, 1968; Zucker and Regehr, 2002). A popular model suggests that enhancement of synaptic responses is brought about by the summation of residual Ca^{2+} from the first stimulus and the newly invading Ca^{2+} from the second one, which leads to an increase in p_{vr} and SV fusion (Katz and Miledi, 1968). Additionally, other models explaining paired-pulse facilitation have been proposed, such as the ‘multi site (X-receptor) mechanism’ and the ‘partial Ca^{2+} buffer saturation mechanism’ (Burnashev and Rozov, 2005). The first one involves an additional Ca^{2+} binding site with high affinity and slow unbinding kinetics that functions together with the main sensor of release (Atluri and Regehr, 1996). The second option describes the local saturation of a fast endogenous Ca^{2+} buffer, which would lead to a progressive increase in free Ca^{2+} around the release sensor (Klingauf and Neher, 1997; Blatow et al., 2003; Felmy et al., 2003). Whether a synapse exhibits paired-pulse facilitation or not is dependent on its activity-history and its p_{vr} . Synapses with an initial high p_{vr} will likely show paired-pulse depression, while synapses starting with a lower p_{vr} tend to facilitate (Dobrunz and Stevens, 1997).

Brp is essential for structural and functional integrity of AZs. While the structural component of Brp was already discussed (see chapter 2.2.3.1), I will now focus on Brp function. Electrophysiological investigations showed that *brp*⁶⁹ as well as a panneurally driven *brp*-RNAi (ribonucleic acid interference; Wagh et al., 2006) exhibit a significant

decrease in evoked postsynaptic excitatory currents (eEPSCs) at low frequency stimulation. In *brp*⁶⁹ the amplitude of minis (miniature EPSCs), which reflects the spontaneous fusion of one vesicle, was significantly increased. This leads to a reduction in quantal content, indicating that the number of vesicles that get released per single presynaptic action potential is severely affected in *brp*⁶⁹ (Kittel et al., 2006). Additionally, the authors found a desynchronization of postsynaptic responses following nerve stimulation, which suggests an altered spatiotemporal presynaptic Ca²⁺ influx, resulting from changes in the distance between Ca²⁺ channels and SVs. Consistently, paired-pulse experiments showed a strong facilitation in *brp*⁶⁹ and application of the slow synthetic Ca²⁺ chelator EGTA further decreased eEPSC amplitudes, confirming the hypothesis that Brp functions in STP by clustering AZ Ca²⁺ channels. Additional investigations on a truncated Brp version, *brp*^{nude}, led to a more complex picture of Brp function (Hallermann et al., 2010c). *Brp*^{nude} is a hypomorphic *brp* allele that lacks the last 1% of the C-terminal amino acids of the protein. Though *brp*^{nude} exhibits a severe defect in vesicle tethering capacity, Ca²⁺ channel clustering and gross Brp localization was unaffected. While functional recordings at low frequency stimulation were unaltered, paired-pulse stimulation revealed a severe reduction of the second eEPSC at short interstimulus intervals, resulting in significant synaptic depression. Furthermore, high frequency stimulation at 60 Hz demonstrated a pronounced depression with a decreased steady-state level. By investigating recovery after synaptic depression, *brp*^{nude} exhibits a significantly slower initial phase, illustrating a role of Brp's vesicle tethering function in STP.

Interestingly, a recently conducted study on two Brp isoforms could not find any effect on STP by eliminating one isoform or the other (Matkovic et al., 2013). Moreover, combining paired-pulse experiments, fluctuation analysis, high frequency stimulation and modelling of STP, Weyersmüller and co-workers could find an increase in the amount of Brp during both life long and rapid presynaptic strengthening. This structural feature was accompanied by an elevated number of RRVs (Weyersmüller et al., 2011).

Taken these results together creates a concept in which Brp performs a dual function of clustering Ca²⁺ channels and concentrating SVs at neuromuscular AZs (Kittel et al., 2006; Hallermann et al., 2010c). By promoting excitation-secretion coupling, Brp

supports efficient transmitter release and shapes synaptic plasticity (Hallermann et al., 2010b; Weyhermüller et al., 2011). Moreover, Brp was also shown to participate in certain forms of learning (Knappek et al., 2011).

Information on Rab3 influencing STP in *Drosophila* is provided by Graf and colleagues (Graf et al., 2009). Here, electrophysiological measurements at low Ca^{2+} concentrations showed no change in eEPSC and mini amplitudes. Despite the apparent loss of Brp-positive AZs (see chapter 2.2.3.1), unaltered evoked synaptic release can be maintained at low frequency stimulation if the remaining sites of release possess a higher p_{vr} . Consistently, stimulation at 10 and 20 Hz revealed decreased synaptic facilitation compared to controls. Moreover, through rescue experiments, it could be shown that AZs are plastic in that altered protein distribution in *rab3^{rup}* can be rapidly and reversibly modified. Hereby, Rab3 increases the likelihood that Brp will cluster at an AZ. Hence, the authors conclude that Rab3 might be involved in synapse-specific plasticity by fast redistribution of Brp and associated CAZ constituents among individual AZs to influence neurotransmitter release (Graf et al., 2009).

2.3 Microscopy

2.3.1 Optical light microscopy

Optical light microscopy, particularly fluorescence and laser scanning confocal microscopy, permanently enjoys great popularity and a wide distribution in the life sciences. Today, technical improvements in fluorescence microscopy, the discovery and development of fluorescent proteins and progress in immunocytochemistry allow highly specific labelling of a vast majority of biological samples, cellular structures, proteins or genomic loci *in vitro* or *in vivo*, fixed or live (Conchello and Lichtman, 2005; Schermelleh et al., 2010; Tønnesen and Nägerl, 2013). However, determined by the wave-like nature of light, optical light microscopy is restricted in resolution to approximately half the wavelength of light, typically 250-300 nm in the x and y direction (Abbe, 1873). This limit is defined by diffraction and represents the smallest possible spot size that can be resolved employing a standard imaging system with focused light. In other words, objects that are smaller or separated by a shorter distance

than the diffraction barrier cannot be differentiated (Egner and Hell, 2005; Galbraith and Galbraith, 2011). Thus, fluorescence microscopy is the method of choice for selectively visualizing bio molecules with a high signal-to-background ratio (Lichtman and Conchello, 2005), but fails to uncover organizational principles at the molecular scale due to its diffraction-limited resolution.

2.3.2. Electron microscopy

To visualize structures on the nanometer scale, researchers have relied on EM. As the resolving power of a microscope is related to the wavelength of irradiation, EM offers substantially improved resolution by replacing photons through electrons. As electrons possess a shorter wavelength, resolution is increased (Leung and Chou, 2011). Unfortunately, the application of EM is restricted to lifeless, fixed and embedded biological structures.

The resolving power of EM at synapses was exemplified by a classical study, which used tomography to investigate the ultrastructure of the frog neuromuscular AZ. The results showed an intricate fine CAZ structure, which assembles a regular and precisely organized arrangement of SVs relative to Ca^{2+} channels at release sites [see chapter 2.1.1.1; (Harlow et al., 2001)]. Furthermore, alternative tissue preparation and fixation techniques have enabled analyses of filamentous AZ structures and their associated SVs in various organisms (Landis et al., 1988; Siksou et al., 2007; Jiao et al., 2010; Wichmann and Sigrist, 2010; Fernández-Busnadiego et al., 2013). As more substructural details are uncovered (Szule et al., 2012), knowledge of the underlying protein species becomes increasingly desirable. Immunogold labelling provides means to locate specific proteins in electron micrographs with nanometer resolution and has been used to examine the topology of AZs [e.g. (Limbach et al., 2011)]. However, specific labelling with antibody-coupled gold particles is inefficient and a compromise must be made between optimal tissue preservation and structural resolution. Consequently, the ideal microscope should combine the minimal invasiveness and efficient specific labelling possibilities of optical microscopy with the high spatial resolution of EM.

2.3.3. Super-resolution microscopy

Technologies that merge these features, at least to a certain extent, are collectively termed super-resolution microscopy (SRM; Figure 8). Based on their conceptions, these techniques can be classed in near-field and far-field methods with subdivisions based on their underlying basic principles that provide subdiffraction resolution.

Near-field scanning optical microscopy [NSOM; (Lewis et al., 2003)] and total internal reflection microscopy [TIRF; (Axelrod, 2003)] are methods for visualizing membrane near structures. NSOM increases resolution approximately 10-fold in x, y direction and > 100-fold in z direction by omitting lenses (Lewis et al., 2003). Here, an aperture much smaller than the wavelength of light is illuminated and scans the surface of a specimen with a penetration depth of roughly 100 nm. TIRF offers high axial resolution (~ 100 nm) through inserting a prism next to a substrate, e.g. a cover slip, which is illuminated at a specific angle where light is not directly spread through the substrate to the sample, instead creating an evanescent field (approximately 100 nm) that excites fluorophores in a thin layer of the sample (Axelrod, 2003; Garini et al., 2005).

Far-field approaches (Figure 8) include structured illumination microscopy (SIM), STED and single-molecule based localization microscopy methods such as photo-activated localization microscopy (PALM) and *d*STORM. All of these techniques bypass the diffraction barrier by temporally separating the fluorescence emission of individual fluorophores in a deterministic (SIM, STED) or stochastic manner (PALM, *d*STORM).

SIM relies on patterned illumination of the specimen with a high spatial frequency in various orientations providing a lateral resolution of approximately 100 nm (Heintzmann and Cremer, 1999; Gustafsson, 2000). SIM does not depend on any specific fluorophore properties and can therefore be generally applied. A further modification of SIM, known as SSIM (saturated-SIM) exhibits higher spatial resolution but requires photostable samples (Gustafsson, 2005). As SIM enables multicolour 3D-imaging with standard fluorescent dyes, it has attracted considerable interest among biologists (Maglione and Sgrist, 2013).

In STED microscopy, the lateral resolution is improved by decreasing the size of the excitation PSF (point-spread function) by stimulated emission of fluorophores at the rim of the PSF (Hell and Wichmann, 1994). Since the resolution enhancement in STED microscopy scales with the intensity of the depletion beam (Hell, 2007) only very photostable fluorophores allow spatial resolutions in the 30-50 nm range (Hell, 2007; Meyer et al., 2008). STED is compatible with various fluorescent dyes including fluorescent proteins, allows direct image acquisition without the necessity for further image processing and is suited for live applications albeit at lower resolution (Hell, 2007; Nägerl et al., 2008; Schermelleh et al., 2010; Tønnesen et al., 2014).

Single-molecule based localization microscopy techniques such as PALM, STORM and *d*STORM rely on stochastic photoactivation, photoconversion, or photoswitching of fluorophores such that only a small subset emits photons at the same time. By fitting a 2D Gaussian function to the PSF of individual, spatially isolated emitters, their positions can be precisely localized and used to reconstruct a super-resolved image. A requirement therefore is, that all fluorophores determining the structure of interest have to be detected and localized at least once during image acquisition (Betzig et al., 2006; Hess et al., 2006; Rust et al., 2006; Heilemann et al., 2008). While PALM is conducted with genetically expressed photoactivatable fluorescent proteins (Betzig et al., 2006; Hess et al., 2006), STORM requires photoswitchable dye pairs (Rust et al., 2006) and *d*STORM takes advantage of the reversible photoswitching of standard organic fluorophores in thiol-containing aqueous buffer (Heilemann et al., 2008; van de Linde et al., 2011). Since localization microscopy methods exhibit explicit single-molecule sensitivity they share the potential to deliver quantitative information about molecular distributions, even reporting absolute numbers of proteins present in subcellular compartments (Sauer, 2013).

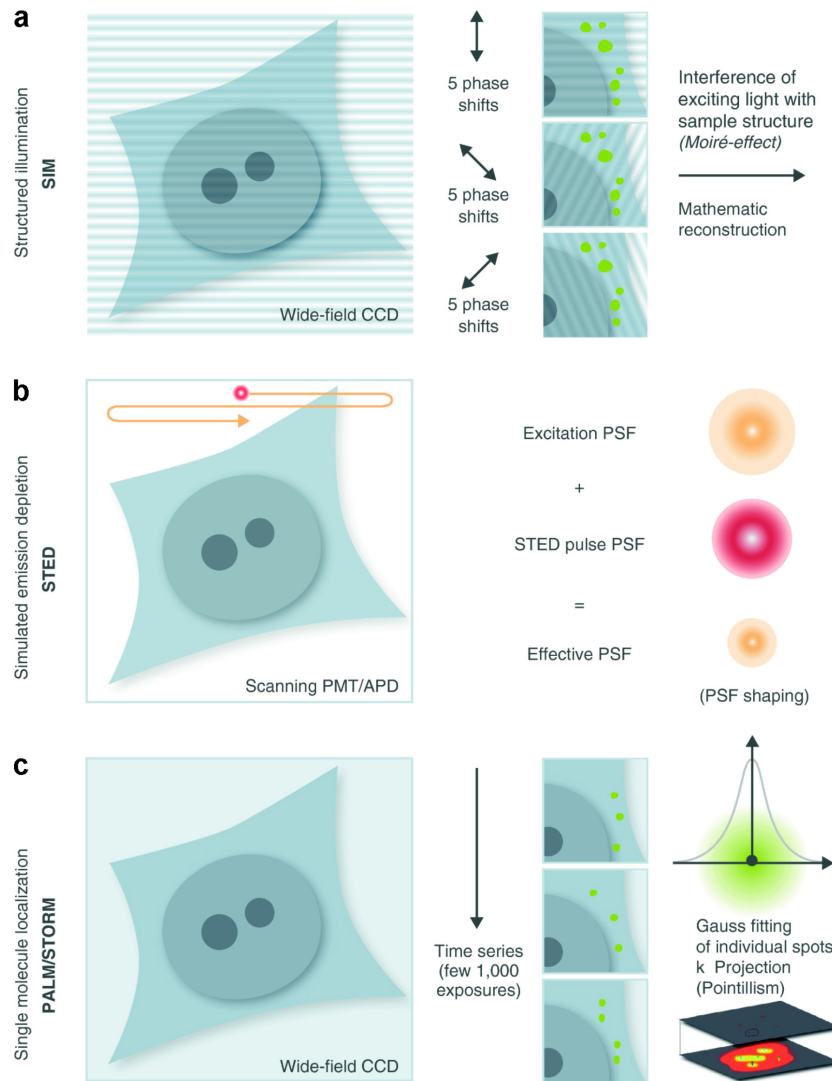


Figure 8 Super-resolution microscopy. (a) SIM relies on illumination of the sample employing an optical grid that forms striped patterns with a high spatial frequency. Imaging through the specimen generates an interference pattern (moiré fringes) that can be processed and mathematically reconstructed to obtain twofold increased lateral resolution. (b) STED microscopy utilizes stimulated emission to generate a reduced PSF by depleting the fluorescent signal at the rim of the diffraction-limited spot. (c) Single molecule localization microscopy, like PALM and STORM, are based on stochastic emission of small subsets of fluorophores that can be localized with nanometer precision to reconstruct a super-resolved image. Modified from Schermelleh et al., 2010 and Sigrist and Sabatini, 2012.

2.3.3.1 Application in the neurosciences

In one of its first biological applications, STED microscopy revealed detailed insights into the distribution of the vesicular calcium sensor Synaptotagmin following exocytosis (Willig et al., 2006). Subsequent work on vesicle organization introduced live cell STED imaging to interrogate SV movement within presynaptic boutons (Westphal et al., 2008) and multicolour imaging to differentiate SV pools (Kempf et al.,

2013). Focussing on Syntaxin as a component of the vesicle fusion machinery, several independently conducted investigations using STED and *d*STORM provided detailed information on its clustered arrangement at the plasma membrane (Sieber et al., 2007; Bar-On et al., 2012). Moreover, 3D applications of STORM and PALM have been utilized to investigate Clathrin structures in the context of endocytosis (Jones et al., 2011; Sochacki et al., 2012).

The first application of STED *in situ* helped identify Brp as a major component of the *Drosophila* AZ (Kittel et al., 2006). Subsequent work described Brp's polarized orientation within the CAZ and resolved the organization of further AZ constituents relative to Brp [Figure 7; (Fouquet et al., 2009; Oswald et al., 2010; Liu et al., 2011)]. This has generated a detailed picture of the protein scaffold at *Drosophila* AZs (Maglione and Sigrist, 2013). In a separate effort, STORM was used to measure the axial positions of the AZ-specific proteins RIM1, Piccolo and Bassoon at synapses in mouse brain tissue (Dani et al., 2010) thus providing a molecular map of synaptic proteins.

2.4 Motivation of the study

Despite a gradually emerging comprehensive catalogue of proteins, we still lack basic knowledge to describe how the molecular arrangement of AZs gives rise to neurotransmission. Based on the wealth of biochemical and genetic studies on the molecular identity of AZ constituents, combined approaches are necessary to ultimately link structure with function.

Since AZs exhibit a high degree of structural and functional diversity (Rozov et al., 2001; Atwood and Karunanithi, 2002; Zhai and Bellen, 2004; Peled and Isacoff, 2011), which can be modified in an activity-dependent manner (Wojtowicz et al., 1994; Castillo et al., 2002; Matz et al., 2010; Weyhersmüller et al., 2011), they pose a formidable challenge to deciphering the molecular properties that influence synaptic output. However, as an AZ contains a variety of densely packed molecular components residing within a small sub-cellular area [in central synapses around 200-400 nm; (Siksou et al., 2007)], direct ultrastructural access to this nanodomain was hindered by

the diffraction-limited resolution of conventional light microscopy. Lately, the development of SRM offers resolutions well beyond the diffraction limit and bridges the gap between conventional light microscopy and EM (Hell, 2009; Patterson et al., 2010; Schermelleh et al., 2010; Galbraith and Galbraith, 2011; Sauer, 2013).

Though SRM holds great potential for elucidating structure-function relationships, little work has been done to correlate AZ structure with function. In addition to the high spatial resolution provided by SRM, localization microscopy can also deliver estimates of protein abundance, which at the moment are mainly obtained from fluorescence intensity measurements and therefore deliver only relative values. However, true quantitative information on endogenous protein copies in addition to their spatial organization is required for a comprehensive mechanistic understanding of synaptic communication.

In this thesis the temporal precision of electrophysiology was combined with the spatial accuracy of *d*STORM to test for structure-function relationships at the *Drosophila* AZ. A specific aim was to find out if the number and nanoscopic organization of Brp proteins can provide functional information on neurotransmission. Therefore an approach was developed that is based on conventional immunohistochemistry to extract quantitative information on Brp protein copies *in situ*. To induce different AZ states, which are structural or functional alterations in the molecular AZ architecture, *Drosophila* mutants were employed and electrophysiology was applied to functionally calibrate super-resolution images.

3. Materials & Methods

3.1 Fly stocks

For this study, the following genotypes were used:

- w^1 or w^{1118} (controls),
- $brp^{nude(5.38)}/df(2R)BSC29$ [brp^{nude} ; (Hallermann et al., 2010c)]
- $rab3^{rup}/df(2R)ED2076$ [$rab3^{rup}$; (Graf et al., 2009)]

Data were obtained from male 3rd instar *Drosophila* larvae raised at 25°C.

3.2 Electrophysiology

3.2.1 Two-electrode voltage clamp

Two-electrode voltage clamp (TEVC) recordings at the *Drosophila* NMJ were performed and analyzed by Xi Zhen Keung and are published in Ehmann et al., 2014.

TEVC is preferred to other voltage clamp techniques, when large and fast currents should be resolved. Usually two low-resistance pipettes are employed: one measures the voltage, the other one injects the current. Figure 9a shows a typical TEVC configuration. For clarity, some frequency dependent components were neglected (The Axon Guide, 2012).

In this configuration, a unity gain buffer amplifier (A1) records the membrane potential (V_m) via ME1 (voltage recording microelectrode). V_m will then be compared to a command potential (V_{cmd}) in A2 (negative feedback amplifier). Here, the voltage output corresponds to the difference (ϵ) between V_m and V_{cmd} and drives the current (I_{TEVC}) through ME2 (current passing microelectrode) into the cell to control the membrane potential. In other words, I_{TEVC} is indirectly proportional to the current that flows over the membrane (I). TEVC recordings were performed using an Axoclamp 900A amplifier (Molecular Devices). For eEPSCs the cells were clamped to -60 mV (for the

sake of clarity, stimulation artefacts were removed in figures), minis were recorded at - 80 mV. All electrophysiological measurements were obtained from muscle 6 (segments A2 and A3; Figure 9b, c) at room temperature with intracellular electrodes (resistances of 10-20 M Ω , filled with 3M KCl) essentially as previously reported (Hallermann et al., 2010b).

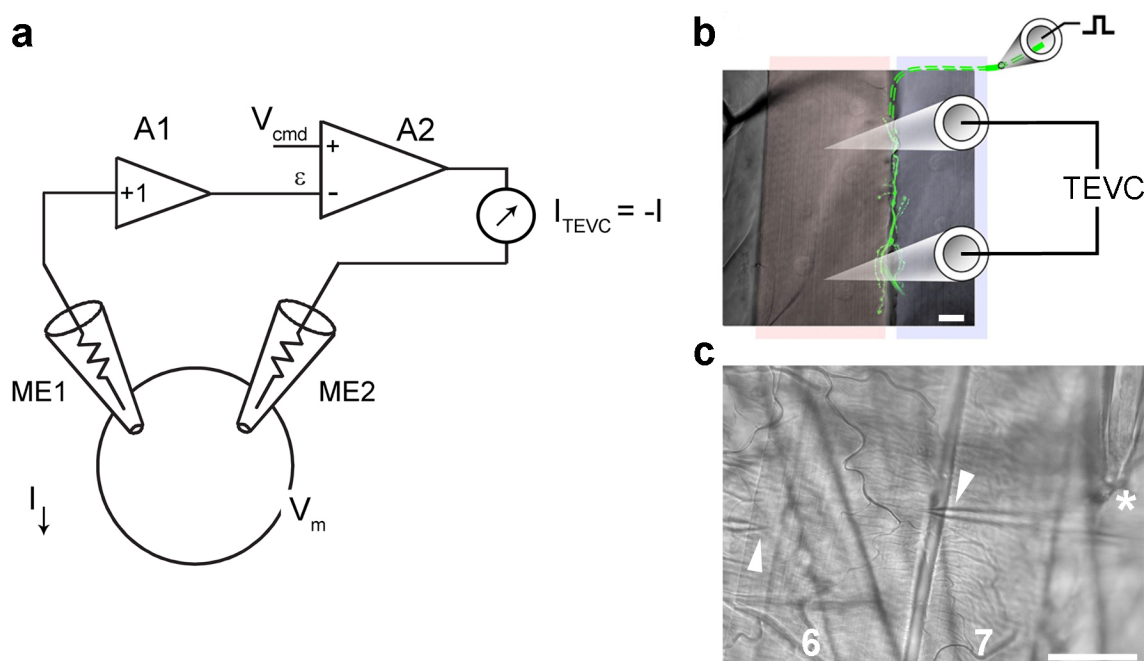


Figure 9 Two-electrode voltage clamp and its application at the *Drosophila* NMJ. (a) Schematics of a conventional TEVC configuration. ME1 (voltage-sensing electrode) records the voltage through A1 (unity gain amplifier), which is fed into A2 (negative feedback amplifier), where V_m is compared to V_{cmd} (difference ϵ). A2 injects the current I_{TEVC} that is required to keep V_m at V_{cmd} via ME2 (current electrode) into the cell. Modified from The Axon Guide, 2012. (b) Image of VLM 6 (red) and 7 (blue) overlaid with a confocal image of motor neurons that express GFP (green fluorescent protein). Positions of both intracellular microelectrodes and the suction electrode are indicated. Adapted from Hallermann et al., 2010b. (c) TEVC configuration during a live measurement at the *Drosophila* NMJ. The image shows VLM 6 and 7 (indicated by numbers), two intracellular electrodes (arrowheads) and the suction electrode with absorbed innervating nerve (asterisk). Scale bar: (c) 50 μ m.

Muscle cells with an initial membrane potential between - 50 and - 70 mV and input resistances of ≥ 4 M Ω were accepted for analysis. Signals were sampled at 10 kHz, low-pass filtered at 1 kHz and analyzed using Clampfit 10.2 (Molecular Devices). EPSCs were evoked by stimulating the innervating nerve [300 μ s pulses typically at 10 V; Grass S88 or S48 stimulator (Astro-Med Inc.) via a suction electrode (Figure 9b, c).

Ten eEPSCs were averaged per cell for each paired-pulse interval and for low frequency stimulation. Paired-pulse recordings were made at 0.2 Hz with inter-stimulus intervals

of (in ms): 10, 30, 100, 300 and 1,000. 10 s of rest were afforded to the cell in between recordings. The amplitude of the 2nd response in 10 ms inter-pulse recordings was measured from the peak to the point of interception with the extrapolated 1st response. High frequency stimulation followed an established protocol (Wu et al., 2005; Hallermann et al., 2010b) consisting of 100 pulses applied at 60 Hz. The recovery was monitored by stimulating at increasing intervals following the train (in ms): 25, 50, 100, 200, 500, 1000, 2000, 5000, 10000, 20000, 50000 and 100000.

All electrophysiological experiments were performed in extracellular haemolymph-like solution [HL-3; (Stewart et al., 1994)]. 1.5 mM CaCl₂ was added to the solution prior to recordings.

HL-3	
70 mM NaCl	1.06404, Merck
5 mM KCl	1.04933, Merck
20 mM MgCl ₂	1.05833, Merck
10 mM NaHCO ₃	S6297, Sigma Aldrich
5 mM D-(+)-Trehalose	T5251, Sigma Aldrich
115 mM Sucrose	S9378, Sigma Aldrich
5 mM HEPES	54457, Sigma Aldrich
1.5 mM CaCl ₂	21097, Fluka Analytics
pH was adjusted to 7.2 using 1 Mol NaOH	

3.2.2 Modelling

Short-term plasticity modelling of 60 Hz trains and of the recovery thereafter was performed by Stefan Hallermann and Annika Rings, University of Leipzig, as previously described (Hallermann et al., 2010b; Weyhersmüller et al., 2011) and results are published in Ehmann et al., 2014. In short, two different models were used. Model 1

is characterized by the following parameters: p_{vr} , the vesicular release probability, N , the number of readily releasable vesicles, N_0 , the number of vesicles in the supply pool from which the readily releasable pool is refilled, and k_{+1} , k_{-1} , k_{+0} and k_{-0} , the refilling rates of N and N_0 , respectively.

In model 2, a small pool of release-ready vesicles (N_2) with a high release probability (p_{vr2}) is refilled with a rate k_2 from a larger pool (N_1), which has a lower vesicular release probability (p_{vr1}), and which, in turn, is refilled from a supply pool (N_0). The refilling rates of these pools (k_{+1} , k_{-1} , k_{+0} and k_{-0}) are defined as in model 1.

The release probabilities (p_{vr} for model 1 and p_{vr1} and p_{vr2} for model 2) were defined according to a biophysical Ca^{2+} -dependent model of facilitation with one single free parameter (α) (Trommershäuser et al., 2003; Hallermann et al., 2010b). Both models had two additional free parameters: N for model 1, N_1 for model 2, and k_{+1} for both models, resulting in three free parameters for each model. The remaining parameters were constrained to values previously estimated at the *Drosophila* NMJ (Hallermann et al., 2010b) with the facilitation parameter (γ) (Trommershäuser et al., 2003) adjusted to $0.4 \mu\text{M}^{-1}$ to reproduce the initial facilitation observed here with an extracellular Ca^{2+} concentration of 1.5 mM.

Individual experiments including depression during 60 Hz train stimulation and the recovery from depression were fitted with either model 1 or model 2 as previously described [Table 3; (Hallermann et al., 2010b)]. The best-fit parameters for both models are shown for each individual experiment of the different genotypes as mean and standard error of the mean (SEM) in Figure 19b.

3.3 Confocal imaging

3.3.1 Immunohistochemistry and image acquisition

In principle, immunohistochemistry was performed as previously described (Schmid and Sigrist, 2008). Male 3rd instar *Drosophila* larvae were dissected in ice-cold HL-3, fixed for 10 min using 4% paraformaldehyde (PFA) in 0.1 M phosphate buffered saline (PBS) and blocked for 30 min in PBT [PBS with 0.05% Triton X-100 (T8787, Sigma)] containing 5% normal goat serum [NGS; (005-000-001, Jackson ImmunoResearch)]. Preparations were incubated with primary antibodies at 4°C over night. After one short and three x 20 min washing steps with PBT, secondary antibodies (in PBT, containing 5% NGS) were added to the fillets and incubated for 2 h at room temperature. Another three washing steps with PBT followed this. The samples were mounted in Vectashield (H1000, Vector Laboratories).

Primary antibodies were used in the following dilutions: mAb Brp^{Nc82} (1:250, provided by E. Buchner) and rabbit-GluRIID (1:1000, provided by S.J. Sigrist). Alexa Fluor 488-conjugated mouse (A11029, Invitrogen) and Cy3-conjugated rabbit (111-165-003, Dianova) antibodies were used at 1:250. Images were acquired with a Zeiss LSM5 Pascal confocal system (objective: 63x, NA 1.25, oil). For each set of experiments all genotypes were stained in the same vial and imaged in one session. To estimate synapse numbers laser power was adjusted individually for each NMJ.

10x PBS

74 g NaCl	1.06404, Merck
-----------	----------------

12.46 g Na ₂ HPO ₄ *2H ₂ O	1.06580, Merck
---	----------------

4.14 g NaH ₂ PO ₄ *H ₂ O	1.06345, Merck
---	----------------

Fill up to 1 l with H₂O. For 1 x PBS dilute 1:10; pH was adjusted to 7.4 using 1 Mol NaOH or 1 Mol HCl.

For PBT add appropriate volume (0.05 %) of Triton X100 (T9284, Sigma Aldrich).

4% PFA in 1x PBS

8 g PFA

Merck 1.04005

150 ml H₂O

Dissolve PFA in H₂O, heat up to 55°C

2 N NaOH

Merck 1.09136; add some drops until solution becomes clear

20 ml 10x PBS

Fill up to 200 ml using H₂O; pH was adjusted to 7.4 using 1 Mol NaOH or 1 Mol HCl

3.3.2 Data analysis

Brp punctae and GluRIID clusters (NMJ 6/7, segments A2, A3) were examined using ImageJ software (National Institute of Health) in principle as previously described (Schmid et al., 2008). After background subtraction, a Gaussian blur (0.9 px standard deviation) was applied to maximum z-projections of confocal stacks and masks were generated (threshold mean grey value of 25 for Brp and 30 for GluRIID). After superimposing the binary mask on the original blurred image, spot detection and segmentation via the 'Find Maxima' operation was performed to extract particle numbers.

To estimate the number of release sites (N) per active zone (AZ), the modelling prediction of N (average value of both models) was divided by the number of AZs on muscle 6 identified in confocal images, i.e. half of NMJ 6/7 (Atwood et al., 1993).

3.3 Super-resolution imaging

3.3.1 Antibody labelling and image acquisition

Super-resolution imaging of *Drosophila* AZs including data acquisition, analysis and quantification was done in collaboration with Markus Sauer, Sebastian van de Linde and Thorge Holm, University of Würzburg, and results are published in Ehmman et al., 2014.

The mAb Brp^{Nc82} was used at a dilution of 1/2000 to identify AZs. Goat anti mouse F(ab')₂ fragments (A10534, Invitrogen) were labelled with Cy5-NHS (PA15101, GE Healthcare) according to standard coupling protocols given by the supplier. In brief, Cy5-NHS was diluted in 100 µl DMSO (Dimethyl sulfoxide; 472301, Sigma Aldrich), and dehydrated (Savant Speed Vac, SC 110) to get a final concentration of 10 µg/µl. For antibody labelling, 1.7-2.4 µl Cy5-NHS (diluted in 100 µl DMSO), 50 µl F(ab')₂ fragments and 25 µl 150 mM NaHCO₃ were interfused. This mixture was kept for 60 minutes at room temperature in the dark to allow labelling reaction. Purification of conjugates (in 1x PBS) was performed using gel filtration columns (Sephadex G-25, GE Healthcare). The degree of labelling (DOL) was determined by absorption spectroscopy (Jasco) as 1.3 for studies of the CAZ ultrastructure and 1.3–1.5 for dilution experiments by application of the following equations:

$$(a) \quad c(IgG) = \frac{A(280) - A(650) \times cF(280)}{\epsilon(IgG) \times d} \quad (b) \quad c(Dye) = \frac{A(650)}{\epsilon(Dye, \max) \times d} \quad (c) \quad DOL = \frac{c(Dye)}{c(IgG)}$$

Equation 1 DOL determination. (a-c) $c(IgG)$ = antibody concentration; $A(280)$ = absorption at 280 nm and 650 ($A(650)$); $cF(280)$ = correction factor, for Cy5 usually 0.05; ϵ = molar extinction coefficient; d = cuvette size; $c(Dye)$ = dye concentration

Samples were stored in 0.2% sodium azide in PBS and for the experiments, Cy5 labelled secondary antibody was used at a concentration of 5.2×10^{-8} M.

For *d*STORM imaging with Cy5, the sample was embedded in photoswitching buffer, i.e. 100 mM mercaptoethylamine (MEA), pH 8.0, enzymatic oxygen scavenger system [5% w/v glucose, 5 U/ml glucose oxidase, 100 U/ml catalase (Schäfer et al., 2013)] and mounted on an inverted microscope (Olympus IX-71) equipped with an oil-immersion objective (60x, NA 1.45, Olympus) and a nosepiece stage [IX2-NPS, Olympus; (van de Linde et al., 2011)]. To excite Cy5 a 641 nm diode laser (Cube 640–100C, Coherent) was used. Telescope lenses and mirror were arranged on a translation stage to allow for switching between widefield, low-angle/highly-inclined-thin illumination, and total internal reflection fluorescence imaging (Sharonov and Hochstrasser, 2007; Tokunaga et al., 2008; van de Linde et al., 2011).

Fluorescence light from Cy5 was filtered by a dichroic mirror (650, Semrock) and a band- and longpass filter (BrightLine 697/75, RazorEdge 647, Semrock) and imaged on

an electron-multiplying CCD camera (EMCCD, Ixon DU897, Andor). Additional lenses were used to generate a final camera pixel size of 107 nm. 15,000 frames were recorded with a frame rate of 100 Hz at an irradiation intensity of $\sim 5 \text{ kW cm}^{-2}$. For imaging A488, a 488 nm laser (Sapphire 488 LP, Coherent) and a polychromatic dichroic mirror (410/504/582/669, Semrock) were used. Fluorescence light from A488 was reflected by a dichroic mirror (630 DCXR, Chroma) and imaged on a second EMCCD camera equipped with a bandpass filter (HQ535/50, Chroma).

Goat anti mouse IgG (Immunoglobulin G) labelled with A532 (A11002, Invitrogen) and A700 (A21036, Invitrogen) was used at a concentration of $6.25 \times 10^{-9} \text{ M}$. The degree of labelling was determined as 2.0 (A700) and 4.5 (A532). Prior to *d*STORM measurements samples were kept in PBT. Imaging of A532 and A700 by *d*STORM was performed in PBS buffer containing 100 mM MEA, pH 8.3. Using appropriate filter sets (dichroic mirrors: 650 or 545/650; bandpass filters: RazorEdge 647 or BrightLine 582/75, Semrock), the samples were irradiated at 641 nm (A700) or 532 nm (NANO 250-532-100, Linos; A532) at $\sim 5 \text{ kW cm}^{-2}$. For titrations of A532-labelled secondary antibodies (Figure 23) fluorescence light from A700 and A532 was separated by a dichroic mirror (630 DCXR, Chroma) and imaged on two EMCCD cameras.

3.3.2 Data analysis

Super-resolution images were reconstructed using the software package *rapid*STORM (Wolter et al., 2010, 2012). Only fluorescence spots containing more than 1000 photons were analyzed. Double-spot emission was analyzed by a two-kernel analysis as described (Wolter et al., 2011) applying a maximum two kernel improvement of 0.1. Raw localization data obtained from *rapid*STORM was examined and further processed with ImageJ. A sub-pixel binning of 10 nm / px was applied. Magnified views in Figure 10, 15 and 20 are shown with 7 nm binning for clarity.

To measure CAZ (defined by Brp^{Nc82}) area and localization numbers, masks were created by applying a Gaussian blur (1 px standard deviation) followed by a minimal threshold (0.15 counts). After a minimum overlay of the original data with the masks, CAZs were then identified via their area (300 px to infinity). For the comparison of genotypes, a total of 812 CAZs in controls, 776 in *brp*^{nude} and 257 in *rab3*^{rup} were

analyzed and data (presented as mean \pm SEM) were acquired in two imaging sessions, each containing all three genotypes stained in the same vial. Images with a background of more than 2.3 single spots per μm^2 were excluded from the comparative analysis. Unspecific background labels exhibited equal localization counts in all genotypes (average counts Control: 12.0 ± 0.2 localizations SEM, $n = 16$ NMJs; *brp^{nude}*: 12.0 ± 0.1 , $n = 13$; *rab3^{rup}*: 12.4 ± 0.3 , $n = 11$), indicating comparable imaging settings.

For the investigation of different motor neurons, a total of 963 (type Ib) and 579 (type Is) CAZs (from NMJ 6/7, segments A2 and A3) were analyzed to determine the structural gradient. Double-stainings included HRP directly conjugated to A488 [1:250 (123-545-021, Jackson ImmunoResearch)] for visualization of boutons. In the representative images, the epifluorescence signals were background subtracted and normalized.

To specify the localization precision of *d*STORM images, localizations of unspecific background label ($n=21436$) from all three genotypes were analyzed using ImageJ. Masks were created as described above (Gaussian blur with 1 px standard deviation, threshold 0.08 counts). Within a *d*STORM image, only selections with a size between 16 and 100 px (10 nm / px) and an ellipticity ≥ 0.95 were analyzed. The coordinates of localizations within a single selection were aligned to their centre of mass and a 2D histogram of all localizations (209537 in total) was generated (binning: 4 nm \times 4 nm). A 2D Gaussian function was fitted to this histogram (adjusted $R^2 = 0.995$). The standard deviation of the Gaussian function ($\sigma_{x,y} = (\sigma_x + \sigma_y) / 2$) was determined as 7.16 ± 0.02 nm and is stated as localization precision in this work (Figure 10a,b). This value is comparable to the localization precision obtained with an alternative method based on nearest neighbour analysis [NeNA; Figure 11; (Endesfelder et al., 2014)]. This method employs pairwise displacement distribution and makes use of the fact that a distinct localization in one imaging frame possesses a nearest neighbour localization in the following frame. By analyzing these localizations NeNA determines their precision. This analysis was performed by applying ‘Coordinate Based Localization Precision Estimator’, a Python script that can be found in Endesfelder et al., 2014, to localization data obtained by *rapid*STORM.

For the investigation of CAZ-units, those structures were chosen which were not grouped together and were viewed *en face* (Fouquet et al., 2009). For the manual selection of CAZ-units, the genotypes were blinded.

In collaboration with Stefan Hallermann and Annika Rings, University of Leipzig, the radial distribution (Figure 15g) was computed using Mathematica 9.0 (Wolfram Research) to automatically calculate the centre of each chosen CAZ-unit as the centre of mass (i.e. the average localization of all pixels of the CAZ-unit weighted with the pixel value). Subsequently, the distance of each pixel to the centre of mass was calculated. These distances were then binned, the pixel values were added to the corresponding bins and the values were normalized by the area of each radial slice. The resulting distributions were averaged across all chosen CAZ-units, resulting in mean and SEM values for the radial distributions of each genotype.

3.3.2.1 Cluster analysis

Cluster analysis was performed in collaboration with Uri Ashery and Amit Alon, Tel Aviv University, and results are published in Ehmann et al., 2014.

For the analysis a home-written density based algorithm was employed. The base of the algorithm comes from the known algorithm, DBSCAN (*Density Based Spatial Clustering of Applications with Noise*): this algorithm simply looks for localizations that reside within the middle of a circle of radius Eps and enclose at least k other localizations (Ester et al., 1996; Bar-On et al., 2012). Since the data contains a large number of localizations in between putative clusters, more constraints on cluster detection were added. The algorithm starts with finding local maxima of density. The density is defined as the number of localizations within an Eps radius circle around a localization (Eps -environment). Each local maximum that has a density that is more than k , will be defined as a cluster centre. For each cluster centre, the localizations contained within its Eps -environment are examined for holding the condition of k localizations. When the condition is held, the current localization along with all the other localizations within the Eps -environment, will become members of this cluster. The algorithm then moves on to another localization that was found within the circle of radius Eps from the cluster centre and examines if it holds the conditions. If not, this

localization will be a boundary point for the cluster and the expansion will end. If it does, this localization will be considered a core-object of the same cluster, and the cluster will keep expanding until it reaches a boundary point. In addition to the above conditions, each localization added to the cluster should have a lower density than the localization that discovered it. If the algorithm detects an increase in density, this localization will not be part of the previous cluster. This separates adjacent clusters and prevents creating saddle points between them.

A search Eps of 20 nm was chosen, which roughly corresponds to the estimated radius of an EM filament with the antibody complex attached to it. For a chosen Eps, the density is calculated as the number of localizations within the Eps-environment of the current localization. The parameter k was chosen based on the density distribution which had a peak around 12-18 and k was large enough to separate from noise but not too large as to find a sparse number of clusters ($k = 16$).

After defining the clusters and the non-clustered localizations, a set of different parameters that characterize the clusters was examined. The following cluster properties were analyzed: a) the number of localizations belonging to each cluster; b) cluster shape and area. Most clusters did not show an exact circular shape but were more elliptic. Therefore, a 2D ellipse was tightly fitted to each cluster. From this ellipse the parameters: shape (minor radius divided by major radius), minor and major axes were calculated. Clusters were defined as comprising a CAZ-unit if the density was at least four clusters within a circle of radius 200 nm.

3.3.3 Quantification of Brp protein numbers

To estimate the number of Brp molecules per CAZ-unit a number of parameters had to be considered. Firstly, the mAb Brp^{Nc82} specifically recognizes one epitope per Brp molecule. Secondly, it is unclear how many Cy5 labelled F(ab')₂ fragments can bind to the primary mAb Brp^{Nc82} and how many localizations can be expected per Cy5 labelled secondary antibody. Here, it has to be considered that the number of localizations detected per antibody can be strongly influenced by its nano-environment. Hence, the number of localizations expected for an individual labelled antibody should ideally be derived from measurements performed under identical imaging and buffer conditions in

the same cellular environment, i.e. within the CAZ. In order to derive quantitative values of Brp molecules from the localization data, antibody titrations with (i) different dilutions of Cy5 labelled secondary antibody and a constant concentration of mAb Brp^{Nc82} and (ii) different dilutions of mAb Brp^{Nc82} and a constant concentration of Cy5 labelled secondary antibody were performed.

To evaluate the localizations presented by a Cy5 labelled F(ab')₂ fragment attached to Brp via mAb Brp^{Nc82}, the concentration of mAb Brp^{Nc82} was kept constant (1/2000, i.e. experimental concentration) and the secondary antibody was diluted (1, 1/2, 1/10, 1/100, 1/1000, 1/10000, 1/100000). Preparations were simultaneously stained with A488 goat anti mouse F(ab')₂ fragments (A11017, Invitrogen) to warrant an overall constant secondary antibody concentration of 5.2×10^{-8} M for epitope saturation (e.g. 1: 100% Cy5 to 0% A488, 1/1,000: 0.1% Cy5 to 99.9% A488) and to enable the unequivocal identification of the CAZ at low Cy5 antibody concentrations (Figure 13b). The epifluorescence signal (A488) was background subtracted, blurred, and contrast enhanced to identify Cy5 localizations within in the CAZ. 8-10 NMJs were evaluated for each dilution and the localizations per CAZ were histogrammed and fit to a Poisson model in order to extract the average number of localizations per CAZ (L_{CAZ}) as the mean of the distribution. L_{CAZ} as a function of the Cy5 antibody dilution (d) was then approximated with the logistic function $L_{CAZ} = L_2 + (L_1 - L_2)(1 + (d/d_0)^p)^{-1}$ where the lowest localization value (L_2) is equivalent to the number of localizations corresponding to a single F(ab')₂ fragment attached to Brp via mAb Brp^{Nc82} (L_1 is the maximum localization value, p is the Hill coefficient, which was fixed to 1; Figure 13b). Such titrations are not limited to Cy5 but can, in principle, as well be performed with other fluorophore-labelled antibodies (Figure 24).

The saturation of mAb Brp^{Nc82} was analyzed by using a constant concentration of secondary antibodies (5.2×10^{-8} M) with a fixed ratio of Cy5 and A488 F(ab')₂ fragments (1% Cy5 : 99% A488) and by diluting the mAb Brp^{Nc82} (1/20, 1/50, 1/100, 1/200, 1/500, 1/1000, 1/2000, 1/5000, and 1/10000). The localization data was analyzed (4-5 NMJs per dilution) as described for Cy5 secondary antibody dilutions [Figure 13c; $L_1 = 198.9$, $L_{CAZ}(1/2000) = 70.6$].

In order to estimate how many Cy5 labelled secondary antibodies bind per primary mAb Brp^{Nc82} under experimental conditions (5.2×10^{-8} M Cy5, 100%), NMJs ($n = 5$) were stained with a very low concentration of mAb Brp^{Nc82} (1/20000) together with an antibody directed against an N-terminal Brp epitope [rabbit-Brp^{N-term} (Fouquet et al., 2009), provided by S.J. Sigrist, 1/2000; labelled by Alexa Fluor 488 goat anti rabbit (A11008, Invitrogen), 1/250]. Only solitary spots within CAZs defined via Brp^{N-term} were measured (threshold ≥ 10 px), histogrammed and fit to a Poisson model to extract the number of localizations corresponding to one mAb Brp^{Nc82} [L_E (Nc82)].

The application of the following equation:

$$\# Brp_{CAZ-unit} = \frac{Loc_{CAZ-unit}}{L_2(Cy5)} \times \frac{L_1(Cy5)}{L_{CAZ}(Cy5\ 100\%)} \times \frac{L_1(Nc82)}{L_{CAZ}(Nc82\ 1/2000)} \times \frac{L_2(Cy5)}{L_E(Nc82)}$$

Equation 2 Estimation of Brp molecules per CAZ-unit. From Ehmann et al., 2014.

gives an estimate of 137 ± 29 Brp molecules SEM at an average CAZ-unit. Correspondingly, the conversion factor 0.134 ± 0.028 SEM was used to translate localizations into molecules for all genotypes (Table 2).

3.4 Statistical analysis

Statistical tests were used as indicated. Data are presented as mean \pm SEM, unless otherwise stated. Levels of significance are identified by asterisks: * $P \leq 0.05$, ** $P \leq 0.01$, *** $P \leq 0.001$.

4. Results

4.1 Localization microscopy of the CAZ nanostructure

4.1.1 Application of *d*STORM to *Drosophila* AZs

Application of STED microscopy to the *Drosophila* AZ has led to a basic understanding of the structural arrangement of Brp within the CAZ (Kittel et al., 2006; Fouquet et al., 2009). Building upon this information, *d*STORM at *Drosophila* AZs was established to have a more thorough look at the molecular arrangement of Brp. Due to its explicit single molecule sensitivity, *d*STORM could provide detailed information on the spatial arrangement and in particular on the number of individual molecules.

The CAZ was recognized with a monoclonal antibody (mAb Brp^{Nc82}) that specifically labels an epitope at the C-terminal end of Brp (Wagh et al., 2006; Fouquet et al., 2009; Hofbauer et al., 2009). To optimize structural resolution secondary F(ab')₂ fragments were employed, which are 50% smaller than whole IgGs, and were labelled on average with 1.3 Cy5-fluorophores. For the whole antibody-fluorophore complex, a size of approximately 13 nm was estimated [primary IgG: 8-10 nm, secondary F(ab')₂: 4 nm; (Weber et al., 1978; Amiry-Moghaddam and Ottersen, 2013)]. The resolution that can be obtained with localization microscopy relies heavily on the photophysical properties of the fluorophore (e.g. its brightness) and the labelling density of the given structure (Patterson et al., 2010; van de Linde et al., 2011; Sauer, 2013). Owing to the high brightness of Cy5 a localization precision (= accuracy of position determination) of 6-7 nm [standard deviation (s.d.), in lateral direction] could be calculated by using either localizations of individual isolated fluorophore-labelled antibodies in the sample or nearest neighbour analysis [Figure 10a, b, Figure 11; Material and Methods; (Endesfelder et al., 2014)]. Interestingly, the increase in spatial resolution provided by *d*STORM revealed a substructural organization of AZs that was obscured in epifluorescence images (Figure 10c, d).

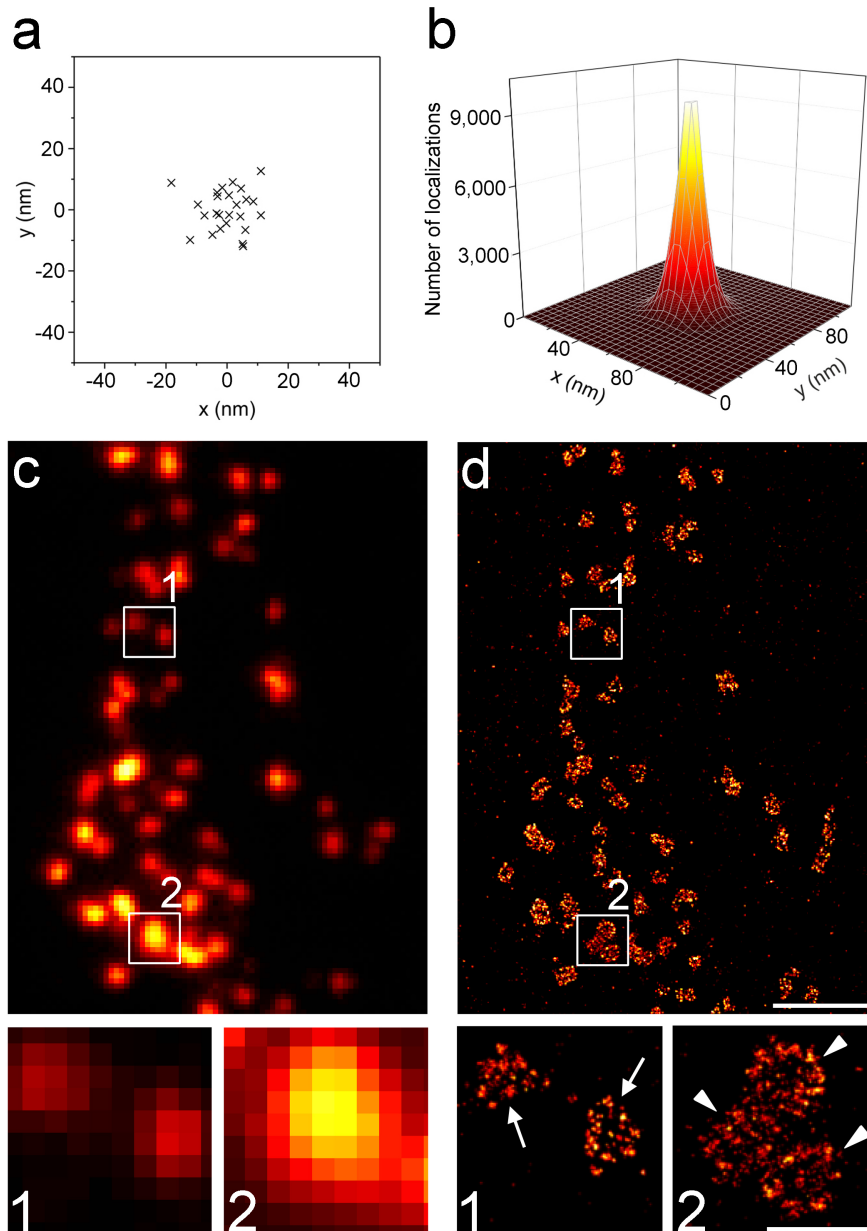


Figure 10 *d*STORM resolves substructural information on the CAZ. (a) 2D localization pattern of a single, unspecifically bound Cy5 F(ab')₂ fragment. (b) Aligned distribution of 209537 localizations from 21436 unspecifically bound antibodies. A 2D Gaussian fit gives a localization precision (s.d.) of 7.16 ± 0.02 nm. (c,d) *d*STORM images (right) of wt NMJs stained against Brp reveal CAZ substructures, hidden in epifluorescence images (left). Such subdivisions of Brp immunofluorescence are termed CAZ-units. d1 shows two individual AZs, each containing a single CAZ-unit (arrows). d2 depicts one AZ that contains 3 CAZ-units (arrowheads). Lower panels are magnifications of boxed regions. Scale bars: (c,d) 2 μ m, (c1,c2,d1,d2) 500 nm. From Ehmann et al., 2014.

Throughout this work, an AZ is defined via its CAZ as an interconnected region of Brp immunofluorescence. Within such a Brp assembly, a further level of organization could be identified in SRM images, which subclassifies Brp into modules. Therefore, one AZ

can contain a single (Figure 10d1) or several of these modules (Figure 10d2), which are termed CAZ-units (e.g. Figure 10d1 depicts two single AZs that are also individual CAZ-units; Figure 10d2 displays one AZ, comprising 3 CAZ-units).

A wt CAZ-unit viewed *en face* has a size of $0.095 \pm 0.003 \mu\text{m}^2$ SEM and comprises on average 1021 ± 43 SEM localizations (n= 144 CAZ-units; chapter 3. Materials and Methods).

To assure that such an organizational principle is not an artefact of fluorescence detection and localization, Brp immunostainings were performed using secondary antibodies with different fluorophores. Application of Alexa Fluor 700 (A700) and Alexa Fluor 532 (A532) resolved the same CAZ organization, although with a lower spatial resolution compared to Cy5 (Figure 11). Hence, Cy5 was used for all following experiments.

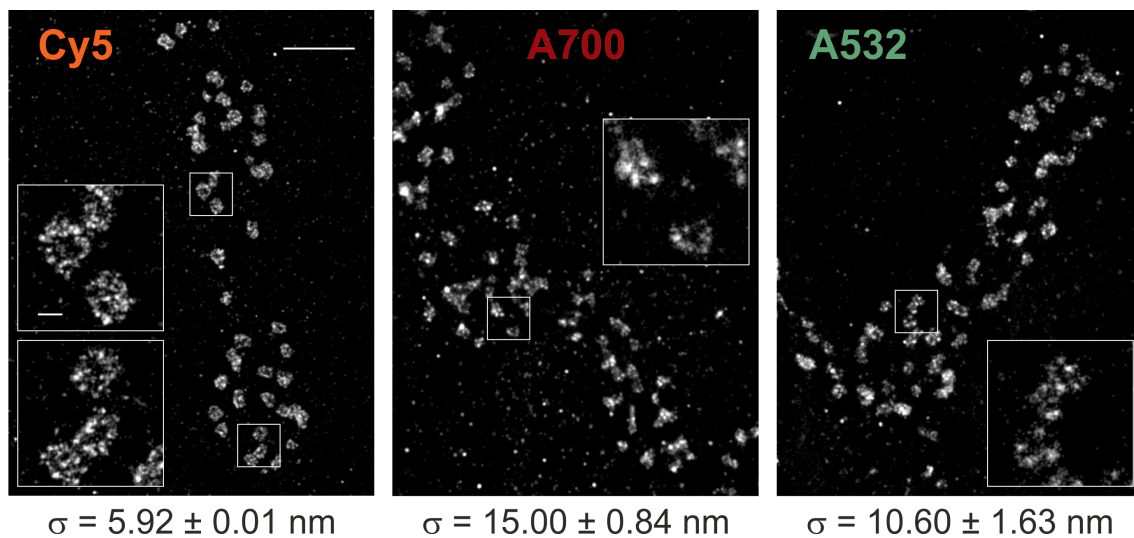


Figure 11 *d*STORM of wt CAZs with three different photoswitchable fluorophores. Using Cy5, Alexa Fluor 700 (A700) and Alexa Fluor 532 (A532) as photoswitchable fluorophores, individual wt CAZ units can be resolved with *d*STORM. However, the CAZ ultrastructure is most accurately resolved by Cy5 (see insets). This is also demonstrated by the localization precision (σ) within the CAZ, which was determined according to Endesfelder et al., 2014. This comparison suggested the use of Cy5 over A532 and A700. Scale bars: 2 μm and 200 nm (inset). From Ehmann et al., 2014.

4.1.2 Density-based analysis of CAZ-units

In order to gain more information on the nanoscopic distribution of Brp within the CAZ, a clustering algorithm was applied that was modified from Bar-On et al., 2012, which takes into account the previously reported diameter of macromolecular CAZ

filaments [~ 10 nm; (Jiao et al., 2010)] analyzed by state-of-the-art electron tomography.

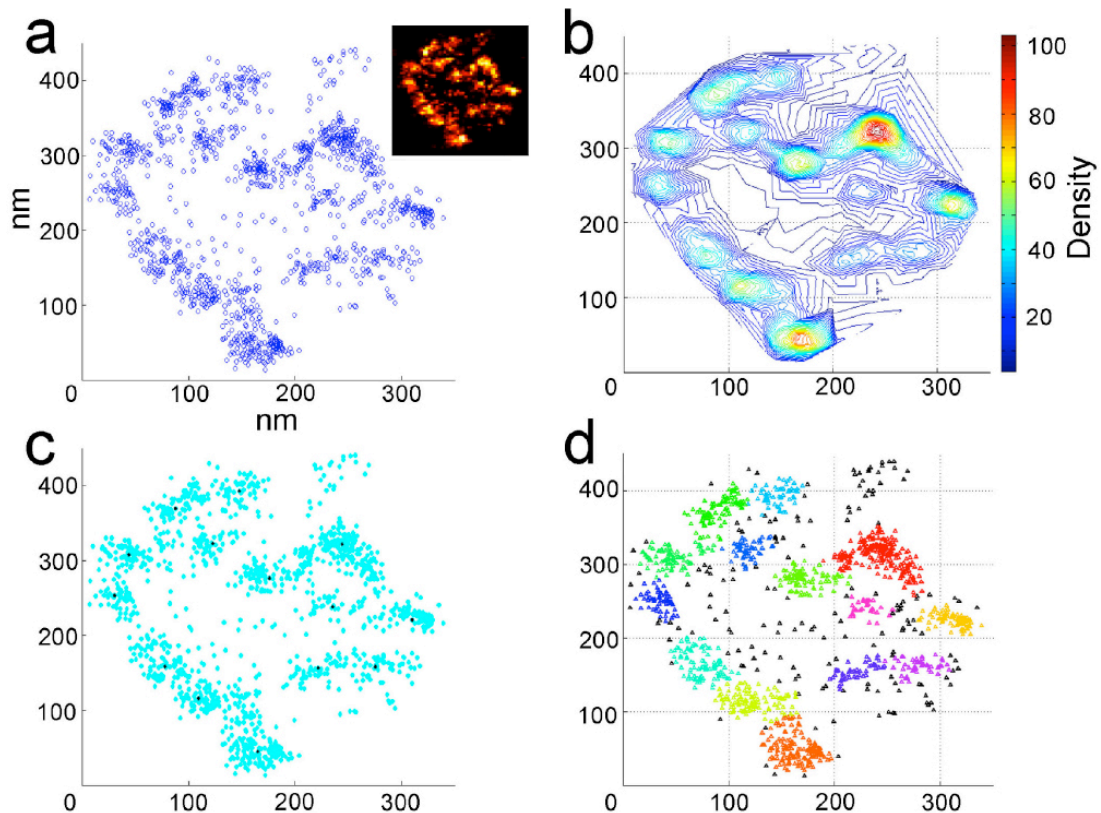


Figure 12 Density-based analysis reveals that CAZ-units are built from multiple Brp clusters. (a) Spatial distribution of localizations in a specific CAZ-unit (shown as inset). (b) Density distribution of localizations in a 20 nm search radius (number of localizations within Eps environment colour coded). Difference between elevation lines, 2 nm. (c) Centres of mass, i.e. local density maxima as discovered by algorithm. (d) Final clusters as defined by algorithm. Each colour represents a different cluster. Parameters used for algorithm: 20 nm search radius (Eps) and 16 neighbours threshold (k). From Ehmann et al., 2014.

Clustering analysis (Figure 12) focused on single, clearly distinguishable CAZ-units (Figure 12a, inset). The density based analysis detected on average 14.5 ± 0.4 multi-protein clusters (SEM) with an elliptic shape (29.8 ± 0.2 nm SEM long radius \times 19.9 ± 0.1 nm SEM short radius) and an average size of 1568 ± 21 nm² (SEM). Taking into account the dimension of the antibody-fluorophore complex and the localization precision (Figure 10a, b), the obtained data closely match the diameter of a CAZ filament. Interestingly, the cluster analysis also revealed that approximately 26% of Brp localizations within the CAZ are not directly grouped into clusters (Figure 12d, black triangles). By comparing this to the imaging background (78 ± 7 localizations per μm^2 SEM) it can be estimated that only 1% of the localizations are caused by unspecific

labelling. Hence, a substantial proportion of Brp molecules is not part of macromolecular filaments.

4.2 Quantifying the substructural organization of Brp in the CAZ

To obtain truly quantitative information on the molecular architecture of AZs, an approach to count Brp molecules in their native surrounding with *d*STORM was developed. Using localization microscopy it is theoretically feasible to extract information on single molecules via the number of localizations obtained in *d*STORM recordings. However, since a primary-secondary antibody approach was chosen, the number of localizations will not directly equal the number of Brp molecules. Therefore, three main questions have to be answered to obtain reliable values for Brp protein copy numbers within the CAZ.

- I. How many localizations are presented by a single Cy5-labelled secondary F(ab')₂ fragment attached to the primary mAb Brp^{Nc82} (Figure 13a, b)?
- II. Are all epitopes saturated by primary mAb Brp^{Nc82} (Figure 13a, c)?
- III. How many secondary antibodies bind to one primary antibody?

Since the number of localizations measured for a fluorophore-labelled antibody is influenced by its nano-environment (Endesfelder et al., 2011; Sauer, 2013), all reference experiments were conducted within the CAZ.

To evaluate the localizations presented by a single Cy5-labelled antibody bound to primary mAb Brp^{Nc82} within the CAZ, titrations of the secondary antibody were performed (Figure 13a, b). To unequivocally identify the CAZ in low concentrations of the secondary Cy5-labelled antibody (2^{ndary} Ab-Cy5), co-staining of mAb Brp^{Nc82} using Alexa-Fluor 488 (A488) was simultaneously accomplished. Additionally, this procedure assures a constant concentration of secondary antibodies (5.2×10^{-8} M; e.g. 1: 100% Cy5 to 0% A488, 10⁻³: 0.1% Cy5 to 99.9% A488). Primary mAb Brp^{Nc82} was kept at a constant concentration (1/2000; experimental concentration). Data were recorded at 7 different dilutions of 2^{ndary} Ab-Cy5 (Figure 13b) and individual super-resolved images

were reconstructed. Localization values within individual CAZs were measured by using the corresponding mAb Brp^{Nc82}-A488 epifluorescence signal as a ‘CAZ-mask’, which was applied to super-resolved Brp^{Nc82}-Cy5 images and allowed localization analysis (Figure 13b). This procedure becomes increasingly important when high dilutions of 2^{ndary} Ab-Cy5 were used. Here, recognition of the CAZ in super-resolved images cannot be accomplished due to strongly decreased Cy5 spot number. The obtained localization values were subsequently histogrammed and fitted to a Poisson model (see chapter 3. Materials and Methods). Applying this method to data obtained from individual dilutions, it was possible to evaluate the average number of localizations per CAZ (L_{CAZ}) as a function of dilution (Figure 13b; Table 1; chapter 3. Materials and Methods). Finally, by fitting a logistic function (Figure 13b; chapter 3. Materials and Methods), the lowest localization value corresponds to a single 2^{ndary} Ab-Cy5 attached to mAb Brp^{Nc82} [$L_2(\text{Cy5})$] and is 16.1 ± 1 SEM (n = 8-10 NMJs per dilution).

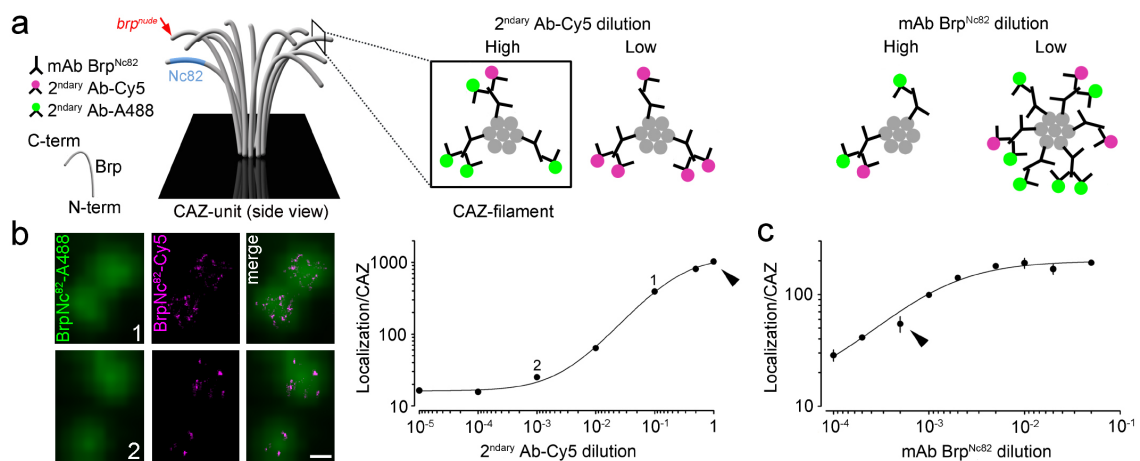


Figure 13 Counting Brp molecules within the CAZ. (a) Schematic of a filamentous CAZ-unit in polarized orientation. Light blue area denotes estimated mAb Brp^{Nc82} epitope, red arrow shows the C-terminal truncation of *brp*^{nude}. Right part of (a) schematically summarizes reference experiments. Individual Brp proteins are indicated by filled circles (grey). (b) Cy5 and A488 labelled 2^{ndary} F(ab')₂ fragments were diluted at a constant overall concentration of 5.2×10^{-8} and a fixed mAb Brp^{Nc82} dilution ($1/2000$; 0.5×10^{-3}) to estimate the number of localizations corresponding to a single Cy5 labelled antibody attached to Brp via mAb Brp^{Nc82}. Binding of single Cy5 antibodies (magenta) to the CAZ was verified through comparison with the A488 epifluorescence signal (green; chapter 3. Materials and Methods). Images depict examples of several antibody dilutions (indicated by 1 and 2 in the graph). (c) Titration of mAb Brp^{Nc82} at fixed Cy5- and A488 antibody concentration (5.2×10^{-8} M; 1% Cy5, 99% A488) provides information on epitope saturation by the primary antibody. Error bars show standard errors of data fits (chapter 3. Materials and Methods). Arrowheads denote antibody concentrations used in experiments (Figures 10, 11, 15 and 20). Scale bar: 200 nm. From Ehmann et al., 2014.

Next it had to be assessed whether all putative Brp epitopes are labelled by mAb Brp^{Nc82} (Figure 13a, c). If naïve epitopes are not completely saturated, localization values would be falsely decreased, thus leading to an underestimation of Brp protein copies within the CAZ. To answer this, titrations of mAb Brp^{Nc82} were performed similar to experiments using 2^{ndary} Ab-Cy5 dilutions before. For this set of experiments, secondary antibody concentration was kept constant and at a fixed ratio of Cy5- and A488-labelled F(ab')₂ fragments (1% to 99%). This ratio was necessary to ensure *d*STORM-compatible imaging settings even at high mAb Brp^{Nc82} concentrations (multiple simultaneous emissions would occur when the Cy5 concentration is too high). Using this approach, it was possible to increase primary mAb Brp^{Nc82} concentration and reconstruct super-resolved images for quantification of localizations until maximal possible epitope saturation could be estimated (Figure 13c). Interestingly, by fitting a logistic function, a value of localizations which corresponds to a saturation of approximately 30% of available Brp epitopes (at the experimental mAb Brp^{Nc82} concentration) was obtained [Figure 13c; Table 1, $L_1(\text{Nc82})$: 198.9 ± 6.4 SEM; $L_{\text{CAZ}}(\text{Nc82 } 1/2000)$: 70.7 ± 7.6 SEM, $n = 4\text{-}5$ NMJs per dilution].

Finally, it had to be clarified how many 2^{ndary} Ab-Cy5 bind to primary mAb Brp^{Nc82}. If the ratio of secondary to primary antibody would be higher than one, the current data obtained through antibody titration experiments would overestimate Brp protein copy number and *vice versa*. To calculate the antibody ratio, a normal concentration of 2^{ndary} Ab-Cy5 (5.2×10^{-8} M) was combined with a low concentration of mAb Brp^{Nc82} (1/20000). For this approach, identification of the CAZ was assured by co-staining using an antibody directed against the N-terminal part of Brp [Brp^{N-term}-A488; (Fouquet et al., 2009)]. In contrast to titration experiments before, where localizations within a whole CAZ were calculated, in this set of experiments solitary Cy5 spots within the CAZ were individually measured. Subsequently, these values were analyzed (see chapter 3. Materials and Methods) to obtain $L_E(\text{Nc82})$: the number of localizations per putative mAb Brp^{Nc82} epitope (Table 1). Comparing this value to $L_2(\text{Cy5})$, the number of localization presented per single 2^{ndary} Ab-Cy5 attached to mAb Brp^{Nc82}, the calculation provided an estimate of 1.59 2^{ndary} Ab-Cy5 per primary mAb Brp^{Nc82} (Table 1).

	$Loc_{CAZ-unit}$	L_2 (Cy5)	L_1 (Cy5)	L_{CAZ} (Cy5 100%)	L_E (Nc82)	L_1 (Nc82)	L_{CAZ} (Nc82 1/2000)
Localizations	1020.5	16.1	1212.2	992.5	25.6	198.9	70.7
SEM	42.7	1.0	117.4	100.9	1.4	6.4	7.6

Table 1 Localization values from antibody titrations. From Ehmann et al., 2014.

Taking these considerations into account allows for quantitative image analysis and provides an estimate of 137 ± 29 SEM Brp molecules per CAZ-unit (see chapter 3. Materials and Methods). Accordingly, approximately 7 Brp molecules are recognized per multiprotein cluster (52.2 ± 0.7 localizations, SEM, $n = 2102$ clusters). Hence, Brp molecules might wrap around each other possibly via their coiled-coil domains to assemble as rod-like heptamers and build up the final 10 nm CAZ-filament. This stoichiometry is quite convincing by comparison with other filamentous protein structures, like subfibrils of intermediate filaments, where seven of them form a filament of ~ 10 nm (Kim and Coulombe, 2007).

4.3 Ultrastructural analysis of different AZ states

The CAZ is subject to activity-dependent structural alterations, which can occur at individual synapses in a highly dynamic manner and are supposed to reflect functional properties of neurotransmission (Atwood and Karunanithi, 2002; Schmid et al., 2008; Matz et al., 2010; Weyhersmüller et al., 2011). However, it is unclear how such structural changes are mechanistically coupled to functional output. A variety of studies previously showed that Brp reorganizations are involved in synaptic plasticity, lasting from milliseconds to days (Schmid et al., 2008; Gilestro et al., 2009; Hallermann et al., 2010c; Weyhersmüller et al., 2011). Theoretically, the reason for such rearrangements could be a change in the number of Brp molecules within the CAZ or their spatial distribution (Graf et al., 2009; Hallermann et al., 2010c).

To test for such underlying mechanisms, two different *Drosophila* mutants, *brp^{nude}* and *rab3^{rup}* (Graf et al., 2009; Hallermann et al., 2010c) were employed. Previous studies have demonstrated that both mutations impact synaptic neurotransmission and exhibit structural changes in Brp organization (Graf et al., 2009; Hallermann et al., 2010c).

Rab3^{rup} is a small vesicle-associated GTPase that regulates and localizes presynaptic components at AZs (Graf et al., 2009). At *rab3^{rup}* mutant NMJs, the number of Brp positive AZs is severely decreased, while remaining AZs exhibit extremely enlarged Brp aggregates [Figure 14; see chapter 2.2.3.1 and 2.2.3.2; (Graf et al., 2009)]. In contrast, *brp^{nude}*, a hypomorphic allele of *brp* that lacks 1% of the entire protein at its C-terminus, displays normal overall CAZ structure (Figure 14), while ultrastructural analyses revealed a strikingly reduced vesicle tethering capacity at T-bars (Hallermann et al., 2010c). Functionally, this results in slowed vesicle recruitment to the AZ and synaptic short-term depression [see chapter 2.2.3.1 and 2.2.3.2; (Hallermann et al., 2010c)]. Employing these two mutants enabled the investigation of different AZ states. Such states are characterized by structural or functional alterations in the precise molecular architecture of AZs and thus shape neurotransmission. Consequently, by using these mutants the CAZ ultrastructure could be assayed quantitatively and combined with functional recordings to test for AZ structure-function relationships.

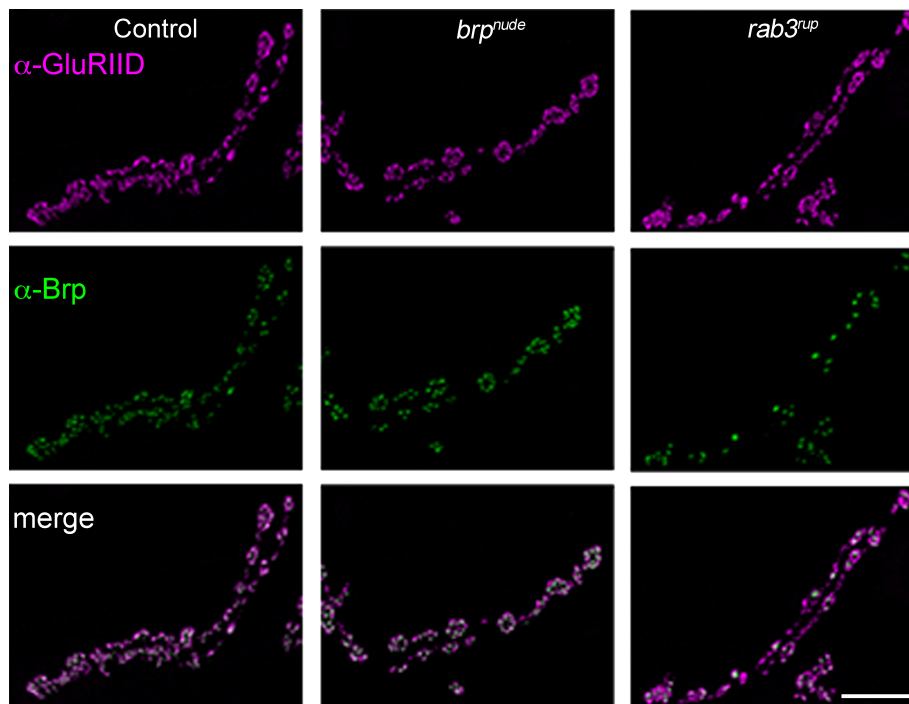


Figure 14 Confocal imaging of *rab3^{rup}* and *brp^{nude}*. Examples displaying GluRIID (glutamate receptor subunit IID, magenta) and Brp (green) immunoreactivities at NMJ sections of control (left panels), *brp^{nude}* (center) and *rab3^{rup}* (right) larvae. Scale bar: 10 μ m.

In agreement with previous work, the application of confocal microscopy to *rab3^{rup}* mutant NMJs showed an accumulation of Brp at a small subset of AZs (Figure 14),

while the overall number of Brp-positive AZs was severely decreased [$\sim 35\%$ of controls; control: 472 ± 43 SEM, $n = 14$ NMJs; *rab3^{rup}*: 164 ± 15 , $n = 14$, $P < 0.001$ vs. control; Figure 15e; (Graf et al., 2009)]. Since the number of GluRIID is unaltered, a large fraction of glutamate receptors does not face Brp-positive AZs (control: 485 ± 49 SEM, $n = 14$ NMJs; *rab3^{rup}*: 354 ± 34 , $n = 14$, rank sum test $P = 0.07$ vs. control). As expected, no change in Brp positive AZs and GluRIID clusters could be observed at *brp^{nude}* mutant NMJs [Brp: *brp^{nude}*: 397 ± 25 , $n = 13$, rank sum test $P = 0.254$ vs. control; Figure 15e; GluRIID: *brp^{nude}*: 447 ± 29 , $n = 13$, rank sum test $P = 0.662$ vs. control; (Hallermann et al., 2010c)].

As a next step, *d*STORM was applied to both mutants in order to study the nanoscopic arrangement of Brp within the CAZ (Figure 15). At *rab3^{rup}* mutant NMJs, the CAZ was significantly enlarged (control: $0.120 \pm 0.006 \mu\text{m}^2$ SEM, $n = 16$ NMJs; *rab3^{rup}*: $0.212 \pm 0.01 \mu\text{m}^2$, $n = 11$, rank sum test $P < 0.001$; Figure 15f) and displayed an increase in Brp localizations (control: 1257 ± 89 localizations SEM, $n = 16$ NMJs; *rab3^{rup}*: 1999 ± 98 , $n = 11$, rank sum test $P < 0.001$; Figure 15f). Additionally, the large *rab3^{rup}* CAZs exhibit a complex structure, often lacking a clearly distinguishable modular composition, which can be seen in controls (Figure 15, enlarged boxed regions). Compared to *rab3^{rup}*, *brp^{nude}* AZs show a more ordered structure, with a modular composition, where CAZ-units can easily be recognized. Moreover, Brp localizations are mostly distributed at the CAZ margin, while they are more uniformly distributed in controls (Figure 15g, enlarged boxed regions, Figure 10). Though *brp^{nude}* AZs show a similar number of Brp localizations (1129 ± 104 localizations SEM, $n = 13$ NMJs, rank sum test $P = 0.28$ vs. control; Figure 15f), they possess a smaller CAZ than controls ($0.097 \pm 0.005 \mu\text{m}^2$ SEM, $n = 13$ NMJs, rank sum test $P = 0.005$ vs. control; Figure 15f). Interestingly, this structural property was not recognized before using STED or EM (Hallermann et al., 2010c).

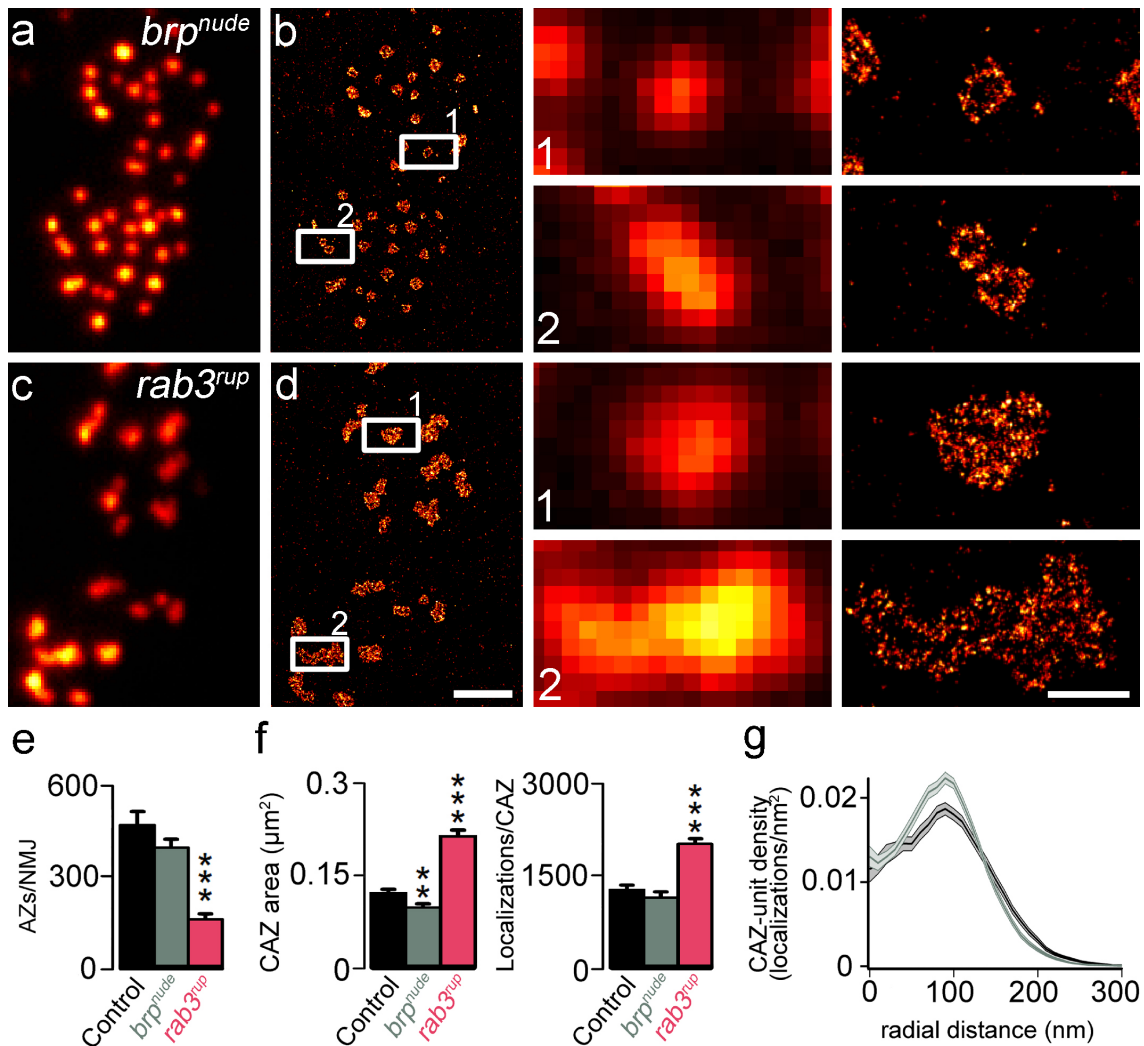


Figure 15 Different nano-organization of Brp within the CAZ. (a,b) Overview of *brp^{nude}* and (c,d) *rab3^{rup}* NMJs stained against Brp. Enlarged boxed regions (left panels epifluorescence, right panels dSTORM) resolve the highly ordered distribution of Brp immunoreactivity in *brp^{nude}*, where Brp localizations are mostly confined to the CAZ margins. In contrast, *rab3^{rup}* CAZs are greatly enlarged and lack a clearly distinguishable modular arrangement. (e-g) Quantification of imaging data acquired with confocal (e) and localization microscopy (f). (g) *En face* views of individual CAZ-units were aligned according to their centres of mass and the radial density distributions of Brp localizations were plotted (dark lines: average, shaded area: SEM). Compared to controls (black), the Brp epitope was distributed more narrowly in *brp^{nude}* (grey) CAZ-units. Scale bars: (a-d) 2 μm , (enlarged boxed regions) 500 nm. From Ehmann et al., 2014.

For a summary of all data obtained with confocal and localization microscopy, please see Table 2. The number of Brp molecules was calculated by application of the conversion factor 0.134 ± 0.028 SEM (chapter 3. Materials and Methods) to corresponding CAZ localizations.

	confocal		<i>d</i> STORM	
	AZ/NMJ	Area (μm^2)	Localizations	Nr of BRP molecules
Control CAZ	472 \pm 43 (n=14 NMJs)	0.120 \pm 0.006 (n=16 NMJs)	1257 \pm 89	168 \pm 34
<i>brp^{nude}</i> CAZ	397 \pm 25 (n=13 NMJs)	0.097 \pm 0.005 (n=13 NMJs)	1129 \pm 104	151 \pm 35
<i>rab3^{rup}</i> CAZ	164 \pm 15 (n=14 NMJs)	0.212 \pm 0.01 (n=12 NMJs)	1999 \pm 98	268 \pm 58

Table 2 Structure of AZs. Confocal microscopy was used to estimate the number of AZs per NMJ (via their Brp-positive CAZ) and super resolution imaging by *d*STORM was engaged to quantify ultrastructural properties of the CAZ. From Ehmann et al., 2014.

4.4 Functional properties of AZ states

4.4.1 Electrophysiological characterization of different AZ states

To obtain mechanistic descriptions of AZ function in both mutants, TEVC recordings were acquired from *Drosophila* larval NMJs. Analysis of minis, spontaneous fusion events of single SVs, showed no differences in *rab3^{rup}* and *brp^{nude}* compared to controls (frequency: control: 2.17 \pm 0.20 Hz SEM, n = 11 NMJs; *brp^{nude}*: 2.28 \pm 0.27 Hz, n = 17, rank sum test P = 0.96 vs. control; *rab3^{rup}*: 1.72 \pm 0.12 Hz, n = 17, rank sum test P = 0.07 vs. control; amplitude: control: - 0.77 \pm 0.04 nA SEM, n = 11 NMJs; *brp^{nude}*: - 0.86 \pm 0.03 nA, n = 17, rank sum test P = 0.20 vs. control; *rab3^{rup}*: - 0.83 \pm 0.02 nA, n = 17, rank sum test P = 0.26 vs. control; Figure 16), indicating no alterations in the response of postsynaptic glutamate receptor fields to neurotransmitter release. Additionally, at low frequency stimulation, evoked at 0.2 Hz, only subtle differences in eEPSC amplitudes could be observed in *rab3^{rup}* mutant larvae (control: - 89.9 \pm 4.8 nA SEM, n = 21 NMJs; *brp^{nude}*: - 87.3 \pm 6.2 nA, n = 26, rank sum test P = 0.45 vs. control; *rab3^{rup}*: - 73.8 \pm 3.3 nA, n = 28, rank sum test P = 0.009 vs. control; Figure 17). Both findings indicate that neither *rap3^{rup}* nor *brp^{nude}* greatly impacts basal synaptic transmission at the NMJ.

As a next step, the impact of both mutations on STP was analyzed. Therefore, paired-pulse recordings and high frequency (60 Hz) stimulation were performed (Figure 18). Both stimulation paradigms evoked pronounced short-term synaptic depression of eEPSC amplitudes in *brp^{nude}* and *rab3^{rup}* (Paired-pulse stimulation: rank sum test vs.

controls: *brp^{nude}* for 10 ms $P = 0.014$, for all other intervals $P \leq 0.01$; *rab3^{rup}* for 10 ms $P = 0.016$, for 30 and 100 ms $P \leq 0.01$; Figure 18a; 60 Hz stimulation: eEPSC 91-100 mean; control: -34.3 ± 1.5 nA SEM, $n = 10$ NMJs; *brp^{nude}*: -23.9 ± 1.3 nA, $n = 10$, rank sum test $P < 0.001$ vs. control; *rab3^{rup}*: -27.3 ± 1.4 nA, $n = 11$, $P = 0.004$ vs. control; Figure 18b).

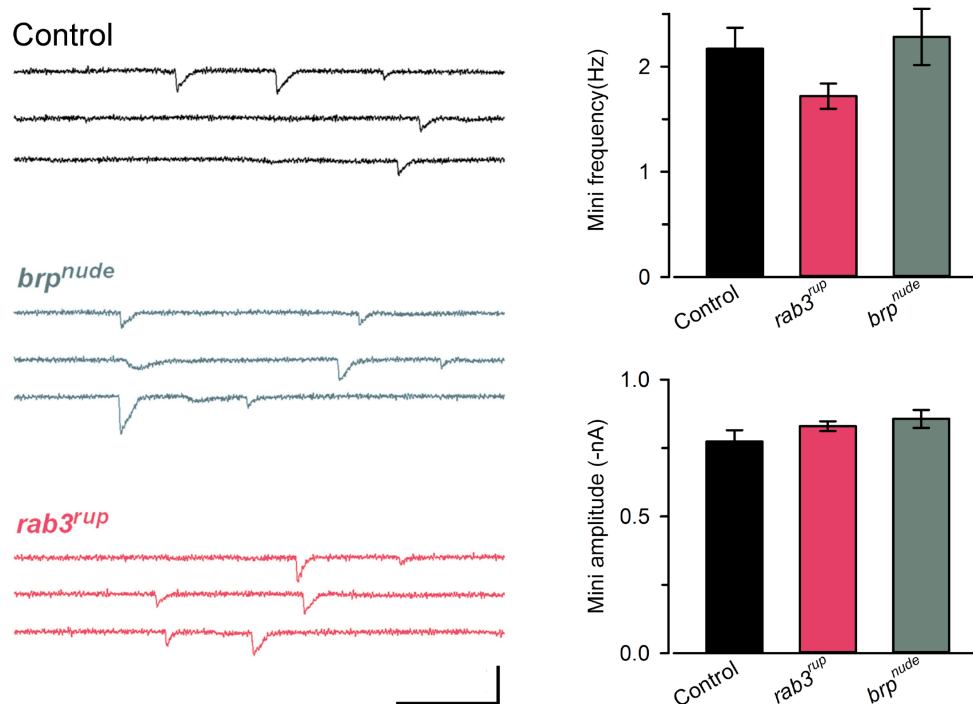


Figure 16 Similar spontaneous transmitter release at larval NMJs. Example traces and quantification of data of mEPSCs. Both mini frequency and amplitude were indistinguishable from controls. Scale bar: 2 nA, 100 ms. From Ehmann et al., 2014.

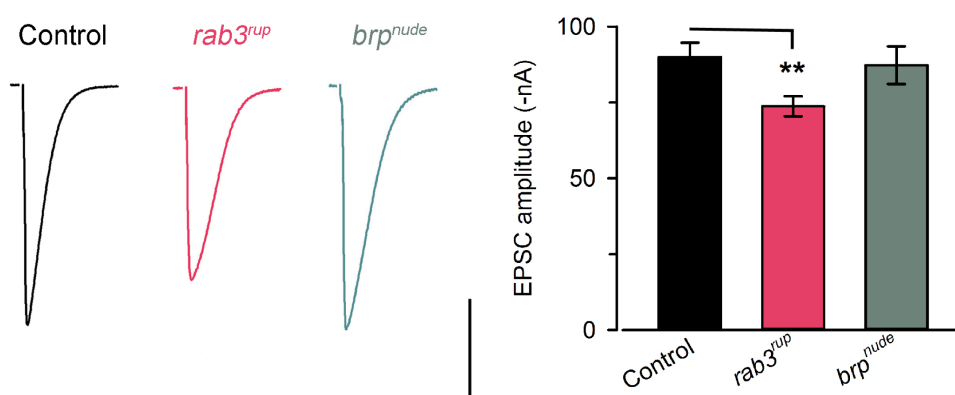


Figure 17 Only subtle differences in evoked release. Average traces and quantification of eEPSC recordings at 0.2 Hz stimulation. The average eEPSC amplitude of *rab3^{rup}* was slightly below control levels. Scale bar: 40 nA, 30 ms. From Ehmann et al., 2014.

Intriguingly, paired-pulse ratios and eEPSC amplitudes during high frequency stimulation were equally reduced in both mutants (Figure 18a), which leads to the question whether synaptic depression might arise from the same origin. To test this, recovery from synaptic depression after a high frequency train of stimuli was investigated with stimuli of increasing interstimulus intervals (Hallermann et al., 2010b, 2010c). While both phases of recovery show a certain Ca^{2+} dependency, previous investigations could nicely show that the first phase additionally relies on fast vesicle supply to the AZ (Hallermann et al., 2010b, 2010c). Whereas *rab3^{rup}* showed normal biphasic recovery, *brp^{nude}* exhibits a slow initial phase of recovery, followed by an unaltered second phase, indicating dissimilar sources of synaptic depression in both mutants (Figure 18b).

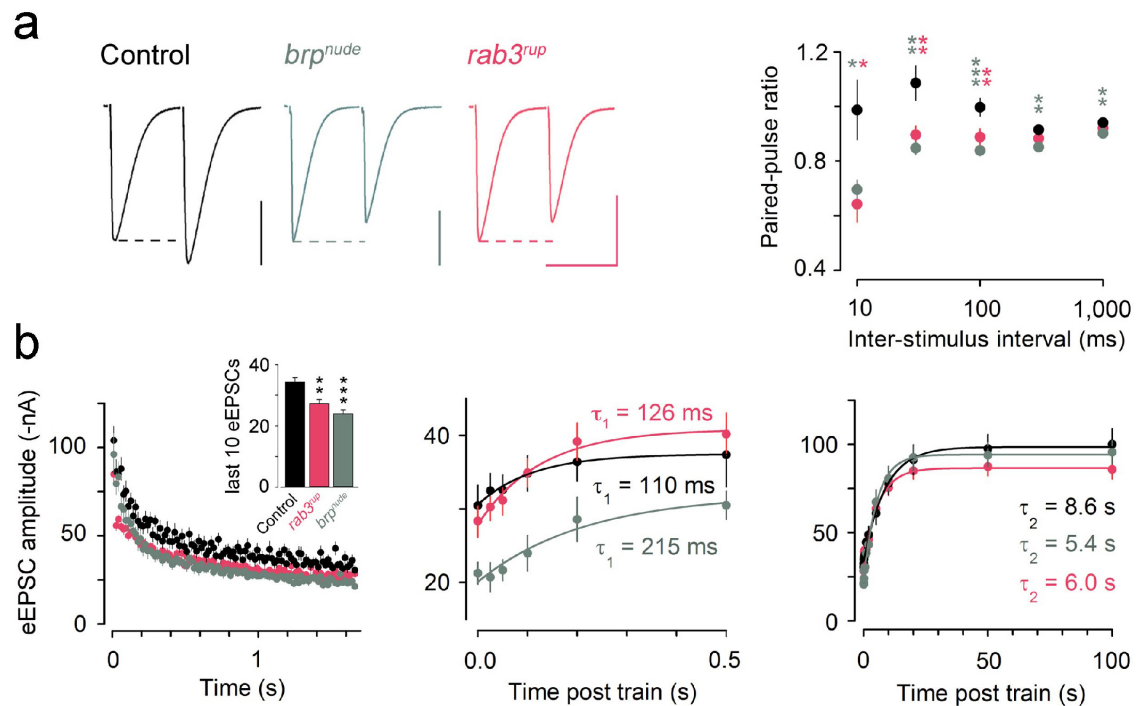


Figure 18 Functional characterization of different AZ states. (a) Example traces (normalized amplitude of the first eEPSC, 30ms interstimulus interval) of paired-pulse recordings at the larval NMJ. Both, paired-pulse recordings and high frequency stimulation at 60 Hz (b) showed similar synaptic depression in both mutants. Whereas recovery in *rab3^{rup}* is unaltered, *brp^{nude}* showed a slowed initial phase of recovery, followed by normal recovery of the slow phase. Scale bar: 30 nA, 30 ms. From Ehmann et al., 2014.

4.4.2 Mechanistic interpretation of AZ function

Alterations in neurotransmission can be described by changes in N , p_{vr} and the rate of vesicle reloading at release sites (k_{+1}). To extract quantitative information on these parameters and thus on the origin of synaptic depression in both mutants, an established modelling approach was applied [see chapter 3. Materials and Methods; (Hallermann et al., 2010b; Weyhermüller et al., 2011)]. In principle, a postsynaptic contribution to synaptic depression is possible, previous studies on both mutants however, allowed to focus on presynaptic parameters. Therefore, two constrained STP models were chosen to simulate high frequency stimulation and the recovery thereof (Figure 19a, modelling parameters: Table 3).

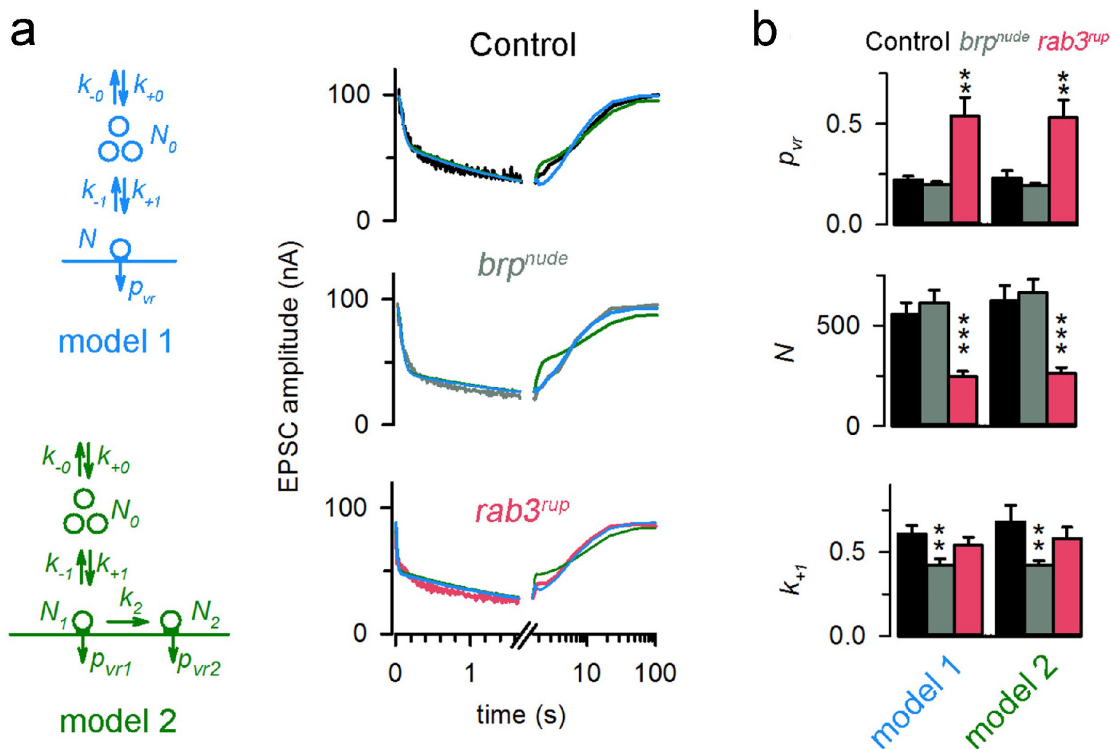


Figure 19 Quantitative description of synaptic depression. (a) Model 1 (blue; encompassing one pool of RRVs refilled from a finite supply pool) and model 2 (green; containing two pools of RRVs with different release probabilities) were used to describe the experimental data (Figure 18; example fits to average data in right panel). (b) By fitting individual trains plus recovery experiments, functional data on neurotransmitter release could be obtained (control: $n = 10$, brp^{nude} : $n = 10$, $rab3^{rup}$: $n = 11$). The results (right panel) can distinguish between brp^{nude} and $rab3^{rup}$ phenotypes. Statistics employed Kruskal-Wallis with Dunn's Multiple Comparison tests. Plots show mean \pm SEM. From Ehmann et al., 2014.

Model 1 comprises one pool of release-ready vesicles (N) with a defined p_{vr} that is refilled from a finite supply pool (N_0) with corresponding refilling rates (k). In contrast,

model 2 incorporates two pools of release-ready vesicles with heterogeneous p_{vr} . $N2$ is a small pool of SVs with a high p_{vr} that is supplied from pool $N1$, which contains more SVs possessing a lower p_{vr} (Figure 19 a; Table 3; chapter 3. Materials and Methods).

For brp^{nude} , both models delineate a regular number of RRVs that possess an average p_{vr} while synaptic depression was brought about by a decreased rate of vesicle replenishment (Figure 19b). These results fit very nicely to a normal electrophysiologically measured RRV pool size, unaltered Ca^{2+} channel clustering but impaired vesicle tethering to AZs (Hallermann et al., 2010c).

In line with previous studies (Graf et al., 2009; Peled and Isacoff, 2011), both STP models assigned synaptic depression at $rab3^{rup}$ NMJs to a decrease in RRVs while the remaining vesicles possess a high p_{vr} (Figure 19b). Given that only a few SVs are available for release, it follows that those get rapidly depleted by stimulus onset, which provokes synaptic depression. Vesicle reloading, however, was not impaired in $rab3^{rup}$.

genotype	N		p_{vr}		k_{+1}	
	model 1	model 2	model 1	model 2	model 1	model 2
Control	555 ± 57	622 ± 76	0.22 ± 0.02	0.23 ± 0.04	0.61 ± 0.05	0.68 ± 0.1
brp^{nude}	612 ± 64	663 ± 68	0.2 ± 0.01	0.19 ± 0.01	0.42 ± 0.04	0.42 ± 0.03
$rab3^{rup}$	246 ± 27	263 ± 30	0.54 ± 0.09	0.53 ± 0.09	0.54 ± 0.05	0.58 ± 0.07

Table 3 Modelling parameters. Data are presented as mean ± SEM. Numbers of individual fitted experiments; control: n = 10; brp^{nude} : n = 10; $rab3^{rup}$: n = 11. Kruskal-Wallis tests with Dunn's Multiple Comparison tests delivered the following levels of significance. From Ehmann et al., 2014:

$N_{model 1}$ P = 0.0002, Control vs. brp^{nude} P > 0.05, Control vs. $rab3^{rup}$ P < 0.001

$N_{model 2}$ P = 0.0001, Control vs. brp^{nude} P > 0.05, Control vs. $rab3^{rup}$ P < 0.001

$p_{model 1}$ P = 0.002, Control vs. brp^{nude} P > 0.05, Control vs. $rab3^{rup}$ P < 0.01

$p_{model 2}$ P = 0.002, Control vs. brp^{nude} P > 0.05, Control vs. $rab3^{rup}$ P < 0.01

$k_{+1, model 1}$ P = 0.005, Control vs. brp^{nude} P < 0.01, Control vs. $rab3^{rup}$ P > 0.05

$k_{+1, model 2}$ P = 0.006, Control vs. brp^{nude} P < 0.01, Control vs. $rab3^{rup}$ P > 0.05

4.5 Dissecting structure-function relationships

Through analysis of *Drosophila* mutants, the presented results provide evidence that quantitative information on the CAZ ultrastructure can be connected to functional properties of neurotransmitter release. These investigations delivered a concept of the relation between Brp structure and function at the AZ. First, the number of release sites scales roughly with the number of AZs per NMJ. Second, variations in release probability correlate with the number of Brp localizations within the CAZ and third, vesicle trafficking speed is reflected by the spatial orientation of Brp within individual CAZ units (Figure 20).

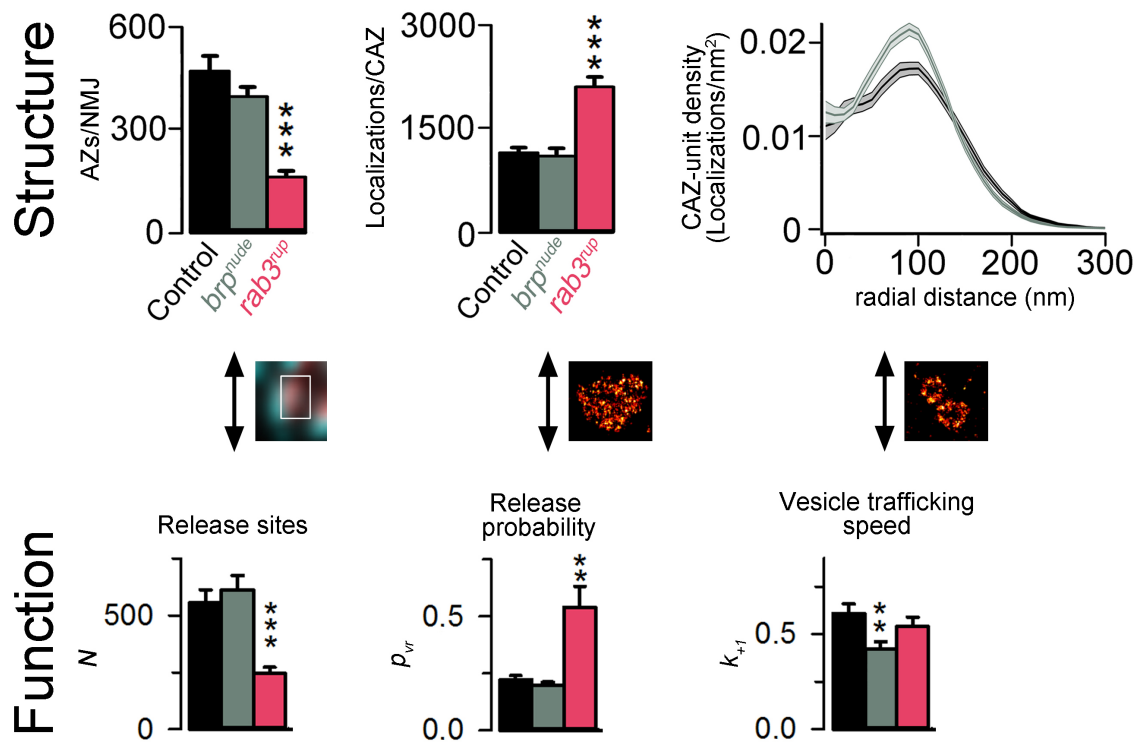


Figure 20 Structure-function relationships at the *Drosophila* AZ. Summary of the results obtained through confocal microscopy and quantitative super-resolution imaging of the CAZ (Figure 15) combined with data from functional analysis of synaptic neurotransmission (Figure 19). Upper panel displays structural features of the CAZ that can be correlated with functional determinants of neurotransmitter release (lower panel) to link AZ structure to function. Middle panel illustrates a wt AZ (boxed region), a *rab3^{rup}* AZ and CAZ-units of *brp^{nude}* (from left to right). From Ehmann et al., 2014.

To further test this interpretation, an intrinsic physiological property of the *Drosophila* NMJ was investigated. Larval muscles are innervated by two glutamatergic motor neurons that form either large (Ib) or small (Is) boutons on the muscle (see chapter

2.2.2). Previous studies already described a functional gradient along Ib boutons, with larger Ca^{2+} signals and correspondingly higher p_{vr} at terminal boutons [Figure 21d; (Guerrero et al., 2005; Peled and Isacoff, 2011)]. Generally, type Ib boutons are relatively large and contain a multitude of AZs (Atwood et al., 1993). Relatedly, a functional gradient in p_{vr} could result from different AZ densities along the axonal branch with an accumulation in terminal boutons. Interestingly, such variations in overall AZ density along the axonal branch have not been detected (Guerrero et al., 2005; Peled and Isacoff, 2011). Hence, a structural match that could describe the gradient in functional properties is still missing.

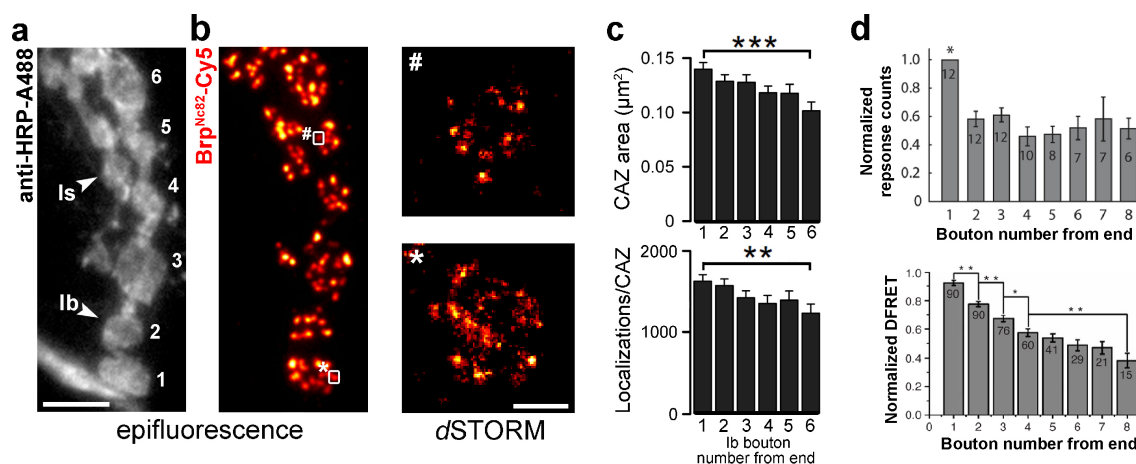


Figure 21 Structural gradient along *Drosophila* Ib motor neurons. (a,b) Epifluorescence images of a Ib motor neuron stained against the neuronal membrane marker HRP (horseradish peroxidase, grey) and anti Brp (red). Staining displays type Ib and type Is motor neurons (arrowheads). Ib boutons are numbered beginning at the distal end (in the lower left corner a neurite passes by the NMJ). (b) The corresponding Brp signal can be clearly allotted to individual boutons (a). Enlarged boxed regions show examples of CAZs imaged with *d*STORM from distal and proximal boutons. (c) Quantification of *d*STORM images reveals larger CAZs and more Brp molecules at terminal boutons that gradually decrease along the Ib motor neuron (Ib bouton number 1 \rightarrow 6 $\hat{=}$ distal \rightarrow proximal boutons). This structural gradient closely matches the functional one (d). Scale bars: (a) 5 μm (b) 200 nm (magnifications). (a-c) From Ehmann et al., 2014. (d) Upper panel from Peled and Isacoff, 2011; Lower panel from Guerrero et al., 2005.

Consequently, *d*STORM was employed to test for different nanoscopic properties of Brp at wt Ib boutons. The results resolve a clear gradient in CAZ area (Ib distal: $0.136 \pm 0.006 \mu\text{m}^2$ SEM, $n = 269$ CAZs; Ib proximal: $0.099 \pm 0.008 \mu\text{m}^2$ SEM, $n = 105$, rank sum test $P < 0.001$) and Brp molecules per CAZ (Ib distal: 1583 ± 77 localizations SEM, $n = 269$ CAZs; Ib proximal: 1200 ± 110 localizations SEM, $n = 105$, rank sum test $P = 0.003$) along the motor neuron (Figure 21). Here, the largest values can be

found in terminal boutons, which reflects a structural correlate that closely matches the functional gradient [Figure 21d; (Guerrero et al., 2005; Peled and Isacoff, 2011)].

For type Is motor neurons no functional gradient has been described. Moreover, it was previously reported that Is boutons possess a higher p_{vr} than their Ib counterparts, whereby this functional property is independent of the number of T-bars per AZ (Atwood et al., 1993; Kurdyak et al., 1994; Feeney et al., 1998). Correspondingly, analysis of the CAZ ultrastructure in Is boutons revealed similar numbers of Brp localizations at Ib and Is boutons (Ib: 1510 ± 93 SEM, $n = 20$ NMJs; Is: 1282 ± 78 , $n = 21$ NMJs, rank sum test $P = 0.074$; Figure 22a), though the CAZ of Is boutons is slightly smaller (Ib: $0.1235 \pm 0.005 \mu\text{m}^2$ SEM, $n = 20$ NMJs, 1255 CAZs; Is: $0.0992 \pm 0.005 \mu\text{m}^2$, $n = 21$ NMJs, 1042 CAZs, rank sum test $P = 0.002$; Figure 21a). A structural gradient along type Is motor neurons was not found (CAZ area: $0.1121 \pm 0.009 \mu\text{m}^2$ SEM (distal), $n = 108$, $0.1141 \pm 0.01 \mu\text{m}^2$ (proximal), $n = 77$, rank sum test $P = 0.575$; Localizations/CAZ: 1380 ± 120 SEM (distal), $n = 108$, 1433 ± 130 (proximal), $n = 77$, rank sum test $P = 0.445$; Figure 22b).

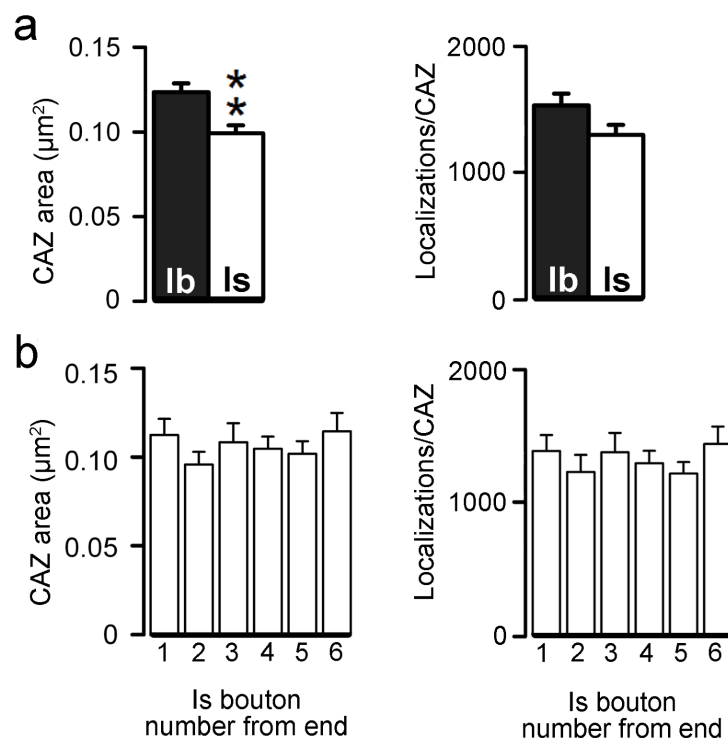


Figure 22 CAZ ultrastructure of type Is boutons. (a) Quantification of *d*STORM data shows that the average CAZ of type Is boutons is slightly smaller compared to Ib CAZs. Both display similar numbers of Brp localizations. In contrast to type Ib CAZs, a structural gradient along the Is motor neuron was not detected (b). From Ehmann et al., 2014.

5. Discussion

5.1 Localization microscopy of the CAZ nanostructure

To the best of my knowledge, the results obtained in this thesis report the first successful application of localization microscopy, namely *d*STORM to *Drosophila* AZs.

In order to assure a high signal to noise ratio, which leads to superior resolution in *d*STORM imaging, primary antibody specificity is enormously important. As can be recognized from density-based cluster analysis, unspecific background labelling was in the range of $\sim 1\%$ taking into account all localizations detected. Additionally, the size of the antibody complex as well as the used fluorophore can critically influence image quality. As resolution increases, the accuracy of localization for a given epitope is limited by the dimension of the antibody bridge (Amiry-Moghaddam and Ottersen, 2013; Sauer, 2013). Commonly used IgGs have a size of $\sim 8\text{-}10$ nm (Weber et al., 1978; Sauer, 2013). Using a primary-secondary antibody system, employing two IgGs will increase the antibody complex to 20 nm, not taking the additional size of the fluorophore into consideration. Hence the large size of the complex can lead to stronger epitope shielding. As a consequence epitope accessibility might be decreased and/or the apparent size of the structure of interest could be enlarged (Sauer, 2013). To reduce dimensions, primary antibodies can be directly labelled, which might cause difficulties in quantifying single molecules or smaller antibodies can be used. In the present work, a secondary F(ab')₂-fragment was used, which decreases the size of the antibody fluorophore complex by $\sim 20\%$ (Amiry-Moghaddam and Ottersen, 2013). Another possibility to reduce antibody dimensions is the application of nanobodies, small camelid antibodies, directed against genetically expressed fluorescent proteins (Ries et al., 2012; Winterflood and Ewers, 2014). Nanobodies are 1.5 x 2.5 nm large and have a molecular mass of 13 kDa (Sauer, 2013). Thus the size of the antibody complex is reduced to about one third (Ries et al., 2012). However, since genetic expression of fluorophore-labelled proteins is necessary, this system is not suitable for detection of endogenous protein levels.

As can be seen in Figure 11, the employment of Cy5 is justified by appreciating the image quality and localization precision obtained with Cy5 in comparison to A700 and A532, which could well be used for 2-channel *d*STORM recordings. One reason for superior resolution could be enhanced fluorescence quantum yield and improved photostability of organic fluorophores, such as Cy5, in addition to its particularly small size [~ 1 nm; (Sauer, 2013)].

The application of *d*STORM to *Drosophila* AZs nicely showed a new level of Brp organization within the CAZ into modules termed CAZ-units (Figure 10d1,d2). Considering their size ($0.095 \pm 0.003 \mu\text{m}^2$ SEM), a CAZ-unit is most likely analogous to a doughnut imaged by STED or a T-bar detected with EM (Atwood et al., 1993; Kittel et al., 2006). An explanation for the modular arrangement of the CAZ, containing several CAZ-units within one AZ, could be provided by keeping in mind that one synapse can harbour more than one T-bar. Interestingly, by dividing the number of localizations per AZ [1257 ± 89 localizations (SEM); Table 2] by the number of localizations per CAZ-unit [1020.5 ± 42.7 localizations (SEM); Table 1], an AZ will comprise on average 1.2 CAZ-units, which fits very well with the number of T-bars per synapse (Atwood et al., 1993; Feeney et al., 1998). At the moment, one can only speculate about the role of these modules for synaptic function but a particularly interesting question is whether this organization is matched by a similar arrangement of glutamate receptor fields at the postsynaptic membrane.

In recent years, SRM has begun to enter the field of neuroscience but it still has to prove itself as a reliable procedure to obtain new cellular insights (Lippincott-Schwartz and Manley, 2009). Therefore analytical tools, which allow quantitative image analysis in order to interpret biological processes must be developed (Bar-On et al., 2012). The implementation of a density-based clustering algorithm provided means to investigate the distribution of Brp within the CAZ and to quantify its supramolecular arrangement (Figure 12). This substantiated the visual interpretation of *d*STORM images and additionally contributed essential information on Brp clusters. Taking into account their structural properties, these clusters most likely match the multiprotein filaments detected with EM (Jiao et al., 2010) and also the ~ 9 ‘dots’ per AZ observed with STED microscopy (Matkovic et al., 2013). Interestingly, a substantial fraction of Brp is not

directly incorporated in clusters but might reside ‘freely’ within the CAZ (Figure 12). This is quite surprising, since at the moment, the biological significance of such ‘free’ Brp molecules is unknown. Using nanoscopy methods, it was previously found that Syntaxin, which is part of the SNARE complex, displays a clustered organization within the plasma membrane (Sieber et al., 2006, 2007). This structural arrangement was refined by the application of *d*STORM that demonstrated three different stages of Syntaxin organization: densely packed into the cluster core (with an even density), with a gradual decrease in density towards the rim of the cluster and as single molecules diffusing outside the clusters (Bar-On et al., 2012). Using modelling, this study suggested a highly reactive state for single Syntaxin molecules while the clustered proteins provide a reserve pool of non-reactive Syntaxin, which could be made ready and released over the clusters periphery (semi-reactive). At the moment, there is no evidence for such a role of ‘free’ Brp molecules. However, it would be extremely interesting to investigate if single molecules get released or incorporated in Brp clusters during synaptic plasticity and if their diffusion at the AZ is restricted by other CAZ constituents as it is the case for Syntaxin (Bar-On et al., 2012).

Another question that derives from the cluster analysis is: Why are Brp clusters elliptical? A possible answer could be provided by the spatial arrangement of fluorophores around Brp filaments. As mAb Brp^{Nc82} will bind around Brp filaments, aligned along the proteins long axis (at the level of mAb Brp^{Nc82} epitope; Figure 13a; Figure 23), the localizations of single fluorophores will be separated by roughly 53 nm [antibody complex (13 nm) + filaments diameter (10 nm) + localization precision (6-7 nm standard deviation, 17 nm FWHM); Figure 23b]. However, since filaments may bend outwards (Jiao et al., 2010; Wichmann and Sigris, 2010), the filaments’ long axis will be perpendicular to the optical axis and the filament diameter of ~ 10 nm will not contribute to the calculation in z. This leads to a decreased projected spacing of localizations along the z-axis of about 43 nm in x and y. This calculation is in good agreement with the results obtained from cluster analysis [60 nm (long axis diameter) × 40 nm (short axis diameter)]. Correspondingly, the widest separation of fluorophores occurs for Cy5 molecules bound to opposite sides of the filament in line with the CAZ-unit circumference, which leads to an elliptic shape of filaments in the analysis.

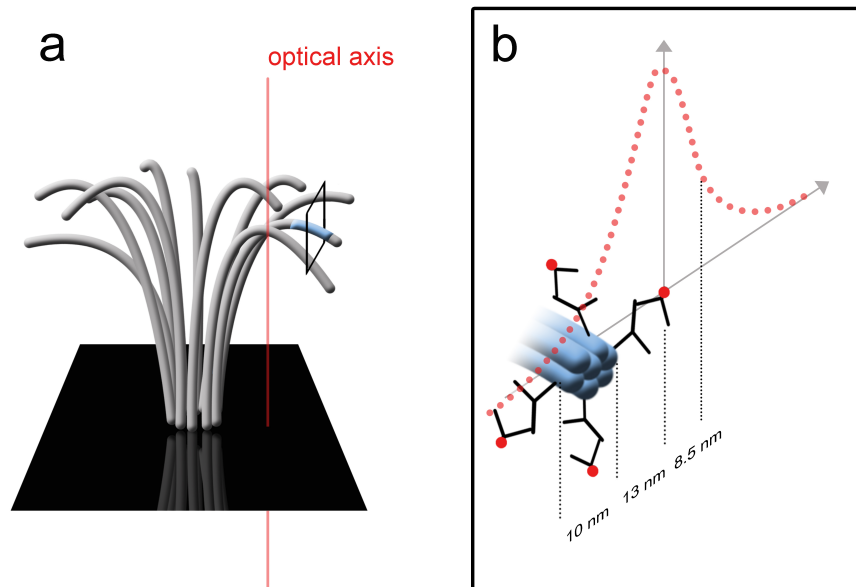


Figure 23 Organization of fluorophores around Brp filaments. (a) Schematics of a CAZ-unit with approximated mAb Brp^{Nc82} epitope in blue. Red line denotes optical axis for a CAZ-unit viewed *en face*. (b) Slice through a single CAZ filament [magnification of boxed region in (a)] at the mAb Brp^{Nc82} binding side illustrates the orientation of antibody complexes [mAb Brp^{Nc82} and Cy5-labelled (red) F(ab')₂ fragment] around Brp epitopes aligned along the proteins long axis. We calculate that 7 Brp molecules contribute to one filament of ~ 10 nm diameter (see chapter 4.2). For clarity only 4 antibody fluorophore complexes are shown. Considering the size of the antibody complex, the filaments' diameter and the localization precision, localizations of single fluorophores are estimated to be separated by 53 nm. As filaments may bend outwards from the CAZ-unit centre, the apparent distance of fluorophores separated in *z* decreases to 43 nm. From Ehmann et al., 2014.

5.2 Quantifying the substructural organization of Brp in the CAZ

Determining the precise number and position of molecules in a biological sample has been described as the ‘holy grail’ of immunocytochemistry (Amiry-Moghaddam and Ottersen, 2013). As already mentioned, the size of the antibody bridge will always influence the precision of localization that can be obtained for a single molecule. Additionally, the use of antibodies themselves demands carefully conducted reference experiments to ensure a robust quantification of imaging data. Localization microscopy with photoactivatable fluorescent proteins might therefore present the method of choice for protein quantification (Betzig et al., 2006; Hess et al., 2006). Here, one can take advantage of specific stoichiometric labelling of the target molecule. This, however, requires genetic expression of a fluorescently tagged protein, which has to be checked carefully for proper function and targeting. Moreover, misfolded and extremely photo-

sensitive proteins, that might bleach before exhibiting sufficient localization for detection, as well as multiple blinking of single fluorescent proteins might complicate the results (Sauer, 2013; Durisic et al., 2014). Recently, Puchner and colleagues published a study on the quantification of molecules in single organelles, in which they corrected for such false positive or false negative errors to extract quantitative information from individual vesicles in the yeast endocytotic pathway (Puchner et al., 2013). This study calibrated for blinking errors by genetically expressing constructs that either contained one, two or three repeats of a photoactivatable fluorescent protein (PAF) in yeast cells. Using this genetic background as a reference, the authors could fit the number of detected PAFs in SRM images to the known number in cells and determined the fraction of non-detected PAFs to be approximately 40% (Puchner et al., 2013).

Another approach to quantify single molecules is stepwise stochastic photobleaching of fluorophores (Sugiyama et al., 2005). Application of this technique, in combination with dynamic and 3D nanoscopy enabled Specht and colleagues to count individual postsynaptic proteins and receptor binding sites (Specht et al., 2013). This method, however, is restricted to sparsely expressed proteins since the likelihood of missed events increases exponentially with the number of molecules (Ulbrich and Isacoff, 2007).

This work focused on the quantification of endogenous proteins in their native environment. Therefore, a standard immunocytochemical approach using primary and dye-labelled secondary antibodies to quantify individual Brp molecules within the CAZ was chosen. As already argued in the results section, several reference experiments had to be conducted to extract reliable data on protein copy numbers (see chapter 4.2). Additionally, uncertainties such as epitope accessibility, antibody affinity and multiple cycles of on/off switching of a single fluorophore have to be taken into account. Brp adopts an elongated polarized orientation at AZs that might naturally help to separate epitopes along the filament circumference thus supporting epitope accessibility (Figure 23). At the moment epitope shielding, which may exist at the level of different AZs and between genotypes cannot be excluded. Additionally, since fixation procedures can lead

to loss of epitopes, which could influence protein numbers, the determined Brp protein copy numbers represent an estimate.

Although specific difficulties in extracting protein numbers remain, an elaborate but in principle secure two-colour method to count single molecules was developed (Figure 13). To demonstrate that such a quantification approach is also possible employing other fluorophores than Cy5, part of the two-colour titration procedure was conducted by using A532 for *d*STORM imaging in combination with A700 to visualize AZs (Figure 24).

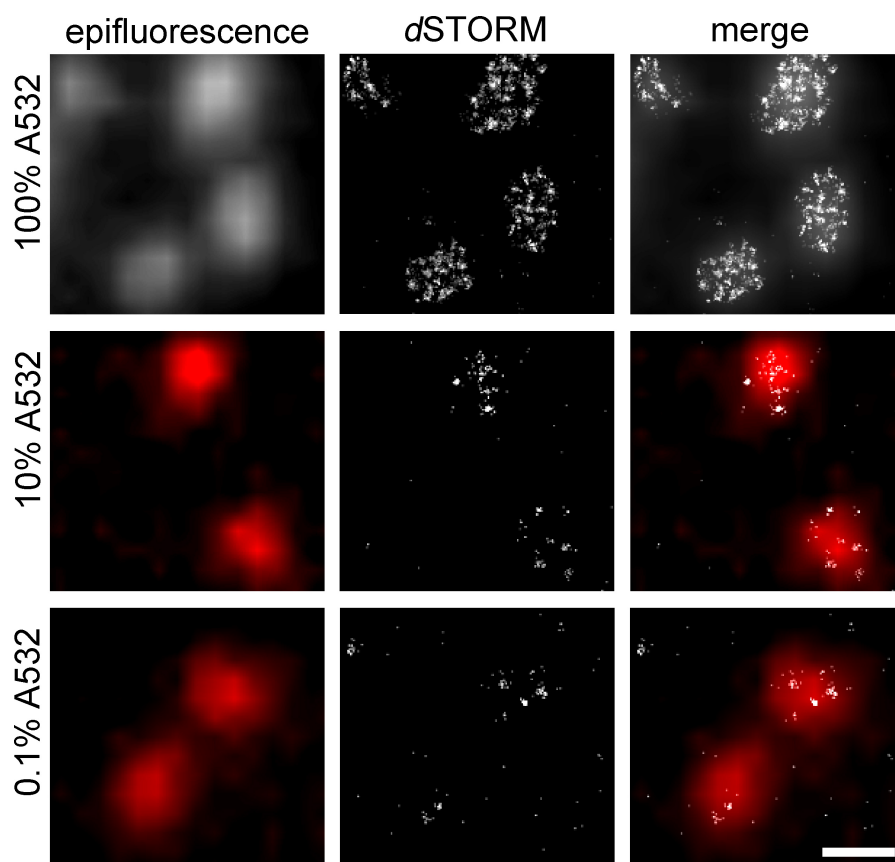


Figure 24 Titration of A532-labelled secondary antibodies. Experiments were conducted using mAb Brp^{Nc82} (1/2000) as primary antibody and specific dilutions of A532-labelled secondary antibody (grey). Co-staining was performed with A700-labelled secondary antibody (red) to assure an overall constant concentration of secondary antibodies (6.25×10^{-9} M). For *d*STORM images a sub-pixel binning of 10 nm / px was applied. Scale bar: 500 nm. From Ehmman et al., 2014.

It has to be kept in mind, that the photoswitching behaviour of fluorophores is sensitive towards changes in the local environment (Endesfelder et al., 2011; Sauer, 2013). Therefore, all antibody titration experiments were conducted and analyzed within the

structure of interest, the CAZ, to stick as tightly as possible to the local protein surrounding. However, certain photophysical effects, like alterations in individual photoswitching characteristics when local fluorophore density is very high (as multiple fluorophores might influence each other's blinking) can never be ruled out and might complicate quantitative super-resolution microscopy.

5.3 Analysis of different AZ states

To investigate different AZ states two already published mutants with known alterations in Brp structure and/or function were employed (Graf et al., 2009; Hallermann et al., 2010c). Using these mutants was necessary, to dissect individual determinants of STP. Taken together, the combined results of *d*STORM imaging, electrophysiological measurements and modelling deliver a comprehensive description of how Brp proteins and their spatial arrangement are connected to synaptic output.

First of all, the data are in line with previous results in that p_{vr} scales with AZ size [Figures 15f, 19b; (Holderith et al., 2012)]. In view of the modelling results, the number of Brp positive AZs per NMJ scales roughly with the number of RRVs (Figures 15e, 19b). Such a calculation predicts on average 3 RRVs per AZ in all three genotypes (wt 2.5, *brp^{nude}* 3.2, *rab3^{rup}* 3.1; chapter 3. Materials and Methods). Hence, in terms of RRVs, the almost twofold larger *rab3^{rup}* CAZ cannot compensate for reduced AZ numbers. Several lines of investigation also stated that larger AZs provide for more RRVs (Miśkiewicz et al., 2011; Weyhersmüller et al., 2011; Holderith et al., 2012; Matkovic et al., 2013). Interestingly, the results obtained from extremely enlarged *rab3^{rup}* CAZs cannot support this finding. A possible solution could be found in the unordered appearance of Brp at *rab3^{rup}* CAZs (Figure 15d, enlarged boxed regions). In *rab3^{rup}* mutants, the number of Brp positive AZs is severely decreased while Brp accumulates at a subset of remaining AZs (Graf et al., 2009). This is accompanied by an increase in fluorescence of cacophony-GFP at Brp positive sites. Therefore, accumulation of Ca²⁺ channels in *rab3^{rup}* might be sufficient for increasing p_{vr} but fails to establish additional release sites. The higher p_{vr} however, cannot compensate for the loss of RRVs during elevated levels of synaptic activity. Additionally, studies at *brp*

null mutant NMJs demonstrated continuous synaptic release, while N appears unchanged (Kittel et al., 2006; Hallermann et al., 2010b). Collectively, results from both mutants point out that Brp itself is most probably not the primary determinant of a release site. Hence, more detailed analysis of wt CAZs and their modular arrangement into CAZ-units, together with super-resolved data on Ca^{2+} channel clustering and vesicle distribution within such units might provide new insights into the structural arrangement of CAZ components, necessary to constitute functional release sites.

In most cases, measuring CAZ area suffices to obtain a basic idea on p_{vr} . However, the results indicate that detailed analysis of Brp protein numbers and their spatial arrangement within the CAZ provides far more information on the ultrastructure that influences synaptic output. This is illustrated at *brp^{nude}* CAZs, which are smaller but contain the same amount of Brp localizations (Figure 15f, Table 2) and elicit an unchanged p_{vr} (Figure 19b). Additionally, Brp molecules are mostly arranged at the rim of the CAZ (Figure 15b, g). Using EM, a nearly opposite phenotype was recently reported in a study that employed an acetylation defective mutant to investigate structural and functional consequences on Brp. This mutation leads to spreading out of Brp filaments, resulting in larger T-bars that can tether more SVs, a larger RRP and enhanced synaptic transmission (Miśkiewicz et al., 2011). In contrast, the smaller *brp^{nude}* CAZ is accompanied by deficient vesicle tethering and slowed vesicle recruitment, resulting in short-term synaptic depression (Figures 18 and 19). Therefore, vesicle tethering might influence the spatial arrangement of CAZ filaments. It is quite conceivable that binding of SVs can lead to a distortion of Brp filaments, resulting in a more unorganized state of the CAZ since not every filament might attach to a SV at the same time. Conversely, it is also possible that the precise arrangement of Brp filaments within the CAZ might influence its vesicle tethering capacity. While at present it cannot be differentiated between these mechanisms, it is clear that the spatial organization of Brp provides information on vesicle reloading kinetics.

Finally, the present work highlights how fundamentally different AZ states can give rise to similar facets of short-term depression (Figure 18). To explain synaptic function, the degree of paired-pulse depression is commonly associated with the extent of p_{vr} . However, the results together with studies that reported fast vesicle reloading

(Hallermann et al., 2010a), transient fusion (Zhang et al., 2007) and release site clearance (Neher, 2010b) show that interpretation of functional data is a delicate issue. Here, the detailed analysis of the CAZ ultrastructure could contribute to test alternative interpretations of synaptic depression.

5.4 Dissecting structure-function relationships

Making use of the high resolution provided by *d*STORM a structural gradient along *Drosophila* Ib motor neurons could be found (Figure 22). This feature has not been seen before (Peled and Isacoff, 2011), most probably due to the diffraction-limited resolution of light microscopy. However, preceding studies already found a functional gradient along this glutamatergic neuron by employing genetically expressed Ca^{2+} sensors (Guerrero et al., 2005; Peled and Isacoff, 2011). This study reported on low- and high-probability release sites that can be directly located next to each other within the same bouton, while the largest fraction of high-probability release sites was found in boutons at the end of the axon (Peled and Isacoff, 2011). These results are in good agreement with a previously reported heterogeneity of synaptic strength along Ib motor neurons using presynaptic Ca^{2+} imaging (Guerrero et al., 2005). The results presented in this thesis constitute a mechanistic basis for the reported functional diversification of AZs (Guerrero et al., 2005; Peled and Isacoff, 2011).

In the case of Is boutons, a functional gradient was not described yet and we did not find any structural gradient along the Is motor neuron. Recently, this result was corroborated by a study that employed electrophysiology in combination with confocal and super-resolution microscopy to show that Brp and Synaptotagmin functionally interact to spatially differentiate AZs (Paul et al., 2015). It was previously reported that AZs of Is neurons possess a higher p_{vr} than their Ib counterparts, which is not accompanied by an increased number of T-bars per AZ (Atwood et al., 1993; Kurdyak et al., 1994; Feeney et al., 1998). Similarly, in comparison to type Ib synapses, we found normal numbers of Brp localization at Is CAZs, though the CAZ was slightly smaller (Figure 22). Here, p_{vr} does not seem to scale directly with CAZ size or Brp localization. Intriguingly, Is boutons possess larger SVs than Ib boutons (Karunanithi et

al., 2002). Using electrophysiology in combination with EM, Karunanithi and co-worker could show a linear relationship between vesicle diameter and quantal size, in which larger vesicles can release more neurotransmitter to maximize their influence on neurotransmission (Karunanithi et al., 2002). Furthermore, theoretical studies on Ca^{2+} dynamics indicate that larger vesicles get released with a higher probability, due to a greater accumulation of Ca^{2+} under their surface (Glavinović and Rabie, 2001). Such large vesicles might present a diffusion barrier for free Ca^{2+} and alter its spatial profiles during fast Ca^{2+} influx. Moreover, they are supposed to bind more fixed Ca^{2+} buffers at the plasma membrane, which could act as ‘memory elements’ to further enhance p_{vr} during stimulation (Glavinović and Rabie, 2001). This, together with the present results obtained for Is boutons, emphasizes again that Brp is not the sole determinant of p_{vr} and motivates detailed ultrastructural analysis of other AZ components.

6. Conclusion & Outlook

The precise description of synaptic function demands a clear understanding of the nanoscopic organization of proteins within AZs that influences neurotransmission. Biochemical and functional studies have already delivered a wealth of valuable information on the molecular composition of AZs and its impact on synaptic output. However, without direct ultrastructural access to this nanodomain, knowledge about molecular structure-function relationships remains incomplete.

Several SRM techniques are already available that yield the capacity to localize proteins on the nanometer scale and resolve components of macromolecular arrangements in their native environment. Here, localization microscopy might capture an outstanding position since it can provide truly quantitative information on single molecules (Specht et al., 2013; Ehmann et al., 2014). In the end, however, combined approaches will help to deliver a clear structural and functional understanding of AZs.

Correlative approaches such as combining SRM with biochemistry (Wilhelm et al., 2014), EM (Watanabe et al., 2011) and array tomography (Nanguneri et al., 2012) present auspicious perspectives for elucidating the nanostructure of AZs. Yet, as resolution increases and quantitative information becomes increasingly important in the neurosciences, sophisticated analyses are required to interpret the depth of data obtained by SRM (Bar-On et al., 2012). Additionally, valuable knowledge on AZ structure-function relationships could be gained by spatially resolving dynamic information. This approach, however, demands technical developments to increase image acquisition speed in order to monitor molecular dynamics with both: high temporal and spatial resolution.

A particular exciting question that might be answered by correlative approaches is the spatial arrangement of Ca^{2+} channels at the AZ (Figure 25). Ca^{2+} channels have a fundamental impact on neurotransmission by governing excitation-secretion coupling. While electrophysiological studies in combination with Ca^{2+} imaging, Ca^{2+} uncaging and modelling have already delivered predictions of Ca^{2+} channel numbers and their arrangement (Stanley, 1993; Meinrenken et al., 2002; Schneggenburger and Neher,

2005; Sheng et al., 2012), direct information on their nanoscopic positioning is still rare (Haydon et al., 1994; Feeney et al., 1998; Holderith et al., 2012; Indriati et al., 2013).

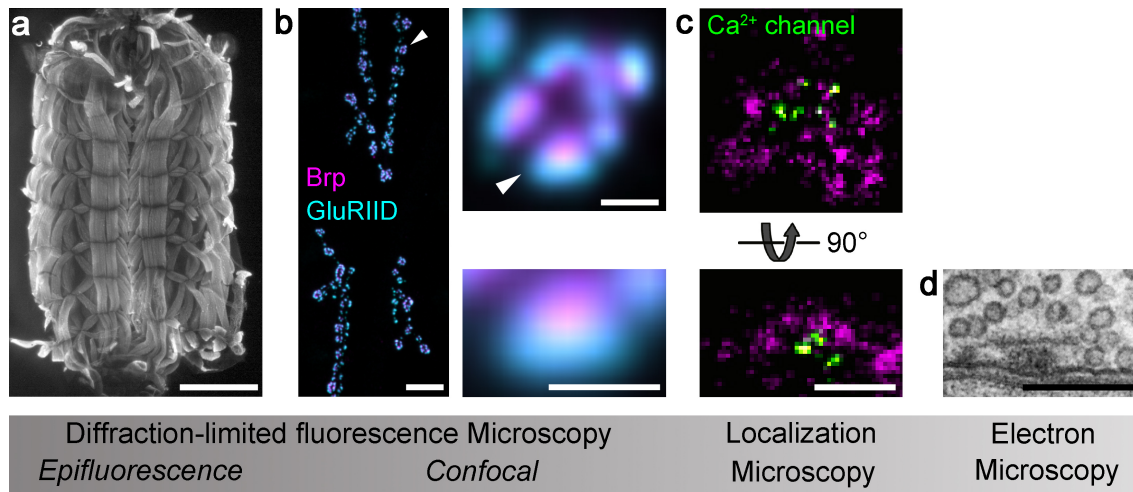


Figure 25 Microscopy of *Drosophila* AZs. Gradual increase in resolution is shown from left to right. (a) shows a *Drosophila* nerve muscle preparation (stained with Phalloidin, a marker against F-Actin) imaged with epifluorescence microscopy. (b) depicts a neuromuscular junction [left panel; stained with mAb Brp^{Nc82} (magenta) and against postsynaptic GluRIID (cyan)], a single bouton (upper panel) and a synapse [(lower panel); arrowheads indicate enlarged regions]. (c) dSTORM image of an AZ stained with mAb Brp^{Nc82} (magenta) and against Ca²⁺ channels [(green); nanobody recognizes a GFP-tagged $\alpha 1$ -subunit of the cacophony Ca²⁺ channel; (Kawasaki et al., 2004)], viewed *en face* (optical axis perpendicular to AZ membrane, upper panel) and from the side (optical axis parallel to AZ membrane, lower panel; cf. d). (d) displays an electron micrograph of the AZ with electron dense pre- and postsynaptic membranes as well as the T-bar that stretches out into the cytoplasm. Electron micrograph kindly provided by C. Wichmann and S.J. Sigrist. Scale bars: (a) 1 mm; (b) 10 μ m (NMJ), 1 μ m (bouton), 500 nm (synapse); (c, d) 200 nm. From Ehmann et al., 2015.

In the context of this thesis, it would be highly interesting to quantify the number and precise arrangement of Ca²⁺ channels at the *Drosophila* NMJ especially at *rab3^{rup}* AZs that contain more Brp localizations but fail to establish more release sites. This might be due to a disordered localization of Ca²⁺ channels. Additionally, *rab3^{rup}* mutants exhibit an extremely enlarged CAZ and lack the modular composition that can be found in controls. Here, the number and nanoscopic arrangement of Ca²⁺ channels in relation to Brp could contribute to our understanding of how these modules are built and what their physiological meaning could be.

A further promising alternative for correlative studies is the combined application of SRM and optogenetics. The term optogenetics derives from the use of ‘light-responsive proteins’ (opto-) that are genetically expressed [-genetic; (Miesenböck, 2009)].

Although a variety of such light-sensitive proteins exist (Grote et al., 2014), the discovery of Channelrhodopsin-1 [ChR1; (Nagel et al., 2002)] and in particular Channelrhodopsin-2 [ChR2; (Nagel et al., 2003)], as light-sensitive cation channels, provided means to examine neural circuits using light (Deisseroth, 2011). At present, ChRs are used in a multitude of laboratories (Grote et al., 2014) to trace functional connections, to study the mechanisms of activity regulation in circuits or to examine the neural basis of behaviour (Miesenböck, 2009).

Recently, we exploited the excellent genetic accessibility of the *Drosophila* NMJ to induce activity-dependent synaptic plasticity via ChR2 in defined synaptic compartments (Figure 26). This work aimed to get a better mechanistic understanding of the coupling between synaptic activity and synapse development. Interestingly, we could reveal that postsynaptic changes in GluR subunit composition follow a Hebbian rule of plasticity (Ljaschenko et al., 2013).

At the *Drosophila* NMJ, GluRs can be categorized as non-NMDA-type and assemble as heterotetramers that contain GluR-IIC/III, IID and IIE subunits while GluRIIA and GluRIIB can be exchanged (Marrus et al., 2004; Featherstone et al., 2005; Qin et al., 2005). Incorporation of GluRIIA or GluRIIB subunits results in different physiological properties of the receptor field (DiAntonio et al., 1999; Qin et al., 2005; Schmid et al., 2006, 2008; Ljaschenko et al., 2013). *In vivo* imaging has delivered substantial information on the maturation of the *Drosophila* NMJ (Rasse et al., 2005; Schmid et al., 2008) and on the incorporation of specific GluR subunits into receptor fields during synapse development (Schmid et al., 2008). Beginning with the incorporation of GluRIIA subunits at immature synapses, maturation of the opposed presynaptic AZ leads to GluRIIB subunit integration until an even ratio is reached at mature synapses (Schmid et al., 2008). Additionally, differential subunit expression results in a specific spatial pattern of receptor fields in that GluRIIA containing receptors are more frequently located opposite of low p_{vr} sites (Marrus and DiAntonio, 2004; Schmid et al., 2008).

Building upon this understanding, we expressed ChR2 presynaptically ('pre'), postsynaptically ('post') or in both compartments ('pre & post'; Figure 26) and analyzed GluRIIA subunit distributions following different light-stimulation paradigms.

In summary, we found that correlated pre- and postsynaptic activity led to synapse specific incorporation of GluRIIA subunits into receptor fields while presynaptic stimulation in the absence of postsynaptic depolarization provoked GluRIIA removal. These findings led to a physiological model that links development to activity-dependent Hebbian synaptic plasticity at the *Drosophila* NMJ (Ljaschenko et al., 2013).

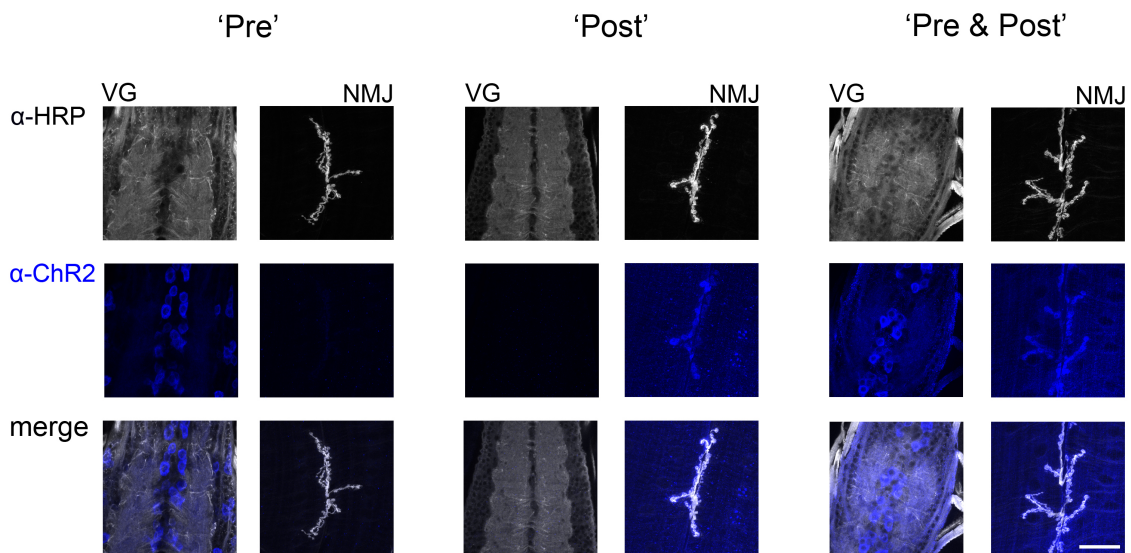


Figure 26 ChR2 expression in individual synaptic compartments. Antibody staining against neuronal membranes (α -HRP; grey) and ChR2 (α -ChR2; blue) in different genetic situations. 'Pre' (presynaptically expressed in motor neurons; *ok6-gal4*>>*UAS-chop2*), 'Post' (postsynaptically expressed in muscles; *g7-gal4*>>*UAS-chop2*) and 'Pre & Post' (expressed in both synaptic compartments). When ChR2 is expressed in postsynaptic compartments, a strong signal can be detected in muscles, possibly owing to the large membrane surface of the SSR. Example images of NMJs are maximum projections. For VG (ventral ganglion) only 3 optical slices were projected. Scale bar: 30 μ m. From Ljaschenko et al., 2013.

Although physiological consequences of alterations in GluR composition have already been successfully studied, information on the precise ultrastructural arrangement of postsynaptic glutamatergic receptor fields is still missing. In *Drosophila* specifically tagged GluR subunits are available that were shown to preserve full physiological functionality (Rasse et al., 2005; Schmid et al., 2008). Exploiting such transgenic strategies, SRM of postsynaptic receptor fields and quantification of their GluR content is possible. Here, antibody titration approaches like the one presented in this thesis might contribute to shed light on the number and nanoscopic distribution of GluRs within individual fields *in situ*. Such analyses will help to clarify if postsynaptic receptor fields follow a similar modular arrangement like their presynaptic counterparts (Figure 10). If so, are two adjacent units equipped with the same GluR composition or

are they regulated at a sub-synaptic level? This information can be linked with functional data obtained by electrophysiological recordings to correlate structural with functional estimations of GluR number per synapse.

Despite its benefits, the application of ChR2 for behavioural studies in adult *Drosophila* has been restrained by high light intensities that are necessary to permeate the pigmented cuticle and activate channels. Therefore, we collaborated with Georg Nagel, University of Würzburg, to introduce a new ChR2 variant, termed ChR2-XXL (eXtra high eXpression and Long open state) to *Drosophila*. In contrast to other ChR variants, this mutant does not require additional retinal food supplementation, which is likely due to its higher affinity for endogenous retinal. We demonstrated improved localization (Figure 27), an extraordinary long open state-state lifetime and the largest currents of all published ChR variants so far (Dawydow et al., 2014).

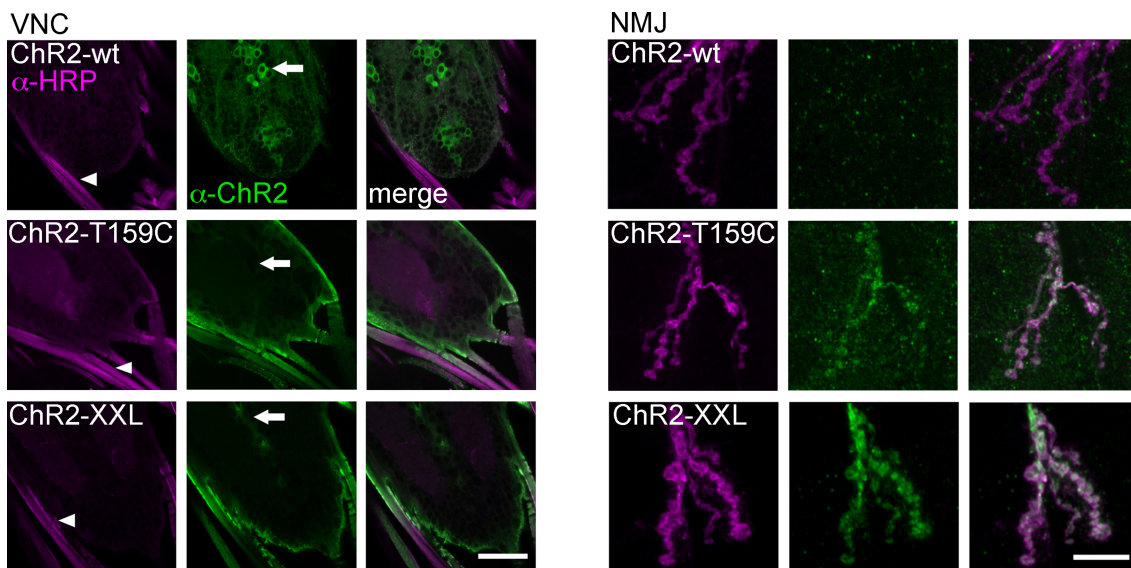


Figure 27 ChR2 localization patterns. Antibody staining against ChR2 (α -ChR2, green) and neuronal membranes (α -HRP, magenta) in different ChR2 mutants, all driven with *ok6-gal4*. In the VNC (ventral nerve cord; left panel) ChR2-wt was restricted to motor neuron cell bodies (arrow), while ChR-T159C and ChR2-XXL showed expression in motor neuron axons, leaving the VNC (arrowheads). At the NMJ, ChR2-XXL as well as ChR2-T159C are present while ChR2-wt could not be detected. For example images of VNCs only 3 images were maximum projected. NMJs are maximum projected, except ChR2-T159C were only one optical slice is shown. Scale bars: 30 μ m (VNC), 10 μ m (NMJ). From Dawydow et al., 2014.

In addition, we introduced a different ChR2 variant [ChR2-T159C; (Berndt et al., 2011)] to flies that exhibits similar advantageous features albeit to a lesser extent. The high light sensitivity of both ChR2 variants was tested in 3 different behavioural

paradigms using adult *Drosophila*: monosynaptic proboscis extension reflex, polysynaptic courtship behaviour and associative learning, in collaboration with André Fiala, University of Göttingen. Predictably, ChR2-T159C required more light compared to ChR2-XXL, where even low light intensities ($\sim 1 \mu\text{W}/\text{mm}^2$) were sufficient to write associative olfactory memories. Therefore, we expect that especially ChR2-XXL will be of great interest to applications where sufficient light delivery but not temporal precision presents the limiting factor (Dawydow et al., 2014). The development of such powerful optogenetic tools constitutes an ideal entry point to study complex physiological processes in adult *Drosophila*. In order to interrogate if mechanisms like learning and memory are associated with structural alterations in specific CAZ components, such a project could exploit precise cell-specific targeting of recently introduced ChR-variants to the presumed site of learning and memory, the mushroom body (Heisenberg, 2003). Thus, non-invasive activity-dependent manipulation of mushroom body neurons in adult *Drosophila* is applicable. By employing this in order to write memories through light using different learning paradigms, the combination with SRM techniques will provide an extraordinary opportunity to clarify if memory traces can be found in the precise architecture of the AZ.

7. References

- Abbe E (1873) Beiträge zur Theorie des Mikroskops und der mikroskopischen Wahrnehmung. Arch für Mikroskopische Anat 9:456–468.
- Abbott LF, Nelson SB (2000) Synaptic plasticity: taming the beast. Nat Neurosci 3 Suppl:1178–1183.
- Adler EM, Augustine GJ, Duffy SN, Charlton MP (1991) Alien intracellular calcium chelators attenuate neurotransmitter release at the squid giant synapse. J Neurosci 11:1496–1507.
- Alabi AA, Tsien RW (2012) Synaptic vesicle pools and dynamics. Cold Spring Harb Perspect Biol 4:a013680.
- Amiry-Moghaddam M, Ottersen OP (2013) Immunogold cytochemistry in neuroscience. Nat Neurosci 16:798–804.
- Anderson M, Halpern M, Keshishian H (1988) Identification of the neuropeptide transmitter proctolin in *Drosophila* larvae: characterization of muscle fiber-specific neuromuscular endings. J Neurosci 8:242–255.
- Atluri PP, Regehr WG (1996) Determinants of the time course of facilitation at the granule cell to Purkinje cell synapse. J Neurosci 16:5661–5671.
- Atwood HL, Govind CK, Wu CF (1993) Differential ultrastructure of synaptic terminals on ventral longitudinal abdominal muscles in *Drosophila* larvae. J Neurobiol 24:1008–1024.
- Atwood HL, Karunanithi S (2002) Diversification of synaptic strength: presynaptic elements. Nat Rev Neurosci 3:497–516.
- Auger C, Kondo S, Marty A (1998) Multivesicular release at single functional synaptic sites in cerebellar stellate and basket cells. J Neurosci 18:4532–4547.
- Augustin I, Rosenmund C, Südhof TC, Brose N (1999) Munc13-1 is essential for fusion competence of glutamatergic synaptic vesicles. Nature 400:457–461.
- Axelrod D (2003) Total internal reflection fluorescence microscopy in cell biology. Methods Enzymol 361:1–33.
- Bar-On D, Wolter S, van de Linde S, Heilemann M, Nudelman G, Nachliel E, Gutman M, Sauer M, Ashery U (2012) Super-resolution imaging reveals the internal architecture of nano-sized syntaxin clusters. J Biol Chem 287:27158–27167.
- Barrionuevo G, Schottler F, Lynch G (1980) The effects of repetitive low frequency stimulation on control and “potentiated” synaptic responses in the hippocampus. Life Sci 27:2385–2391.
- Bear MF (1999) Homosynaptic long-term depression: a mechanism for memory? Proc Natl Acad Sci U S A 96:9457–9458.
- Bellen HJ, Levis RW, Liao G, He Y, Carlson JW, Tsang G, Evans-Holm M, Hiesinger PR, Schulze KL, Rubin GM, Hoskins RA, Spradling AC (2004) The BDGP gene disruption project: single transposon insertions associated with 40% of *Drosophila* genes. Genetics 167:761–781.
- Bellen HJ, Tong C, Tsuda H (2010) 100 years of *Drosophila* research and its impact on vertebrate neuroscience: a history lesson for the future. Nat Rev Neurosci 11:514–522.

- Berndt A, Schoenenberger P, Mattis J, Tye KM, Deisseroth K, Hegemann P, Oertner TG (2011) High-efficiency channelrhodopsins for fast neuronal stimulation at low light levels. *Proc Natl Acad Sci U S A* 108:7595–7600.
- Betz A, Thakur P, Junge HJ, Ashery U, Rhee JS, Scheuss V, Rosenmund C, Rettig J, Brose N (2001) Functional interaction of the active zone proteins Munc13-1 and RIM1 in synaptic vesicle priming. *Neuron* 30:183–196.
- Betzig E, Patterson GH, Sougrat R, Lindwasser OW, Olenych S, Bonifacino JS, Davidson MW, Lippincott-Schwartz J, Hess HF (2006) Imaging intracellular fluorescent proteins at nanometer resolution. *Science* 313:1642–1645.
- Blatow M, Caputi A, Burnashev N, Monyer H, Rozov A (2003) Ca^{2+} buffer saturation underlies paired pulse facilitation in calbindin-D28k-containing terminals. *Neuron* 38:79–88.
- Bliss TVP, Lomo T (1973) Long-lasting potentiation of synaptic transmission in the dentate area of the anaesthetized rabbit following stimulation of the perforant path. *J Physiol* 232:331–356.
- Bliss TV, Collingridge GL (1993) A synaptic model of memory: long-term potentiation in the hippocampus. *Nature* 361:31–39.
- Bloom FE, Aghajanian GK (1968) Fine structural and cytochemical analysis of the staining of synaptic junctions with phosphotungstic acid. *J Ultrastruct Res* 22:361–375.
- Bollmann JH, Sakmann B, Borst JG (2000) Calcium sensitivity of glutamate release in a calyx-type terminal. *Science* 289:953–957.
- Borst JG, Sakmann B (1996) Calcium influx and transmitter release in a fast CNS synapse. *Nature* 383:431–434.
- Branco T, Staras K (2009) The probability of neurotransmitter release: variability and feedback control at single synapses. *Nat Rev Neurosci* 10:373–383.
- Brand AH, Perrimon N (1993) Targeted gene expression as a means of altering cell fates and generating dominant phenotypes. *Development* 118:401–415.
- Brose N, Hofmann K, Hata Y, Südhof TC (1995) Mammalian homologues of *Caenorhabditis elegans* unc-13 gene define novel family of C2-domain proteins. *J Biol Chem* 270:25273–25280.
- Budnik V, Ruiz-Canada C (2006) *The Fly Neuromuscular Junction: Structure and Function: Second Edition*. Elsevier.
- Burnashev N, Rozov A (2005) Presynaptic Ca^{2+} dynamics, Ca^{2+} buffers and synaptic efficacy. *Cell Calcium* 37:489–495.
- Castillo PE, Schoch S, Schmitz F, Südhof TC, Malenka RC (2002) RIM1 α is required for presynaptic long-term potentiation. *Nature* 415:327–330.
- Choquet D, Triller A (2013) The dynamic synapse. *Neuron* 80:691–703.
- Citri A, Malenka RC (2008) Synaptic plasticity: multiple forms, functions, and mechanisms. *Neuropsychopharmacology* 33:18–41.
- Clements JD, Silver RA (2000) Unveiling synaptic plasticity: a new graphical and analytical approach. *Trends Neurosci* 23:105–113.
- Conchello J-A, Lichtman JW (2005) Optical sectioning microscopy. *Nat Methods* 2:920–931.
- Couteaux R, Pécot-Dechavassine M (1970) Synaptic vesicles and pouches at the level of “active zones” of the neuromuscular junction. *Acad Sci Hebd Seances Acad Sci D* 271:2346–2349.

- Dani A, Huang B, Bergan J, Dulac C, Zhuang X (2010) Superresolution Imaging of Chemical Synapses in the Brain. *Neuron* 68:843–856.
- Dawydow A, Gueta R, Ljaschenko D, Ullrich S, Hermann M, Ehmann N, Gao S, Fiala A, Langenhan T, Nagel G, Kittel RJ (2014) Channelrhodopsin-2-XXL, a powerful optogenetic tool for low-light applications. *Proc Natl Acad Sci*:2–7.
- Deisseroth K (2011) Optogenetics. *Nat Methods* 8:26–29.
- Deken SL, Vincent R, Hadwiger G, Liu Q, Wang Z-W, Nonet ML (2005) Redundant localization mechanisms of RIM and ELKS in *Caenorhabditis elegans*. *J Neurosci* 25:5975–5983.
- Del Castillo J, Katz B (1954) Quantal components of the end-plate potential. *J Physiol* 124:560–573.
- Dellinger B, Felling R, Ordway RW (2000) Genetic Modifiers of the *Drosophila* NSF Mutant, comatose, Include a Temperature-Sensitive Paralytic Allele of the Calcium Channel α 1-Subunit Gene, cacophony. *Genetics* 155:203–211.
- Deng L, Kaeser PS, Xu W, Südhof TC (2011) RIM proteins activate vesicle priming by reversing autoinhibitory homodimerization of Munc13. *Neuron* 69:317–331.
- DiAntonio A, Petersen SA, Heckmann M, Goodman CS (1999) Glutamate receptor expression regulates quantal size and quantal content at the *Drosophila* neuromuscular junction. *J Neurosci* 19:3023–3032.
- DiAntonio A, Burgess RW, Chin AC, Deitcher DL, Scheller RH, Schwarz TL (1993) Identification and characterization of *Drosophila* genes for synaptic vesicle proteins. *J Neurosci* 13:4924–4935.
- Dietzl G, Chen D, Schnorrer F, Su K-C, Barinova Y, Fellner M, Gasser B, Kinsey K, Oppel S, Scheiblaue S, Couto A, Marra V, Keleman K, Dickson BJ (2007) A genome-wide transgenic RNAi library for conditional gene inactivation in *Drosophila*. *Nature* 448:151–156.
- Dobrunz LE, Stevens CF (1997) Heterogeneity of release probability, facilitation, and depletion at central synapses. *Neuron* 18:995–1008.
- Dulubova I, Khvotchev M, Liu S, Huryeva I, Südhof TC, Rizo J (2007) Munc18-1 binds directly to the neuronal SNARE complex. *Proc Natl Acad Sci U S A* 104:2697–2702.
- Durisc N, Laparra-Cuervo L, Sandoval-Álvarez A, Borbely JS, Lakadamyali M (2014) Single-molecule evaluation of fluorescent protein photoactivation efficiency using an *in vivo* nanotemplate. *Nat Methods* 11:156–162.
- E.B. Lewis, Bacher F (1968) Methods of feeding ethyl methane sulfonate (EMS) to *Drosophila* males. *Dros Inf Serv* 43:193.
- Eggermann E, Bucurenciu I, Goswami SP, Jonas P (2012) Nanodomain coupling between Ca^{2+} channels and sensors of exocytosis at fast mammalian synapses. *Nat Rev Neurosci* 13:7–21.
- Egner A, Hell SW (2005) Fluorescence microscopy with super-resolved optical sections. *Trends Cell Biol* 15:207–215.
- Ehmann N, Sauer M, Kittel RJ, Ehmann N, Sauer M, Kittel RJ (2015) Super-resolution microscopy of the synaptic active zone. *Front. Cell. Neurosci.* 9:7.
- Ehmann N, van de Linde S, Alon A, Ljaschenko D, Keung XZ, Holm T, Rings A, DiAntonio A, Hallermann S, Ashery U, Heckmann M, Sauer M, Kittel RJ (2014) Quantitative super-resolution imaging of Bruchpilot distinguishes active zone states. *Nat Commun* 5:1–12.

- Endesfelder U, Malkusch S, Flottmann B, Mondry J, Liguzinski P, Verveer PJ, Heilemann M (2011) Chemically induced photoswitching of fluorescent probes-A general concept for super-resolution microscopy. *Molecules* 16:3106–3118.
- Endesfelder U, Malkusch S, Fricke F, Heilemann M (2014) A simple method to estimate the average localization precision of a single-molecule localization microscopy experiment. *Histochem Cell Biol* 141:629–638.
- Ester M, Kriegel H, Sander J, Xu X (1996) A density-based algorithm for discovering clusters in large spatial databases with noise. *KDD-96 Proc.*
- Fatt P, Katz B (1952) Spontaneous subthreshold activity at motor nerve endings. *J Physiol* 117:109–128.
- Featherstone DE, Rushton E, Rohrbough J, Liebl F, Karr J, Sheng Q, Rodesch CK, Broadie K (2005) An essential *Drosophila* glutamate receptor subunit that functions in both central neuropil and neuromuscular junction. *J Neurosci* 25:3199–3208.
- Fedchyshyn MJ, Wang L-Y (2005) Developmental transformation of the release modality at the calyx of Held synapse. *J Neurosci* 25:4131–4140.
- Feeney CJ, Karunanithi S, Pearce J, Govind CK, Atwood HL (1998) Motor nerve terminals on abdominal muscles in larval flesh flies, *Sarcophaga bullata*: comparisons with *Drosophila*. *J Comp Neurol* 402:197–209.
- Felmy F, Neher E, Schneggenburger R (2003) Probing the intracellular calcium sensitivity of transmitter release during synaptic facilitation. *Neuron* 37:801–811.
- Fenster SD, Chung WJ, Zhai R, Cases-Langhoff C, Voss B, Garner AM, Kaempf U, Kindler S, Gundelfinger ED, Garner CC (2000) Piccolo, a presynaptic zinc finger protein structurally related to bassoon. *Neuron* 25:203–214.
- Fernández-Busnadiego R, Asano S, Oprisoreanu A-M, Sakata E, Doengi M, Kochovski Z, Zürner M, Stein V, Schoch S, Baumeister W, Lucić V (2013) Cryo-electron tomography reveals a critical role of RIM1 α in synaptic vesicle tethering. *J Cell Biol* 201:725–740.
- Fouquet W, Oswald D, Wichmann C, Mertel S, Depner H, Dyba M, Hallermann S, Kittel RJ, Eimer S, Sigrist SJ (2009) Maturation of active zone assembly by *Drosophila* Bruchpilot. *J Cell Biol* 186:129–145.
- Frank CA, Wang X, Collins CA, Rodal AA, Yuan Q, Verstreken P, Dickman DK (2013) New approaches for studying synaptic development, function, and plasticity using *Drosophila* as a model system. *J Neurosci* 33:17560–17568.
- Galbraith CG, Galbraith J a (2011) Super-resolution microscopy at a glance. *J Cell Sci* 124:1607–1611.
- Garini Y, Vermolen BJ, Young IT (2005) From micro to nano: recent advances in high-resolution microscopy. *Curr Opin Biotechnol* 16:3–12.
- Geiger JRP, Jonas P (2000) Dynamic Control of Presynaptic Ca²⁺ Inflow by Fast-Inactivating K⁺ Channels in Hippocampal Mossy Fiber Boutons. *Neuron* 28:927–939.
- Geppert M, Goda Y, Hammer RE, Li C, Rosahl TW, Stevens CF, Südhof TC (1994) Synaptotagmin I: a major Ca²⁺ sensor for transmitter release at a central synapse. *Cell* 79:717–727.
- Gilestro GF, Tononi G, Cirelli C (2009) Widespread changes in synaptic markers as a function of sleep and wakefulness in *Drosophila*. *Science* 324:109–112.

- Glavinović MI, Rabie HR (2001) Monte Carlo evaluation of quantal analysis in the light of Ca^{2+} dynamics and the geometry of secretion. *Pflügers Arch Eur J Physiol* 443:132–145.
- Gracheva EO, Hadwiger G, Nonet ML, Richmond JE (2008) Direct interactions between *C. elegans* RAB-3 and Rim provide a mechanism to target vesicles to the presynaptic density. *Neurosci Lett* 444:137–142.
- Graf ER, Daniels RW, Burgess RW, Schwarz TL, DiAntonio A (2009) Rab3 dynamically controls protein composition at active zones. *Neuron* 64:663–677.
- Graf ER, Valakh V, Wright CM, Wu C, Liu Z, Zhang YQ, DiAntonio A (2012) RIM Promotes Calcium Channel Accumulation at Active Zones of the *Drosophila* Neuromuscular Junction. *J Neurosci* 32:16586–16596.
- Grote M, Engelhard M, Hegemann P (2014) Of ion pumps, sensors and channels - perspectives on microbial rhodopsins between science and history. *Biochim Biophys Acta* 1837:533–545.
- Guerrero G, Reiff DF, Rieff DF, Agarwal G, Ball RW, Borst A, Goodman CS, Isacoff EY (2005) Heterogeneity in synaptic transmission along a *Drosophila* larval motor axon. *Nat Neurosci* 8:1188–1196.
- Gundelfinger ED, Fejtova A (2012) Molecular organization and plasticity of the cytomatrix at the active zone. *Curr Opin Neurobiol* 22:423–430.
- Gustafsson MGL (2000) Surpassing the lateral resolution limit by a factor of two using structured illumination microscopy. *J Microsc* 198:82–87.
- Gustafsson MGL (2005) Nonlinear structured-illumination microscopy: wide-field fluorescence imaging with theoretically unlimited resolution. *Proc Natl Acad Sci U S A* 102:13081–13086.
- Hallermann S, Fejtova A, Schmidt H, Weyhersmüller A, Silver RA, Gundelfinger ED, Eilers J (2010a) Bassoon speeds vesicle reloading at a central excitatory synapse. *Neuron* 68:710–723.
- Hallermann S, Heckmann M, Kittel RJ (2010b) Mechanisms of short-term plasticity at neuromuscular active zones of *Drosophila*. *HFSP J* 4:72–84.
- Hallermann S, Kittel RJ, Wichmann C, Weyhersmüller A, Fouquet W, Mertel S, Oswald D, Eimer S, Depner H, Schwärzel M, Sigrist SJ, Heckmann M (2010c) Naked dense bodies provoke depression. *J Neurosci* 30:14340–14345.
- Han Y, Kaeser PS, Südhof TC, Schneggenburger R (2011) RIM determines Ca^{2+} channel density and vesicle docking at the presynaptic active zone. *Neuron* 69:304–316.
- Harlow ML, Ress D, Stoschek A, Marshall RM, McMahan UJ (2001) The architecture of active zone material at the frog's neuromuscular junction. *Nature* 409:479–484.
- Haydon PG, Henderson E, Stanley EF (1994) Localization of individual calcium channels at the release face of a presynaptic nerve terminal. *Neuron* 13:1275–1280.
- Hebb DO (1949) *The organization of behavior: A neuropsychological Theory*. John Wiley.
- Heilemann M, van de Linde S, Schüttpelz M, Kasper R, Seefeldt B, Mukherjee A, Tinnefeld P, Sauer M (2008) Subdiffraction-resolution fluorescence imaging with conventional fluorescent probes. *Angew Chem Int Ed Engl* 47:6172–6176.
- Heintzmann R, Cremer C (1999) Laterally Modulated Excitation Microscopy: Improvement of resolution by using a diffraction grating. *Proc SPIE* 3568:185–196.

- Heisenberg M (2003) Mushroom body memoir: from maps to models. *Nat Rev Neurosci* 4:266–275.
- Hell S (2009) primer: fluorescence imaging under the diffraction limit. *Nat Methods* 6:19.
- Hell SW (2007) Far-field optical nanoscopy. *Science* 316:1153–1158.
- Hell SW, Wichmann J (1994) Breaking the diffraction resolution limit by stimulated emission: stimulated-emission-depletion fluorescence microscopy. *Opt Lett* 19:780.
- Hess ST, Girirajan TPK, Mason MD (2006) Ultra-high resolution imaging by fluorescence photoactivation localization microscopy. *Biophys J* 91:4258–4272.
- Heuser JE, Reese TS (1973) Evidence for recycling of synaptic vesicle membrane during transmitter release at the frog neuromuscular junction. *J Cell Biol* 57:315–344.
- Hibino H, Pironkova R, Onwumere O, Vologodskaja M, Hudspeth AJ, Lesage F (2002) RIM Binding Proteins (RBPs) Couple Rab3-Interacting Molecules (RIMs) to Voltage-Gated Ca^{2+} Channels. *Neuron* 34:411–423.
- Hofbauer A, Ebel T, Waltenspiel B, Oswald P, Chen Y, Halder P, Biskup S, Lewandrowski U, Winkler C, Sickmann A, Buchner S, Buchner E (2009) The Wuerzburg hybridoma library against *Drosophila* brain. *J Neurogenet* 23:78–91.
- Holderith N, Lorincz A, Katona G, Rózsa B, Kulik A, Watanabe M, Nusser Z (2012) Release probability of hippocampal glutamatergic terminals scales with the size of the active zone. *Nat Neurosci* 15:988–997.
- Hosoi N, Sakaba T, Neher E (2007) Quantitative analysis of calcium-dependent vesicle recruitment and its functional role at the calyx of Held synapse. *J Neurosci* 27:14286–14298.
- Imig C, Min S-W, Krinner S, Arancillo M, Rosenmund C, Südhof TC, Rhee J, Brose N, Cooper BH (2014) The Morphological and Molecular Nature of Synaptic Vesicle Priming at Presynaptic Active Zones. *Neuron* 84:416–431.
- Indriati DW, Kamasawa N, Matsui K, Meredith AL, Watanabe M, Shigemoto R (2013) Quantitative localization of Cav_{2.1} (P/Q-type) voltage-dependent calcium channels in Purkinje cells: somatodendritic gradient and distinct somatic coclustering with calcium-activated potassium channels. *J Neurosci* 33:3668–3678.
- Jahn R, Fasshauer D (2012) Molecular machines governing exocytosis of synaptic vesicles. *Nature* 490:201–207.
- Jan LY, Jan YN (1976a) Properties of the larval neuromuscular junction in *Drosophila melanogaster*. *J Physiol* 262:189–214.
- Jan LY, Jan YN (1976b) L-glutamate as an excitatory transmitter at the *Drosophila* larval neuromuscular junction. *J Physiol* 262:215–236.
- Jia XX, Gorczyca M, Budnik V (1993) Ultrastructure of neuromuscular junctions in *Drosophila*: comparison of wild type and mutants with increased excitability. *J Neurobiol* 24:1025–1044.
- Jiao W, Masich S, Franzén O, Shupliakov O (2010) Two pools of vesicles associated with the presynaptic cytosolic projection in *Drosophila* neuromuscular junctions. *J Struct Biol* 172:389–394.
- Johnston PA, Archer BT, Robinson K, Mignery GA, Jahn R, Südhof TC (1991) rab3A attachment to the synaptic vesicle membrane mediated by a conserved polyisoprenylated carboxy-terminal sequence. *Neuron* 7:101–109.

- Jones S a, Shim S-H, He J, Zhuang X (2011) Fast, three-dimensional super-resolution imaging of live cells. *Nat Methods* 8:499–508.
- Kaesler PS, Deng L, Wang Y, Dulubova I, Liu X, Rizo J, Südhof TC (2011) RIM proteins tether Ca^{2+} channels to presynaptic active zones via a direct PDZ-domain interaction. *Cell* 144:282–295.
- Kandel ER (1976) *Cellular basis of behavior: An introduction to behavioral neurobiology*. W.H. Freeman, San Fransisco.
- Kandel ER (2001) The molecular biology of memory storage: a dialogue between genes and synapses. *Science* 294:1030–1038.
- Karunanithi S, Marin L, Wong K, Atwood HL (2002) Quantal size and variation determined by vesicle size in normal and mutant *Drosophila* glutamatergic synapses. *J Neurosci* 22:10267–10276.
- Katz B, Miledi R (1968) The role of calcium in neuromuscular facilitation. *J Physiol* 195:481–492.
- Kaufmann N, DeProto J, Ranjan R, Wan H, Van Vactor D (2002) *Drosophila* Liprin- α and the Receptor Phosphatase Dlar Control Synapse Morphogenesis. *Neuron* 34:27–38.
- Kawasaki F, Collins SC, Ordway RW (2002) Synaptic Calcium-Channel Function in *Drosophila*: Analysis and Transformation Rescue of Temperature-Sensitive Paralytic and Lethal Mutations of Cacophony. *J Neurosci* 22:5856–5864.
- Kawasaki F, Felling R, Ordway RW (2000) A temperature-sensitive paralytic mutant defines a primary synaptic calcium channel in *Drosophila*. *J Neurosci* 20:4885–4889.
- Kawasaki F, Zou B, Xu X, Ordway RW (2004) Active zone localization of presynaptic calcium channels encoded by the cacophony locus of *Drosophila*. *J Neurosci* 24:282–285.
- Kempf C, Staudt T, Bingen P, Horstmann H, Engelhardt J, Hell SW, Kuner T (2013) Tissue multicolor STED nanoscopy of presynaptic proteins in the calyx of held. *PLoS One* 8:e62893.
- Keshishian H, Chiba A, Chang TN, Halfon MS, Harkins EW, Jarecki J, Wang L, Anderson M, Cash S, Halpern ME (1993) Cellular mechanisms governing synaptic development in *Drosophila melanogaster*. *J Neurobiol* 24:757–787.
- Kim S, Coulombe PA (2007) Intermediate filament scaffolds fulfill mechanical, organizational, and signaling functions in the cytoplasm. *Genes Dev* 21:1581–1597.
- Kittel RJ, Wichmann C, Rasse TM, Fouquet W, Schmidt M, Schmid A, Wagh D a, Pawlu C, Kellner RR, Willig KI, Hell SW, Buchner E, Heckmann M, Sigrist SJ (2006) Bruchpilot promotes active zone assembly, Ca^{2+} channel clustering, and vesicle release. *Science* 312:1051–1054.
- Klingauf J, Neher E (1997) Modeling buffered Ca^{2+} diffusion near the membrane: implications for secretion in neuroendocrine cells. *Biophys J* 72:674–690.
- Knapek S, Sigrist S, Tanimoto H (2011) Bruchpilot, a synaptic active zone protein for anesthesia-resistant memory. *J Neurosci* 31:3453–3458.
- Kurdyak P, Atwood HL, Stewart BA, Wu CF (1994) Differential physiology and morphology of motor axons to ventral longitudinal muscles in larval *Drosophila*. *J Comp Neurol* 350:463–472.

- Kuromi H, Honda A, Kidokoro Y (2004) Ca^{2+} influx through distinct routes controls exocytosis and endocytosis at *Drosophila* presynaptic terminals. *Neuron* 41:101–111.
- Lai S-L, Lee T (2006) Genetic mosaic with dual binary transcriptional systems in *Drosophila*. *Nat Neurosci* 9:703–709.
- Landis DM, Hall AK, Weinstein LA, Reese TS (1988) The organization of cytoplasm at the presynaptic active zone of a central nervous system synapse. *Neuron* 1:201–209.
- Lee JS, Ho W-K, Lee S-H (2012) Actin-dependent rapid recruitment of reluctant synaptic vesicles into a fast-releasing vesicle pool. *Proc Natl Acad Sci U S A* 109:E765–E774.
- Lee JS, Ho W-K, Neher E, Lee S-H (2013) Superpriming of synaptic vesicles after their recruitment to the readily releasable pool. *Proc Natl Acad Sci U S A* 110:15079–15084.
- Lenzi D, von Gersdorff H (2001) Structure suggests function: the case for synaptic ribbons as exocytotic nanomachines. *Bioessays* 23:831–840.
- Leung BO, Chou KC (2011) Review of super-resolution fluorescence microscopy for biology. *Appl Spectrosc* 65:967–980.
- Lewis A, Taha H, Strinkovski A, Manevitch A, Khatchaturiants A, Dekhter R, Ammann E (2003) Near-field optics: from subwavelength illumination to nanometric shadowing. *Nat Biotechnol* 21:1378–1386.
- Lichtman JW, Conchello J-A (2005) Fluorescence microscopy. *Nat Methods* 2:910–919.
- Limbach C, Laue MM, Wang X, Hu B, Thiede N, Hultqvist G, Kilimann MW (2011) Molecular in situ topology of Aczonin/Piccolo and associated proteins at the mammalian neurotransmitter release site. *Proc Natl Acad Sci U S A* 108:E392–E401.
- Lippincott-Schwartz J, Manley S (2009) Putting super-resolution fluorescence microscopy to work. *Nat Methods* 6:21–23.
- Liu KSY, Siebert M, Mertel S, Knoche E, Wegener S, Wichmann C, Matkovic T, Muhammad K, Depner H, Mettke C, Buckers J, Hell SW, Müller M, Davis GW, Schmitz D, Sigrist SJ (2011) RIM-Binding Protein, a Central Part of the Active Zone, Is Essential for Neurotransmitter Release. *Science* 334:1565–1569.
- Ljaschenko D, Ehmann N, Kittel RJ (2013) Hebbian plasticity guides maturation of glutamate receptor fields *in vivo*. *Cell Rep* 3:1407–1413.
- Loewi O (1921) Über humorale Übertragbarkeit der Herznervenwirkung. *Pflügers Arch. ges Physiol* 189:239.
- Ma C, Su L, Seven AB, Xu Y, Rizo J (2013) Reconstitution of the vital functions of Munc18 and Munc13 in neurotransmitter release. *Science* 339:421–425.
- Macleod GT, Hegström-Wojtowicz M, Charlton MP, Atwood HL (2002) Fast calcium signals in *Drosophila* motor neuron terminals. *J Neurophysiol* 88:2659–2663.
- Maglione M, Sigrist SJ (2013) Seeing the forest tree by tree: super-resolution light microscopy meets the neurosciences. *Nat Neurosci* 16:790–797.
- Marrus SB, DiAntonio A (2004) Preferential localization of glutamate receptors opposite sites of high presynaptic release. *Curr Biol* 14:924–931.
- Marrus SB, Portman SL, Allen MJ, Moffat KG, DiAntonio A (2004) Differential localization of glutamate receptor subunits at the *Drosophila* neuromuscular junction. *J Neurosci* 24:1406–1415.

- Marvin JS, Borghuis BG, Tian L, Cichon J, Harnett MT, Akerboom J, Gordus A, Renninger SL, Chen T-W, Bargmann CI, Orger MB, Schreiter ER, Demb JB, Gan W-B, Hires SA, Looger LL (2013) An optimized fluorescent probe for visualizing glutamate neurotransmission. *Nat Methods* 10:162–170.
- Matkovic T, Siebert M, Knoche E, Depner H, Mertel S, Oswald D, Schmidt M, Thomas U, Sickmann A, Kamin D, Hell SW, Bürger J, Hollmann C, Mielke T, Wichmann C, Sigrist SJ (2013) The Bruchpilot cytomatrix determines the size of the readily releasable pool of synaptic vesicles. *J Cell Biol* 202:667–683.
- Matz J, Gilyan A, Kolar A, McCarvill T, Krueger SR (2010) Rapid structural alterations of the active zone lead to sustained changes in neurotransmitter release. *Proc Natl Acad Sci U S A* 107:8836–8841.
- Mayer ML, Westbrook GL, Guthrie PB (1984) Voltage-dependent block by Mg^{2+} of NMDA responses in spinal cord neurones. *Nature* 309:261–263.
- McMahon HT, Missler M, Li C, Südhof TC (1995) Complexins: Cytosolic proteins that regulate SNAP receptor function. *Cell* 83:111–119.
- Meinrenken CJ, Borst JGG, Sakmann B (2002) Calcium secretion coupling at calyx of held governed by nonuniform channel-vesicle topography. *J Neurosci* 22:1648–1667.
- Meyer L, Wildanger D, Medda R, Punge A, Rizzoli SO, Donnert G, Hell SW (2008) Dual-color STED microscopy at 30-nm focal-plane resolution. *Small* 4:1095–1100.
- Miesenböck G (2009) The optogenetic catechism. *Science* 326:395–399.
- Miśkiewicz K, Jose LE, Bento-Abreu A, Fislage M, Taes I, Kasprówicz J, Swerts J, Sigrist S, Versées W, Robberecht W, Verstreken P (2011) ELP3 controls active zone morphology by acetylating the ELKS family member Bruchpilot. *Neuron* 72:776–788.
- Monastirioti M, Gorczyca M, Rapus J, Eckert M, White K, Budnik V (1995) Octopamine immunoreactivity in the fruit fly *Drosophila melanogaster*. *J Comp Neurol* 356:275–287.
- Moulder KL, Mennerick S (2005) Reluctant vesicles contribute to the total readily releasable pool in glutamatergic hippocampal neurons. *J Neurosci* 25:3842–3850.
- Nagel G, Ollig D, Fuhrmann M, Kateriya S, Musti AM, Bamberg E, Hegemann P (2002) Channelrhodopsin-1: a light-gated proton channel in green algae. *Science* 296:2395–2398.
- Nagel G, Szellas T, Huhn W, Kateriya S, Adeishvili N, Berthold P, Ollig D, Hegemann P, Bamberg E (2003) Channelrhodopsin-2, a directly light-gated cation-selective membrane channel. *Proc Natl Acad Sci U S A* 100:13940–13945.
- Nägerl UV, Willig KI, Hein B, Hell SW, Bonhoeffer T (2008) Live-cell imaging of dendritic spines by STED microscopy. *Proc Natl Acad Sci U S A* 105:18982–18987.
- Nanguneri S, Flottmann B, Horstmann H, Heilemann M, Kuner T (2012) Three-dimensional, tomographic super-resolution fluorescence imaging of serially sectioned thick samples. *PLoS One* 7:e38098.
- Neher E (1998) Vesicle pools and Ca^{2+} microdomains: new tools for understanding their roles in neurotransmitter release. *Neuron* 20:389–399.
- Neher E (2010a) Complexin: Does It Deserve Its Name? *Neuron* 68:803–806.
- Neher E (2010b) What is Rate-Limiting during Sustained Synaptic Activity: Vesicle Supply or the Availability of Release Sites. *Front Synaptic Neurosci* 2:144.

- Neher E, Sakaba T (2008) Multiple Roles of Calcium Ions in the Regulation of Neurotransmitter Release. *Neuron* 59:861–872.
- Ni JQ, Liu LP, Binari R, Hardy R, Shim HS, Cavallaro A, Booker M, Pfeiffer BD, Markstein M, Wang H, Villalta C, Laverty TR, Perkins LA, Perrimon N (2009) A *Drosophila* resource of transgenic RNAi lines for neurogenetics. *Genetics* 182:1089–1100.
- Nicoll RA, Kauer JA, Malenka RC (1988) The current excitement in long term potentiation. *Neuron* 1:97–103.
- Nowak L, Bregestovski P, Ascher P, Herbet A, Prochiantz A (1984) Magnesium gates glutamate-activated channels in mouse central neurones. *Nature* 307:462–465.
- Ohana O, Sakmann B (1998) Transmitter release modulation in nerve terminals of rat neocortical pyramidal cells by intracellular calcium buffers. *J Physiol* 513 (Pt 1):135–148.
- Ohtsuka T, Takao-Rikitsu E, Inoue E, Inoue M, Takeuchi M, Matsubara K, Deguchi-Tawarada M, Satoh K, Morimoto K, Nakanishi H, Takai Y (2002) CAST: A novel protein of the cytomatrix at the active zone of synapses that forms a ternary complex with RIM1 and Munc13-1. *J Cell Biol* 158:577–590.
- Owald D, Fouquet W, Schmidt M, Wichmann C, Mertel S, Depner H, Christiansen F, Zube C, Quentin C, Körner J, Urlaub H, Mechtler K, Sigrist SJ (2010) A Syd-1 homologue regulates pre- and postsynaptic maturation in *Drosophila*. *J Cell Biol* 188:565–579.
- Patterson G, Davidson M, Manley S, Lippincott-Schwartz J (2010) Superresolution imaging using single-molecule localization. *Annu Rev Phys Chem* 61:345–367.
- Paul MM, Pauli M, Ehmann N, Hallermann S, Sauer M, Kittel RJ, Heckmann M (2015) Bruchpilot and Synaptotagmin collaborate to drive rapid glutamate release and active zone differentiation. *Front Cell Neurosci* 9:1–12.
- Peled ES, Isacoff EY (2011) Optical quantal analysis of synaptic transmission in wild-type and rab3-mutant *Drosophila* motor axons. *Nat Neurosci* 14:519–526.
- Peng I-F, Wu C-F (2007) *Drosophila* cacophony channels: a major mediator of neuronal Ca²⁺ currents and a trigger for K⁺ channel homeostatic regulation. *J Neurosci* 27:1072–1081.
- Pfenninger K, Akert K, Moor H, Sandri C (1972) The fine structure of freeze-fractured presynaptic membranes. *J Neurocytol* 1:129–149.
- Phillips GR, Huang JK, Wang Y, Tanaka H, Shapiro L, Zhang W, Shan WS, Arndt K, Frank M, Gordon RE, Gawinowicz MA, Zhao Y, Colman DR (2001) The presynaptic particle web: ultrastructure, composition, dissolution, and reconstitution. *Neuron* 32:63–77.
- Potter CJ, Tasic B, Russler E V, Liang L, Luo L (2010) The Q system: a repressible binary system for transgene expression, lineage tracing, and mosaic analysis. *Cell* 141:536–548.
- Prokop A (1999) Integrating bits and pieces: Synapse structure and formation in *Drosophila* embryos. *Cell Tissue Res* 297:169–186.
- Puchner EM, Walter JM, Kasper R, Huang B, Lim W a (2013) Counting molecules in single organelles with superresolution microscopy allows tracking of the endosome maturation trajectory. *Proc Natl Acad Sci U S A* 110:16015–16020.
- Qin G, Schwarz T, Kittel RJ, Schmid A, Rasse TM, Kappei D, Ponimaskin E, Heckmann M, Sigrist SJ (2005) Four different subunits are essential for expressing

- the synaptic glutamate receptor at neuromuscular junctions of *Drosophila*. *J Neurosci* 25:3209–3218.
- Ramón y Cajal S (1894) The Croonian Lecture: La fine structure des centres nerveux. *Proc R Soc London*.
- Rasse TM, Fouquet W, Schmid A, Kittel RJ, Mertel S, Sigrist CB, Schmidt M, Guzman A, Merino C, Qin G, Quentin C, Madeo FF, Heckmann M, Sigrist SJ (2005) Glutamate receptor dynamics organizing synapse formation *in vivo*. *Nat Neurosci* 8:898–905.
- Richmond JE, Weimer RM, Jorgensen EM (2001) An open form of syntaxin bypasses the requirement for UNC-13 in vesicle priming. *Nature* 412:338–341.
- Rieckhof GE, Yoshihara M, Guan Z, Littleton JT (2003) Presynaptic N-type calcium channels regulate synaptic growth. *J Biol Chem* 278:41099–41108.
- Ries J, Kaplan C, Platonova E, Eghlidi H, Ewers H (2012) A simple, versatile method for GFP-based super-resolution microscopy via nanobodies. *Nat Methods* 9:582–584.
- Rong YS, Titen SW, Xie HB, Golic MM, Bastiani M, Bandyopadhyay P, Olivera BM, Brodsky M, Rubin GM, Golic KG (2002) Targeted mutagenesis by homologous recombination in *D. melanogaster*. *Genes Dev* 16:1568–1581.
- Rosenmund C (2003) Molecular mechanisms of active zone function. *Curr Opin Neurobiol* 13:509–519.
- Rosenmund C, Stevens CF (1996) Definition of the Readily Releasable Pool of Vesicles at Hippocampal Synapses. *Neuron* 16:1197–1207.
- Rozov A, Burnashev N, Sakmann B, Neher E (2001) Transmitter release modulation by intracellular Ca^{2+} buffers in facilitating and depressing nerve terminals of pyramidal cells in layer 2/3 of the rat neocortex indicates a target cell-specific difference in presynaptic calcium dynamics. *J Physiol* 531:807–826.
- Rust MJ, Bates M, Zhuang X (2006) Sub-diffraction-limit imaging by stochastic optical reconstruction microscopy (STORM). *Nat Methods* 3:793–795.
- Sabatini BL, Regehr WG (1996) Timing of neurotransmission at fast synapses in the mammalian brain. *Nature* 384:170–172.
- Saitoe M, Tanaka S, Takata K, Kidokoro Y (1997) Neural activity affects distribution of glutamate receptors during neuromuscular junction formation in *Drosophila* embryos. *Dev Biol* 184:48–60.
- Sakaba T (2006) Roles of the fast-releasing and the slowly releasing vesicles in synaptic transmission at the calyx of held. *J Neurosci* 26:5863–5871.
- Sakaba T, Schneggenburger R, Neher E (2002) Estimation of quantal parameters at the calyx of Held synapse. *Neurosci Res* 44:343–356.
- Sätzler K, Söhl LF, Bollmann JH, Borst JGG, Frotscher M, Sakmann B, Lübke JHR (2002) Three-dimensional reconstruction of a calyx of Held and its postsynaptic principal neuron in the medial nucleus of the trapezoid body. *J Neurosci* 22:10567–10579.
- Sauer M (2013) Localization microscopy coming of age: from concepts to biological impact. *J Cell Sci* 126:3505–3513.
- Schäfer P, van de Linde S, Lehmann J, Sauer M, Doose S (2013) Methylene blue- and thiol-based oxygen depletion for super-resolution imaging. *Anal Chem* 85:3393–3400.
- Schermelleh L, Heintzmann R, Leonhardt H (2010) A guide to super-resolution fluorescence microscopy. *J Cell Biol* 190:165–175.

- Scheuss V, Schneggenburger R, Neher E (2002) Separation of presynaptic and postsynaptic contributions to depression by covariance analysis of successive EPSCs at the calyx of held synapse. *J Neurosci* 22:728–739.
- Schmid A, Hallermann S, Kittel RJ, Khorramshahi O, Frölich AMJ, Quentin C, Rasse TM, Mertel S, Heckmann M, Sigrist SJ (2008) Activity-dependent site-specific changes of glutamate receptor composition *in vivo*. *Nat Neurosci* 11:659–666.
- Schmid A, Qin G, Wichmann C, Kittel RJ, Mertel S, Fouquet W, Schmidt M, Heckmann M, Sigrist SJ (2006) Non-NMDA-type glutamate receptors are essential for maturation but not for initial assembly of synapses at *Drosophila* neuromuscular junctions. *J Neurosci* 26:11267–11277.
- Schmid A, Sigrist SJ (2008) Analysis of neuromuscular junctions: histology and *in vivo* imaging. *Methods Mol Biol* 420:239–251.
- Schneggenburger R, Neher E (2005) Presynaptic calcium and control of vesicle fusion. *Curr Opin Neurobiol* 15:266–274.
- Schneggenburger R, Sakaba T, Neher E (2002) Vesicle pools and short-term synaptic depression: lessons from a large synapse. *Trends Neurosci* 25:206–212.
- Schuster CM, Davis GW, Fetter RD, Goodman CS (1996) Genetic dissection of structural and functional components of synaptic plasticity. II. Fasciclin II controls presynaptic structural plasticity. *Neuron* 17:655–667.
- Sharonov A, Hochstrasser RM (2007) Single-molecule imaging of the association of the cell-penetrating peptide Pep-1 to model membranes. *Biochemistry* 46:7963–7972.
- Sheng J, He L, Zheng H, Xue L, Luo F, Shin W, Sun T, Kuner T, Yue DT, Wu L-G (2012) Calcium-channel number critically influences synaptic strength and plasticity at the active zone. *Nat Neurosci* 15:998–1006.
- Sieber JJ, Willig KI, Heintzmann R, Hell SW, Lang T (2006) The SNARE motif is essential for the formation of syntaxin clusters in the plasma membrane. *Biophys J* 90:2843–2851.
- Sieber JJ, Willig KI, Kutzner C, Gerding-Reimers C, Harke B, Donnert G, Rammner B, Eggeling C, Hell SW, Grubmüller H, Lang T (2007) Anatomy and dynamics of a supramolecular membrane protein cluster. *Science* 317:1072–1076.
- Sigrist SJ, Sabatini BL (2012) Optical super-resolution microscopy in neurobiology. *Curr Opin Neurobiol* 22:86–93.
- Siksou L, Rostaing P, Lechaise J-P, Boudier T, Ohtsuka T, Fejtová A, Kao H-T, Greengard P, Gundelfinger ED, Triller A, Marty S (2007) Three-dimensional architecture of presynaptic terminal cytomatrix. *J Neurosci* 27:6868–6877.
- Silver RA, Lubke J, Sakmann B, Feldmeyer D (2003) High-probability unquantal transmission at excitatory synapses in barrel cortex. *Science* 302:1981–1984.
- Smith LA, Wang X, Peixoto AA, Neumann EK, Hall LM, Hall JC (1996) A *Drosophila* Calcium Channel $\alpha 1$ Subunit Gene Maps to a Genetic Locus Associated with Behavioral and Visual Defects. *J Neurosci* 16:7868–7879.
- Sochacki KA, Larson BT, Sengupta DC, Daniels MP, Shtengel G, Hess HF, Taraska JW (2012) Imaging the post-fusion release and capture of a vesicle membrane protein. *Nat Commun* 3:1154.
- Sorra KE, Mishra a., Kirov S a., Harris KM (2006) Dense core vesicles resemble active-zone transport vesicles and are diminished following synaptogenesis in mature hippocampal slices. *Neuroscience* 141:2097–2106.

- Specht CG, Izeddin I, Rodriguez PC, El Beheiry M, Rostaing P, Darzacq X, Dahan M, Triller A (2013) Quantitative nanoscopy of inhibitory synapses: counting gephyrin molecules and receptor binding sites. *Neuron* 79:308–321.
- Stanley EF (1993) Single calcium channels and acetylcholine release at a presynaptic nerve terminal. *Neuron* 11:1007–1011.
- Stanley EF (1997) The calcium channel and the organization of the presynaptic transmitter release face. *Trends Neurosci* 20:404–409.
- Stewart BA, Atwood HL, Renger JJ, Wang J, Wu C-F (1994) Improved stability of *Drosophila* larval neuromuscular preparations in haemolymph-like physiological solutions. *J Comp Physiol A* 175:179–191.
- Südhof TC (2004) The synaptic vesicle cycle. *Annu Rev Neurosci* 27:509–547.
- Südhof TC (2012) The presynaptic active zone. *Neuron* 75:11–25.
- Südhof TC (2013) Neurotransmitter release: the last millisecond in the life of a synaptic vesicle. *Neuron* 80:675–690.
- Sugiyama Y, Kawabata I, Sobue K, Okabe S (2005) Determination of absolute protein numbers in single synapses by a GFP-based calibration technique. *Nat Methods* 2:677–684.
- Sullivan WA, Ashburner M, Hawley RS (2000) *Drosophila* protocols. (Sullivan WA, Ashburner M, Hawley RS, eds). Cold Spring Harbor Laboratory Press.
- Sun J, Pang ZP, Qin D, Fahim AT, Adachi R, Südhof TC (2007) A dual-Ca²⁺-sensor model for neurotransmitter release in a central synapse. *Nature* 450:676–682.
- Szule J a., Harlow ML, Jung JH, De-Miguel FF, Marshall RM, McMahan UJ (2012) Regulation of synaptic vesicle docking by different classes of macromolecules in active zone material. *PLoS One* 7.
- Tarr TB, Dittrich M, Meriney SD (2013) Are unreliable release mechanisms conserved from NMJ to CNS? *Trends Neurosci* 36:14–22.
- The Axon Guide (2012) The Axon guide for electrophysiology & biophysics laboratory techniques, 3rd edition.
- The FlyBase Consortium (2003) The FlyBase database of the *Drosophila* genome projects and community literature. *Nucleic Acids Res* 31:172–175.
- Tokunaga M, Imamoto N, Sakata-Sogawa K (2008) Highly inclined thin illumination enables clear single-molecule imaging in cells. *Nat Methods* 5:159–161.
- tom Dieck S, Sanmartí-Vila L, Langnaese K, Richter K, Kindler S, Soyke A, Wex H, Smalla KH, Kämpf U, Fränzer JT, Stumm M, Garner CC, Gundelfinger ED (1998) Bassoon, a novel zinc-finger CAG/glutamine-repeat protein selectively localized at the active zone of presynaptic nerve terminals. *J Cell Biol* 142:499–509.
- Tong G, Jahr CE (1994) Multivesicular release from excitatory synapses of cultered hippocampal neurons. *Neuron* 12:51–59.
- Tønnesen J, Katona G, Rózsa B, Nägerl UV (2014) Spine neck plasticity regulates compartmentalization of synapses. *Nat Neurosci* 17:678–685.
- Tønnesen J, Nägerl UV (2013) Superresolution imaging for neuroscience. *Exp Neurol* 242:33–40.
- Trommershäuser J, Schneggenburger R, Zippelius A, Neher E (2003) Heterogeneous presynaptic release probabilities: functional relevance for short-term plasticity. *Biophys J* 84:1563–1579.
- Ulbrich MH, Isacoff EY (2007) Subunit counting in membrane-bound proteins. *Nat Methods* 4:319–321.

- van de Linde S, Löschberger A, Klein T, Heidbreder M, Wolter S, Heilemann M, Sauer M (2011) Direct stochastic optical reconstruction microscopy with standard fluorescent probes. *Nat Protoc* 6:991–1009.
- Venken KJT, Bellen HJ (2005) Emerging technologies for gene manipulation in *Drosophila melanogaster*. *Nat Rev Genet* 6:167–178.
- von Schilcher F (1976) The behavior of cacophony, a courtship song mutant in *Drosophila melanogaster*. *Behav Biol* 17:187–196.
- von Schilcher F (1977) A mutation which changes courtship song in *Drosophila melanogaster*. *Behav Genet* 7:251–259.
- Vyleta NP, Jonas P (2014) Loose coupling between Ca²⁺ channels and release sensors at a plastic hippocampal synapse. *Science* 343:665–670.
- Wadel K, Neher E, Sakaba T (2007) The coupling between synaptic vesicles and Ca²⁺ channels determines fast neurotransmitter release. *Neuron* 53:563–575.
- Wagh DA, Rasse TM, Asan E, Hofbauer A, Schwenkert I, Dürbeck H, Buchner S, Dabauvalle M-C, Schmidt M, Qin G, Wichmann C, Kittel R, Sigrist SJ, Buchner E (2006) Bruchpilot, a protein with homology to ELKS/CAST, is required for structural integrity and function of synaptic active zones in *Drosophila*. *Neuron* 49:833–844.
- Wang Y, Liu X, Biederer T, Südhof TC (2002) A family of RIM-binding proteins regulated by alternative splicing: implications for the genesis of synaptic active zones. *Proc Natl Acad Sci U S A* 99:14464.
- Watanabe S, Punge A, Hollopeter G, Willig KI, Hobson RJ, Davis MW, Hell SW, Jorgensen EM (2011) Protein localization in electron micrographs using fluorescence nanoscopy. *Nat Methods* 8:80–84.
- Weber K, Rathke PC, Osborn M (1978) Cytoplasmic microtubular images in glutaraldehyde-fixed tissue culture cells by electron microscopy and by immunofluorescence microscopy. *Proc Natl Acad Sci U S A* 75:1820–1824.
- Westphal V, Rizzoli SO, Lauterbach MA, Kamin D, Jahn R, Hell SW (2008) Video-rate far-field optical nanoscopy dissects synaptic vesicle movement. *Science* 320:246–249.
- Weyhersmüller A, Hallermann S, Wagner N, Eilers J (2011) Rapid active zone remodeling during synaptic plasticity. *J Neurosci* 31:6041–6052.
- Wichmann C, Sigrist SJ (2010) The active zone T-bar – a plasticity module? *J Neurogenet* 24:133–145..
- Wilhelm BG, Mandad S, Truckenbrodt S, Kröhnert K, Schäfer C, Rammner B, Koo SJ, Claßen GA, Krauss M, Haucke V, Urlaub H, Rizzoli SO (2014) Composition of isolated synaptic boutons reveals the amounts of vesicle trafficking proteins. *Science* 344:1023–1028.
- Willig KI, Rizzoli SO, Westphal V, Jahn R, Hell SW (2006) STED microscopy reveals that synaptotagmin remains clustered after synaptic vesicle exocytosis. *Nature* 440:935–939.
- Winterflood CM, Ewers H (2014) Single-Molecule Localization Microscopy using mCherry. *Chemphyschem*:3–8.
- Wojcik SM, Brose N (2007) Regulation of membrane fusion in synaptic excitation-secretion coupling: speed and accuracy matter. *Neuron* 55:11–24.
- Wojtowicz JM, Marin L, Atwood HL (1994) Activity-induced changes in synaptic release sites at the crayfish neuromuscular junction. *J Neurosci* 14:3688–3703.

- Wölfel M, Lou X, Schneggenburger R (2007) A mechanism intrinsic to the vesicle fusion machinery determines fast and slow transmitter release at a large CNS synapse. *J Neurosci* 27:3198–3210.
- Wolpert L, Tickle C (2011) *Principles of Development*. Oxford University Press.
- Wolter S, Endesfelder U, van de Linde S, Heilemann M, Sauer M (2011) Measuring localization performance of super-resolution algorithms on very active samples. *Opt Express* 19:7020–7033.
- Wolter S, Löschberger A, Holm T (2012) *rapidSTORM*: accurate, fast open-source software for localization microscopy. *Nat Methods* 9:1040–1041.
- Wolter S, Schüttpelz M, Tscherepanow M, van de Linde S, Heilemann M, Sauer M (2010) Real-time computation of subdiffraction-resolution fluorescence images. *J Microsc* 237:12–22.
- Wu Y, Kawasaki F, Ordway RW (2005) Properties of short-term synaptic depression at larval neuromuscular synapses in wild-type and temperature-sensitive paralytic mutants of *Drosophila*. *J Neurophysiol* 93:2396–2405.
- Xu-Friedman MA, Harris KM, Regehr WG (2001) Three-dimensional comparison of ultrastructural characteristics at depressing and facilitating synapses onto cerebellar Purkinje cells. *J Neurosci* 21:6666–6672.
- Zhai RG, Bellen HJ (2004) The architecture of the active zone in the presynaptic nerve terminal. *Physiology (Bethesda)* 19:262–270.
- Zhai RG, Vardinon-Friedman H, Cases-Langhoff C, Becker B, Gundelfinger ED, Ziv NE, Garner CC (2001) Assembling the presynaptic active zone: A characterization of an active zone precursor vesicle. *Neuron* 29:131–143.
- Zhang Q, Cao Y-Q, Tsien RW (2007) Quantum dots provide an optical signal specific to full collapse fusion of synaptic vesicles. *Proc Natl Acad Sci U S A* 104:17843–17848.
- Zhang Q, Li Y, Tsien R (2009) The dynamic control of kiss-and-run and vesicular reuse probed with single nanoparticles. *Science* 323:1448–1453.
- Zhong Y, Peña LA (1995) A novel synaptic transmission mediated by a PACAP-like neuropeptide in *Drosophila*. *Neuron* 14:527–536.
- Zucker RS, Regehr WG (2002) Short-term synaptic plasticity. *Annu Rev Physiol* 64:355–405.

8. Abbreviations

2D = two dimensional

3D = three dimensional

A488 = Alexa Fluor 488

A532 = Alexa Fluor 532

A700 = Alexa Fluor 700

AZ = active zone

BAPTA = 1,2-bis(o-aminophenoxy)ethane-N,N,N',N'-tetraacetic acid)

Brp = Bruchpilot

Ca²⁺ = calcium

CaCl₂ = calcium chloride

CAST = CAZ-associated structural protein

CAZ = cytomatrix associated with the AZ

DBSCAN = density based spatial clustering of applications with noise

ChR1 = Channelrhodopsin 1

ChR2 = Channelrhodopsin-2

cm = centimeter

DLiprin- α = *Drosophila* Liprin- α

DMSO = dimethyl sulfoxide

dSTORM = *direct* stochastic optical reconstruction microscopy

Dsyd-1 = *Drosophila* Syd-1, synapse defective-1

e.g. = for example, *exempli gratia*

eEPSC = evoked excitatory current

EGTA = ethylene glycol tetraacetic acid

EM = electron microscopy

Eps = epsilon; distance between neighbours
FWHM= full width at half maximum
GDP = guanosine diphosphate
GFP = green fluorescent protein
GluR = glutamate receptor
GTP = guanosine triphosphate
H₂O = water
HCl = hydrogen chloride
HEPES = 4-(2-hydroxyethyl)-1-piperazineethanesulfonic acid
HL-3 = haemolymph like solution
HPF = high-pressure freezing
HRP = horseradish peroxidase
i.e. = that is, id est
Ib = type I big boutons
Is = type I small boutons
KCl = potassium chloride
kDa = kilo Dalton
kW = kilowatt
LTD = long-term depression
LTP = long-term potentiation
MEA = mercaptoethylamine
MgCl₂ = magnesium chloride
minis = miniature EPSCs
mm = millimeter
mM = millimolar; M = molar
mV = milli Volt

$M\Omega$ = mega Ohm

N = number of release sites or number of RRV

NA = numerical aperture

Na_2HPO_4 = di-sodium hydrogen phosphate

NaCl = sodium chloride

NaH_2PO_4 = sodium di-hydrogen phosphate

$NaHCO_3$ = sodium bicarbonate

NaOH = sodium hydroxide

NGS = normal goat serum

nm = nanometer (10^{-9} meter)

NMDAR = N-methyl-D-aspartate receptor

NMJ = neuromuscular junction

NSOM = near-field scanning optical microscopy

P = permeability coefficient

PALM = photo-activated localization microscopy

PBS = phosphate buffered saline

pF = pico Farad

PFA = paraformaldehyde

PSF = point-spread function

p_{vr} = release probability

px = pixel

RBP = RIM binding protein

RIM = Rab3 interacting molecule

RNAi = ribonucleic acid interference

RRP = readily releasable pool

RRV = readily releasable vesicles

rup = running-unapposed

s.d. = standard deviation

SIM = structured illumination microscopy

SM = Sec1/Munc18-like

SNARE = soluble N-ethylmaleimide-sensitive factor attachment receptor

SRM = super-resolution microscopy

SSIM = saturated-SIM

STED = stimulated emission depletion

STP = short-term synaptic plasticity

SV = synaptic vesicle

TEVC = two electrode voltage clamp

TIRF = total internal reflection microscopy

U/ml = units per milliliter

V_{cmd} = command potential

VLM = ventral longitudinal muscles

V_m = resting membrane potential

VNC = ventral nerve cord

w/v = measure of concentration: weight of solid per total volume of solution (%)

wt = wildtype

XXL = eXtra high eXpression and Long open state

μm = micrometer (10^{-6} meter)

μW = microwatt

9. Table of figures

Figure 1 AZ ultrastructures. _____	6
Figure 2 Schematics of nanodomain and microdomain coupling at a single vesicle release site. _____	7
Figure 3 Key players at the presynaptic AZ. _____	9
Figure 4 <i>Drosophila melanogaster</i> . _____	15
Figure 5 <i>Drosophila</i> neuromuscular system. _____	16
Figure 6 Synaptic structure of the <i>Drosophila</i> NMJ. _____	18
Figure 7 Ultrastructural composition of the <i>Drosophila</i> AZ. _____	21
Figure 8 Super-resolution microscopy. _____	30
Figure 9 Two-electrode voltage clamp and its application at the <i>Drosophila</i> NMJ. _____	33
Figure 10 <i>d</i> STORM resolves substructural information on the CAZ. _____	46
Figure 11 <i>d</i> STORM of wt CAZs with three different photoswitchable fluorophores. _____	47
Figure 12 Density-based analysis reveals that CAZ-units are built from multiple Brp clusters. _____	48
Figure 13 Counting Brp molecules within the CAZ. _____	50
Figure 14 Confocal imaging of <i>rab3^{rup}</i> and <i>brp^{nude}</i> . _____	53
Figure 15 Different nano-organization of Brp within the CAZ. _____	55
Figure 16 Similar spontaneous transmitter release at larval NMJs. _____	57
Figure 17 Only subtle differences in evoked release. _____	57
Figure 18 Functional characterization of different AZ states. _____	58
Figure 19 Quantitative description of synaptic depression. _____	59
Figure 20 Structure-function relationships at the <i>Drosophila</i> AZ. _____	61
Figure 21 Structural gradient along <i>Drosophila</i> Ib motor neurons. _____	62
Figure 22 CAZ ultrastructure of type Is boutons. _____	63
Figure 23 Organization of fluorophores around Brp filaments. _____	67
Figure 24 Titration of A532-labelled secondary antibodies.. _____	69
Figure 25 Microscopy of <i>Drosophila</i> AZs. _____	75
Figure 26 ChR2 expression in individual synaptic compartments. _____	77
Figure 27 ChR2 localization patterns. _____	78
Equation 1 DOL determination. _____	38
Equation 2 Estimation of Brp molecules per CAZ-unit. _____	44
Table 1 Localization values from antibody titrations. _____	52
Table 2 Structure of AZs. _____	56
Table 3 Modelling parameters. _____	60

10. Appendix

10.1 List of publications

Paul MM, Pauli M, Ehmann N, Hallermann S, Sauer M, Kittel RJ and Heckmann M (2015). Bruchpilot and Synaptotagmin collaborate to drive rapid glutamate release and active zone differentiation. *Front. Cell. Neurosci.* 9:29.

Ehmann N, Sauer M, Kittel RJ (2015) Super-resolution microscopy of the synaptic active zone. *Front. Cell. Neurosci.* 9:7.

Dawydow A*, Gueta R*, Ljaschenko D, Ullrich S, Hermann M, Ehmann N, Gao S, Fiala A, Langenhan T, Nagel G, Kittel RJ (2014) Channelrhodopsin-2-XXL, a powerful optogenetic tool for low-light applications. *Proc Natl Acad Sci* 111:13972–13977. (*equal contribution)

Ehmann N*, van de Linde S*, Alon A, Ljaschenko D, Keung XZ, Holm T, Rings A, DiAntonio A, Hallermann S, Ashery U, Heckmann M, Sauer M, Kittel RJ (2014) Quantitative super-resolution imaging of Bruchpilot distinguishes active zone states. *Nat Commun* 5:1–12. (*equal contribution)

Ljaschenko D, Ehmann N, Kittel RJ (2013) Hebbian plasticity guides maturation of glutamate receptor fields *in vivo*. *Cell Rep* 3:1407–1413.

10.2 Curriculum vitae

Nadine
Ehmann

University of Würzburg
Institute of Physiology
Dept of Neurophysiology
Röntgenring 9
97070 Würzburg

nadine.ehmann@uni-wuerzburg.de
phone 0931-31-83923

personal details

Gender: female
Date of birth: 26.12.1984
Place of birth: 74722 Buchen

education

2010-present

PhD (Doctor rerum naturalium) student
University of Würzburg, Institute of Physiology/Neurophysiology
'Linking the active zone ultrastructure to function in *Drosophila*'

2009-2010

Diploma thesis, University of Würzburg, Institute of Physiology, Dept of
Neurophysiology
'Molecular changes during synaptic plasticity'

2004-2009

Studies in biology
2009 Diplom
Main focus: Neurobiology; focus: biotechnology, biochemistry

2004

University entrance qualification (Abitur); Burghardt-Gymnasium Buchen

publications

Paul MM, Pauli M, Ehmann N, Hallermann S, Sauer M, Kittel RJ and Heckmann M
(2015). Bruchpilot and Synaptotagmin collaborate to drive rapid glutamate release
and active zone differentiation. *Front. Cell. Neurosci.* 9:29.

Ehmann N, Sauer M, Kittel RJ (2015) Super-resolution microscopy of the synaptic
active zone. *Front. Cell. Neurosci.* 9:7.

Dawydow A*, Gueta R*, Ljaschenko D, Ullrich S, Hermann M, Ehmann N, Gao S,
Fiala A, Langenhan T, Nagel G, Kittel RJ (2014) Channelrhodopsin-2-XXL, a
powerful optogenetic tool for low-light applications. *Proc Natl Acad Sci*
111:13972–13977. (*equal contribution)

Ehmann N*, van de Linde S*, Alon A, Ljaschenko D, Keung XZ, Holm T, Rings A,
DiAntonio A, Hallermann S, Ashery U, Heckmann M, Sauer M, Kittel RJ (2014)
Quantitative super-resolution imaging of Bruchpilot distinguishes active zone
states. *Nat Commun* 5:1–12. (*equal contribution)

Ljaschenko D, Ehmann N, Kittel RJ (2013) Hebbian plasticity guides maturation of
glutamate receptor fields *in vivo*. *Cell Rep* 3:1407–1413.

skills and experiences

Summer and winter semester 2014

Practical course and seminar supervision in general human physiology, University
of Würzburg

November 2013

Oral presentation at the 43rd annual meeting of the Society for Neuroscience
2013.

'Functional super-resolution imaging of active zone states'

October 2011/2012

Member of the organizing committee of the 6th and 7th international symposium
of the Graduate School of Life Sciences, University Würzburg

honors and awards

2010-2014

PhD fellowship from the Graduate School of Life Sciences, University of Würzburg

2012

Poster award at the 91st annual meeting of the German Physiological Society.
'Genetic expression of an active zone peptide as a tool to induce sell-specific
synaptic depression *in vivo*.'

